A Dissertation

entitled

Performance-Based Engineering for Resilient and Sustainable Structures of the Future

by

Rafael de Amorim Salgado

Submitted to the Graduate Faculty as partial fulfillment of the requirements for the

Doctor of Philosophy Degree in

Civil Engineering

Dr. Serhan Guner, Committee Chair

Dr. Liangbo Hu, Committee Member

Dr. Luis Alexander Mata, Committee Member

Dr. Mark A. Pickett, Committee Member

Dr. Shiling Pei, Committee Member

Dr. Amanda C. Bryant-Friedrich, Dean
College of Graduate Studies

The University of Toledo

August 2020

An Abstract of

Performance-Based Engineering for Resilient and Sustainable Structures of the Future

by

Rafael de Amorim Salgado

Submitted to the Graduate Faculty as partial fulfillment of the requirements for the
Doctor of Philosophy Degree in
Civil Engineering

The University of Toledo
August 2020

Using prescriptive design approaches, structures are intended to provide a life-safety level of protection that has been shown by recent natural hazard events to have limited contribution to the post-disaster resilience of a community. The performance-based engineering (PBE) methodology allows the structure to be designed to achieve any pre-defined performance objective. The structures of the future will not only aim at being structurally resilient but also sustainable to natural hazard loads. To contribute to the development of these structures, PBE requires the development of state-of-the-art numerical models for the accurate structural performance assessment and the creation of a framework that can effectively account for this performance when evaluating the environmental impacts of structures.

This research has two main goals: i) to create state-of-the-art high-fidelity numerical models for the PBE of structures; and ii) to create a multidisciplinary framework for the resilient-based environmental impact assessment of structures subjected to natural hazard loads. In pursuit of this research's goals, four main objectives were conducted: High-Fidelity Numerical Modeling, PBE, Life Cycle Assessment, and Combined PBE and LCA. This research has been primarily conducted on reinforced concrete (RC) and cross

laminated timber (CLT) structures, as the first is a traditional and resilient while the second is a newer and seemingly more sustainable structural alternative. However, the created approach can also be applied to other structural alternatives under natural hazard loads. The high-fidelity numerical models created have demonstrated to satisfactorily capture the structural performance of the considered building structure alternatives and the multidisciplinary framework created provides a powerful means for making science-based decisions when considering newer and seemingly more sustainable building structure alternatives while accounting for their natural hazard resilience level.

To my God, who has helped me all the way up to here.

Acknowledgments

First of all, I would like to thank God for giving me the strength to conclude this step of my life. Without His grace over me every day of this journey, I would not have reached this far. "*For from him and through him and for him are all things. To him be the glory forever! Amen*." (Romans 11:36).

I thank my wife, Mônica Salgado, which has been with me on this journey even before we constituted a family. Your endless support, care, and love is an essential part of this achievement. I would also like to thank my family, in special my parents, Walter Salgado and Sandra Salgado, for doing everything they could to allow me to be where I am today.

I thank my advisor Dr. Serhan Guner, who has tremendously helped me with his wisdom since even before this challenging journey began. I thank you for all the countless meeting hours, patience, and professional and personal advice given over the last five years.

Last but not least, I would like to thank all of the faculty at The University of Toledo who has helped me along this ride, whom I will be always grateful and shall not forget. In special, I would like to thank Dr. Ashok Kumar, Dr. Azadeh Parvin, Dr. Douglas Nims, and Dr. Defne Apul for all the support provided, which are greatly appreciated. May your names be registered here so I never forget you.

Table of Contents

List of Tables

List of Figures

List of Abbreviations

AASHTO ....American Association of State Highway and Transportation Officials
AC ....Acidification
ACI.............................American Concrete Institute
ANOVA ....Analysis of Variance
ASCE ....American Society of Civil Engineers

C&D...........................Construction and Demolition
CA ....Catenary Action
CAA ....Compressive Arch Action
CFRP..........................Carbon Fiber Reinforced Polymer
CLT ....Cross Laminated Timber
COV ....Coefficient of Variation
CP...............................Collapse Prevention
CSA............................Canadian Standards Association

DL ....Dead Load

EC ....Ecotoxicity
ECOV.........................Estimated Coefficient of Variation
ECPH ....Elastic with Concentrated Plasticity Hinges
EDP ....Engineering Demand Parameters
ET...............................Eutrophication

FEMA ....Federal Emergency Management Agency
FRP ....Fiber Reinforced Polymer

GFRP..........................Glass Fiber Reinforced Polymer
GM ....Ground Motion
GW-IB........................Global Warming Including Biogenic Carbon
GW-EB ....Global Warming Excluding Biogenic Carbon
GWP...........................Global Warming Potential

HHPA.........................Human Health Particulate Air
HT-C ....Human Toxicity Cancer
HT-NC ....Human Toxicity Non-Cancer

IO ....Immediate Occupancy
ISD ....Inter-Story Drift
ISO ....International Organization for Standardization

LCA...........................Life Cycle Assessment
LCI ....Life Cycle Inventory
LL..............................Live Load
LS ....Life Safety

MCFT.........................Modified Compression Field Theory

NEHRP ....National Earthquake Hazards Reduction Program
NLA ....Nonlinear Structural Analysis
NLDA ....Nonlinear Dynamic Analysis
NLFB ....Nonlinear Fiber-Based
NLFBSH ....Nonlinear Fiber-Based Shear-Hinge
NLFEA.......................Nonlinear Finite Element Analysis

ODA ....Ozone Depletion Air
OPE ....Out-of-Plane Exterior
OPI ....Out-of-Plane Interior

PBE ....Performance-Based Engineering
PBEE..........................Performance-Based Earthquake Engineering
PEER..........................Pacific Earthquake Engineering Research
PH ....Plastic Hinge
PNF ....Performance Normalization Factor

RC ....Reinforced Concrete
RCA ....Recycled Concrete Aggregate
R-FF ....Resources and Fossil Fuels

SA ....Smog Air
STM ....Strut-and-Tie Model

UBC ....Uniform Building Code

List of Symbols

$\$$ .... Currency

B .... Breadth of the building plane normal to the direction of the flow
b_f .... Flange width
bn .... Billion
b .... Width of building
C .... Constant factor
C_{cx} .... Coefficient that accounts for the openings in the building
C_d .... Drag coefficient
C_f .... Factor based on the number of nails in the floor side of the connection
CO_2 .... Carbon dioxide
C_w .... Factor based on the number of nails in the wall side of the connection
cm .... Centimeter
D .... Allowable threshold
d .... Effective depth, diameter, or distance
d_{wid} .... Withdrawal influence distance
d_i .... Position of nail i measured from the bend line of the angle bracket
E .... Elasticity
E_s .... Steel elasticity
Edp_{b1i} .... EDP for building 1 at limit state i
erf .... Gauss error function
F .... Force
F_{ax} .... Axial withdrawal capacity
F_{b2i} .... Force for building 2 at limit state i
F_{pl} .... Plastic force
F_r .... Froude number
F_u .... Ultimate force capacity
F_y .... Yield force
f_{c3} .... Confining pressure
f_c .... Concrete stress

f_{cm} ....Mean concrete stress
f_m or f_u.........................Maximum stress
f_r ....Modulus of rupture of the concrete
f_s ....Steel stress
f_{sz} ....Stress in the out-of-plane reinforcement
f_y ....Yield stress
f_{ym} ....Mean yield stress
ft ....Foot
f_{tk} ....Characteristic tensile strength of the FRP
f_{tm}................................Mean tensile strength of the FRP
G_f................................Fracture energy
GPA............................Giga Pascal
g..................................Gravity
H_c ....Connection height
h..................................Inundation depth
hp................................horsepower
I ....Inertia
in. ....Inch
K_{ax} ....Axial withdrawal stiffness
K_b ....Bending stiffness
k_{el}...............................Elastic stiffness
kg................................Kilogram
k_h ....Hardening stiffness
kip ....Kilopound
km ....Kilometer
kN...............................Kilonewton
k_s ....Softening stiffness
kWh............................Kilowatt-hour
L ....Length
L_c ....Connection length
L_w ....Web length
lb ....Pound
l_{ef} ....Thread length
M ....Moment
MPa ....Mega Pascal
m ....Meter
me...............................Milistrain
mm ....Millimeter
n..................................Number of nails
n_f or N_f........................Floor side nails
n_w or N_w......................Wall side nails

P ....Probability of…
P_{cal} ....Calculated force
P_{exp} ....Experimentally recorded force
psi..............................Pound-force per square inch
R_d...............................Design resistance
S_a ....Spectral acceleration
s or sec.......................Second
s_{Fy} ....Slip at the maximum bond stress
s_{Fu} ....Slip at the ultimate bond stress
t_f.................................Flange thickness
t_w ....Web thickness
u.................................Flow velocity
V................................Shear
V_R ....Coefficient of variation of the resistance
w_s or W_s......................Wood species
W...............................Watt

α ....Impulsive load amplification factor
α_R...............................Sensitivity factor for the resistance reliability
β ....Standard deviation or reliability index
γ_G...............................Global capacity factor
γ_s and γ_s ....Partial factors for materials for the ultimate limit states
Δ ....Displacement
ε_c...............................Concrete or compressive strain
ε_s...............................Steel strain
ε_t ....Tensile strain
θ_{max} ....Maximum first-story drift
λ.................................Leading coefficients
ρ.................................Longitudinal bottom reinforcement ratio or fluid density
ρ' ....Longitudinal top reinforcement ratio
ρ_f...............................Flange longitudinal reinforcement ratio
ρ_s ....Fluid density including sediment
ρ_z ....Out-of-plane reinforcement ratio
ρ_{sh} ....Shear reinforcement ration
ρ_w...............................Web longitudinal reinforcement ratio
σ_c ....Compressive stress
σ_t...............................Tensile stress
τ_{bFy} ....Maximum bond stress
ϕ ....Curvature

Chapter 1

Introduction and Objectives

The majority of existing structures throughout the world have been constructed following traditional, prescriptive design approaches in which structural elements are dimensioned to meet a minimum acceptable standard that aims at providing a single level of protection: life-safety. Recent natural hazard events, however, have shown that structural responses can cause community effects beyond those that threaten their occupants' lives. For instance, the 2011 magnitude 6.3 earthquake in Christchurch, New Zealand, caused 70000 people to flee the city due to post-event non-habitable homes and required a quarter of the buildings in the central business district of the city to be demolished, cordoning off the area for more than two years after the event [1]. Consequently, prescriptive design approaches, while providing a certain level of life-safety protection, provide a much lower contribution to the creation of the natural hazard resilient structures of the future.

The *performance-based engineering* (PBE) methodology, on the other hand, has been increasingly investigated and adopted as an innovative approach for the structural design and assessment of structures. Differently from the prescriptive approach, PBE provides a better understanding of the behavior of a structure under a range of loading events and help decision makers better understand the vulnerabilities of their design [2]. Following the PBE methodology, a structural design is not limited to present a life-safety level of protection; rather, it can be designed to achieve any pre-defined performance objective that may include its collapse risk, downtime, repair cost, fatalities, etc. Consequently, PBE has been predominantly applied to investigate structural performances under extreme loads such as those created by natural hazard events.

PBE relies on an accurate structural analysis method to predict the performance of the structure to the considered natural hazard loads and assess if the pre-defined desired performance has been achieved by the current design. This structural analysis requires an accurate characterization of the structure from its initial, linear-elastic to its nonlinear, near-collapse response to cover a wide range of possible performances. Since full-, or reduced-, scale experimentation would be unfeasible due to prohibitive costs, nonlinear finite element is a powerful tool for structural analysis as it allows a realistic simulation of the nonlinear behavior of structures in a way similar to physical lab tests. To ensure accurate numerical results, there is a constant need for the development of state-of-the-art numerical models that can simulate the main material and structural behaviors.

The PBE methodology can also be used to assess non-structural related performance objectives such as the environmental impacts caused by natural hazard loads. When assessing its environmental performance, however, impacts are not put into the perspective of the structure's structural performance, which may lead to the wrong conclusions, especially when two different structural alternatives are being compared. This is particularly important as the structures of the future will not only aim at being resilient but also sustainable.

The goals of this research are: i) to create state-of-the-art high-fidelity numerical models for the PBE of structures; and ii) to create a multidisciplinary framework for the resilient-based environmental impact assessment of structures subjected to natural hazard loads. These goals have been primarily investigated on reinforced concrete (RC) and cross laminated timber (CLT) structures, as the first is a traditional and resilient while the second is a newer and seemingly more sustainable structural alternative. However, the created approach can also be applied to other structural alternatives under natural hazard loads.

In pursuit of this research's goal, four main objectives were conducted, as shown in Figure 1-1.

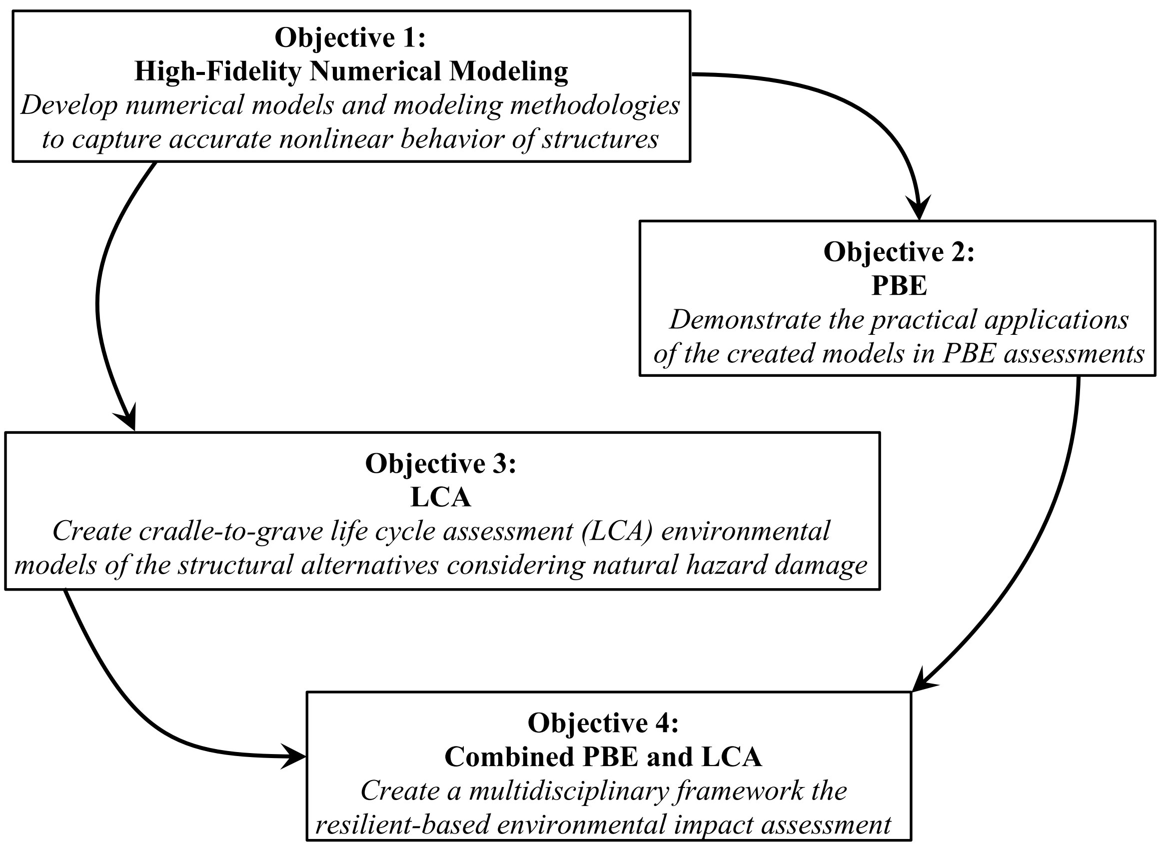

Figure 1-1: Summary of the objectives conducted in this research.

This dissertation is written in manuscript format, which means that each chapter is either a published or submitted journal or peer-reviewed conference publication. Table 1.1 summarizes each paper contained in this dissertation, which research objective it addresses, and its main contributions.

Table 1.1: Summary of each paper contained in this dissertation and their main contributions.

Paper	Chapter	Obj.	Main Contributions
Journal Paper I	Chapter 2	1, 2	• Three high fidelity numerical models of RC structures of different computational demand characteristic created • Accuracy of each model in capturing experimental response is statistically assessed • Performance-based earthquake engineering structural analyses of a previously tested RC frame performed • Structural risk to a set of performance limits is evaluated by means of fragility curves
Journal Paper II	Chapter 3	1	• A high-fidelity modeling and analysis methodology are proposed and validated for reinforced concrete elements retrofitted with fiber-reinforced polymers sheets
Journal Paper III	Chapter 4	1	• The out-of-plane behaviors of CLT connections are characterized using high fidelity numerical modeling • 48 experimentally validated high-fidelity nonlinear numerical models are developed • The influences of three key connection design parameters are statistically quantified • A mechanics-based simplified procedure is proposed for quantifying the nail contribution • A simplified equation is proposed for estimating the

Table 1.1 cont.

Paper	Chapter	Obj.	Main Contributions
			out-of-plane load capacity
Journal Paper IV	Chapter 5	3	• Environmental impacts of three different RC seismic retrofit techniques are compared • Benefits of recycling construction and demolition waste generated as opposed to landfill disposal are investigated
Journal Paper V	Chapter 6	3, 4	• A multidisciplinary framework that combines PBE with LCA to quantify and compare the resilience-based environmental impacts of two different building configurations is created • Two seven-story building configurations made from RC and CLT materials are investigated and comparative resilience versus sustainability conclusions are drawn
Conference Paper I	Chapter 7	1	• Five state-of-the-art numerical beam-column joint modelling techniques and constitutive behaviors were investigated • Conclusions drawn on the effects of beam-column joints on high-fidelity numerical models

Chapter 2

Journal Paper I - A Comparative Study on Nonlinear Models for Performance-Based Earthquake Engineering[1]

2.1 Abstract

Performance-based earthquake engineering requires a large number of nonlinear dynamic analyses to statistically assess the performance of frame structures. The complexity and high computational demand of such procedures, however, has hindered its use in practice. The objective of this study is to evaluate the performance of three numerical models with varying computational demand levels. Two nonlinear models with different complexities and one linear model with a concentrated plasticity approach were used to evaluate a reinforced concrete frame. The accuracy of the calculated responses was assessed using the experimental results. A total number of 126 dynamic analyses were performed to derive fragility curves. The nonlinear models calculated significantly more accurate structural responses than the more-commonly used plastic-hinge model. The model preparation and result acquisition times were found to comprise a significant portion of the total computational demand of each model. An overview of the performance-based

[1] Reprinted from Engineering Structures, Vol 172, Rafael A. Salgado & Serhan Guner, A comparative study on nonlinear models for performance-based earthquake engineering, 382-391, © 2018, with permission from Elsevier. For the published version, please refer to https://doi.org/10.1016/j.engstruct.2018.06.034.

modeling processes and the critical points for minimizing the computational demand while retaining the calculation accuracy are also presented.

2.2 Introduction

Performance-based earthquake engineering (PBEE) makes use of the nonlinear structural analysis (NLA) methods to accurately predict the inelastic response that most buildings undergo during seismic excitation. Amongst different NLA methods, the nonlinear dynamic analysis (NLDA) methods, also known as time-history analysis, provide the most realistic simulation of structural behavior [1-4]. Multiple NLDAs are required to assess (or design) a structure using PBEE; however, the NLDA methods are complex and computationally-intensive, which significantly limits their applicability in practical situations.

Previous studies have either focused on proposing simplified analysis procedures [4-9] to substitute the need for the NLDA methods or evaluate the influence of local element assumptions and modeling approaches on the overall structural response [10-12]. There is still a lack of studies that investigate the structural response reliability when a structural system is numerically analyzed with different modeling techniques. The objective of this research is to study various numerical modeling techniques with different complexity levels and evaluate their simulation accuracy and computational demand. For this objective, a PBEE structural assessment of a previously-tested RC frame is conducted using three modeling approaches. The calculated structural risk to a set of performance limits is evaluated by means of fragility curves.

2.3 Performance-Based Earthquake Engineering

A summary of the PBEE structural assessment is presented herein to illustrate the methodology used in this paper [13-14]. First, the building location, importance, and soil condition are used to determine the earthquake hazard level and the response spectrum of the structure as per the applicable building code. Structural analysis is then conducted using a numerical model subjected to a series of ground motion (GM) acceleration histories that match the response spectrum. The performance is evaluated based on the calculated responses and the structural risk is expressed by means of fragility (or vulnerability) curves, which indicate the probability of the structure to exceed a certain damage state (i.e., damage measures or performance levels) based on the engineering demand parameters (EDP) (e.g., story drift, floor accelerations, or velocities) calculated by the structural analysis. A loss analysis is finally conducted, based on the previously calculated probability of exceedance, to quantify the financial, downtime, casualty, or other types of loses.

2.4 Hazard Determination

In this study, the structure considered is in Portland, Oregon, USA, and constructed over 'type D' soil, which is the standard soil type in ASCE 7 [15] when no sufficient detail is provided. The design response spectrum was calculated based on the NEHRP [16] provisions.

Seven acceleration histories were considered to meet the minimum requirements of the NEHRP [16] provisions. The ground motion characteristics included: 'strike-slip' fault type, less than 50 km to the epicenter, and Richter magnitude between 6 and 8 (see Table

2.1). Time-histories were obtained from the Pacific Earthquake Engineering Research (PEER) online NGA-West2 database [17].

Table 2.1: Selected ground motion characteristics.

ID	Earthquake Name	Year	Station Name	Mag.	Epicenter Distance, km	Scale Factor
1	Imperial Valley-02	1940	El Centro Array #9	6.95	12.98	1.5
2	Imperial Valley-06	1979	Agrarias	6.53	2.62	2.6
3	Victoria, Mexico	1980	Cerro Prieto	6.33	33.73	1.2
4	Superstition Hills-02	1987	El Centro Imp. Co. Cent	6.54	35.83	1.6
5	Landers	1992	Desert Hot Springs	7.28	27.32	2.7
6	Erzican, Turkey	1992	Erzincan	6.69	8.97	1.5
7	Parkfield-02, CA	2004	Parkfield - UPSAR 13	6.00	12.59	2.6

The selected ground motions were scaled such that the average follows the requirements of NEHRP [16], with the result shown in Figure 2-1. The one-third scale frame to be examined exhibited a natural period of 0.303 s, which corresponds to a full-scale period of 0.525 s.

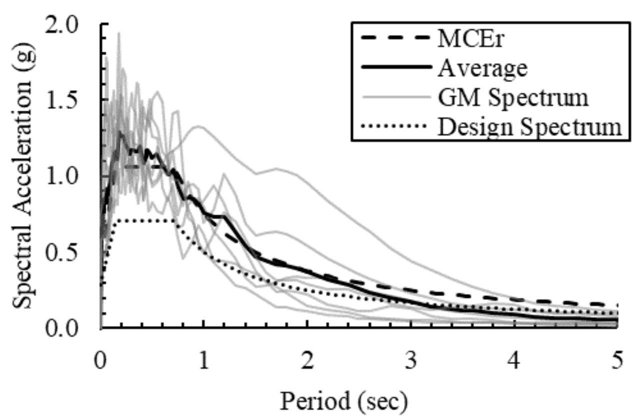

Figure 2-1: Spectral response.

2.5 Structural Analysis

A structure designed based on pre-1970s building codes was chosen for assessment using the PBEE methods due to their seismically-deficient details. The frame examined was a one-third scale, three-story, three-bay planar structure designed by Ghannoum and Moehle [18] to develop a flexure-shear-critical failure mechanism (i.e., the columns yield in flexure prior to a shear failure). Two of the columns were constructed with widely-spaced shear reinforcement (denoted as non-ductile columns), while the other two columns were designed to fulfill ACI 318-08 specifications (denoted as ductile columns). Ghannoum and Moehle [18] indicated that the mixture of older-type columns and ductile columns is not completely representative of typical 1970s construction. It was introduced in the test frame so that collapse of the frame due to the failure of the older-type columns would be slowed by the ductile columns and the dynamic failure mechanism could be more closely monitored. A strong beam-weak column mechanism was included, and the beam-column joints were designed in accordance with ACI 318-08 to avoid any joint failure prior to a column failure. Each beam carried 26.68-kN lead weight packets distributed over two points located approx. 0.4 m from the face of each column. A sketch of the frame is shown in Figure 2-2.

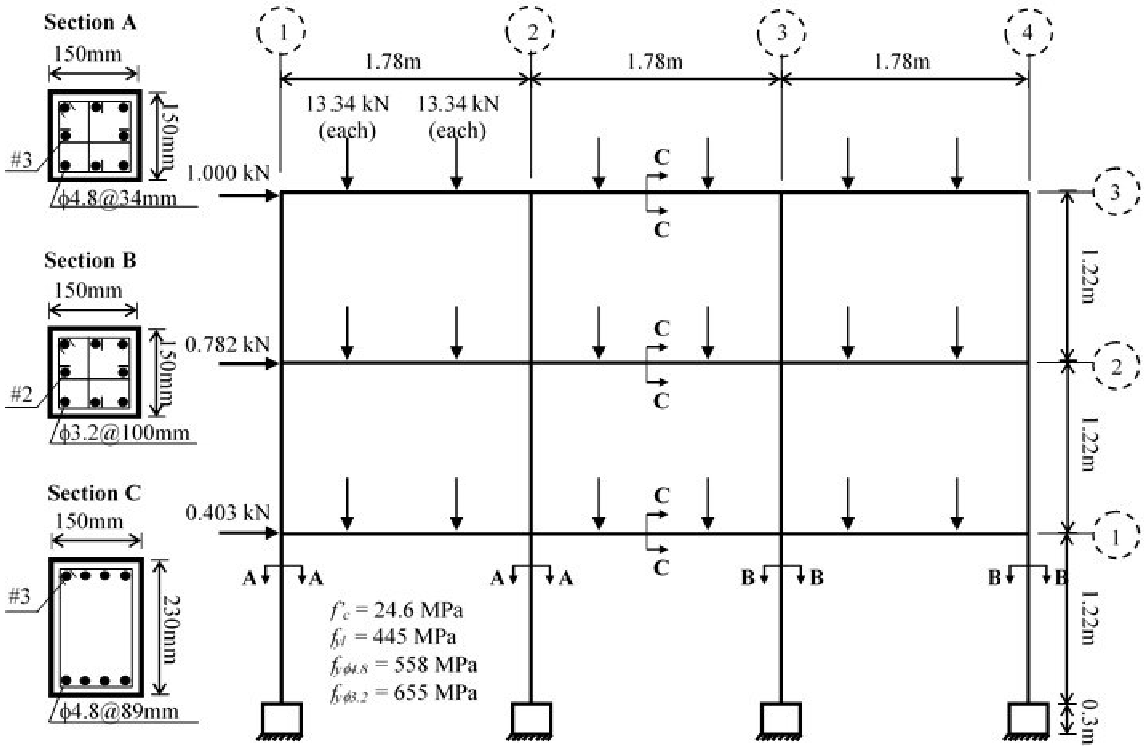

Figure 2-2: Frame and section design details.

The frame was subjected to four shake table tests using the March 3, 1985, Chile Earthquake (Llolleo Station, Component 100); namely, half-yield (HY), and dynamic tests 1, 2, and 3 (DT1, DT2, and DT3). Table 2.2 lists the ground motion scale factors and the response of the frame in each test [18].

Table 2.2: Dynamic tests and respective ground motion scale factor.

Test	GM Scale Factor	Frame Response
HY	0.3625	Minor flexural cracks.
DT1	4.06	Column 3 shear and axial failure at 5.2% story drift.
DT2	4.06	Column 4 advanced shear damage. No failure.
DT3	5.80	Column 4 failure. Partial collapse of frame's east side.

2.6 Numerical Modeling

In this study, three numerical models were created. A full nonlinear model that employs distributed-plasticity fiber-based elements, called Nonlinear Fiber-Based (NLFB) model; a simplified nonlinear model with fewer and longer flexure-only elements with combined shear-hinges, called Nonlinear Fiber-Based Shear Hinge (NLFBSH) model; and a fully-elastic model with concentrated flexure, axial, and shear-hinges, called Elastic with Concentrated Plasticity Hinges (ECPH) model. All models used two-dimensional beam-column elements due to their computational efficiency and analytical accuracy.

2.6.1 Nonlinear Fiber-Based Model (NLFB)

The NLFB model employed the frame element developed by Guner and Vecchio [19]. This element performs interrelated global and sectional analyses, where the internal forces calculated by the former are used to perform the latter. It is based on the Modified Compression Field Theory (MCFT) [20], which allows the element to account for the coupled flexure, axial and shear effects. Additionally, the MCFT uses the average and local strains and stresses of the concrete and reinforcement, and the widths and orientations of cracks throughout the load-deformation response of the element. Shear strains are calculated using a parabolic strain distribution [19]. The element employs a smeared, rotating crack approach based on a total load, secant stiffness formulation. The triaxial concrete core confinement is inherently accounted for through the use of in- and out-of-plane reinforcement ratios. In addition, it incorporates several second-order material behaviors that are specific to reinforced concrete structures, as listed in Table 2.3 [21].

Table 2.3: Material models and second-order behaviors considered.

Material behavior	Default model
Compression softening	Vecchio 1992-A
Tension stiffening	Modified Bentz 2003
Tension softening	Linear
Confinement strength	Kupfer/Richart
Crack width check	Max crack width of Agg/5
Rebar dowel action	Tassios (Crack slip)
Rebar buckling	Refined Dhakal-Maekawa

The structure was modeled using the computer program VecTor 5 [22, 23]. The structural analysis package also incorporates graphical pre- and post-processor programs. FormWorks Plus [24, 25] is a graphical pre-processor developed specifically for the VecTor suite of applications to provide better modeling capabilities such as the list of available elements and material models, auto-meshing and auto-substructure features. The post-processor program Janus [26, 27] can display the displaced shape of the structure, crack widths, locations and propagation, rebar and concrete stresses and strains, and failure conditions. The post-processor program is a critical component of structural assessment process since they aid analysts to understand the structural behavior, detect modeling mistakes, and effectively compare the calculated responses. Some important capabilities of the computer program VecTor5 are summarized in Table 2.4.

Table 2.4: Summary of each computer programs capabilities.

	Vector 5	OpenSees	SAP2000
Nonlinear Analysis	✓	✓	
Coupled Interaction	F-A-S	F-A	F-A
Second-Order	✓		
Monotonic	✓	✓	✓
Dynamic/Cyclic	✓	✓	✓
Pre-Processor	✓		✓
Post-Processor	✓		✓
Organized Manual	✓		✓

F – Flexure; A – Axial; S – Shear.

The concrete uniaxial stress-strain response was modeled using the Popovics and Modified Park-Kent models for the pre- and post-peak responses [21]. The steel reinforcement stress-strain response is composed of three parts: linear-elastic response, yield plateau, and a nonlinear strain-hardening phase until rupture in tension, and a buckling response in compression (see Figure 2-3). As recommended by [19], each beam and column was divided into elements of about half of its cross-section height (see Figure 2-4), and the number of fibers used in all cross-sections was kept at about 30 fibers. The longitudinal reinforcement was discretely modeled while the shear reinforcement was smeared into relevant concrete layers.

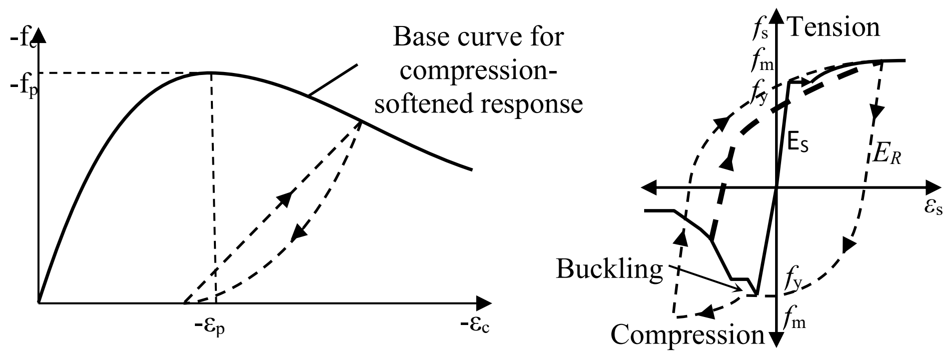

Figure 2-3: NLFB hysteretic concrete and steel reinforcing material models.

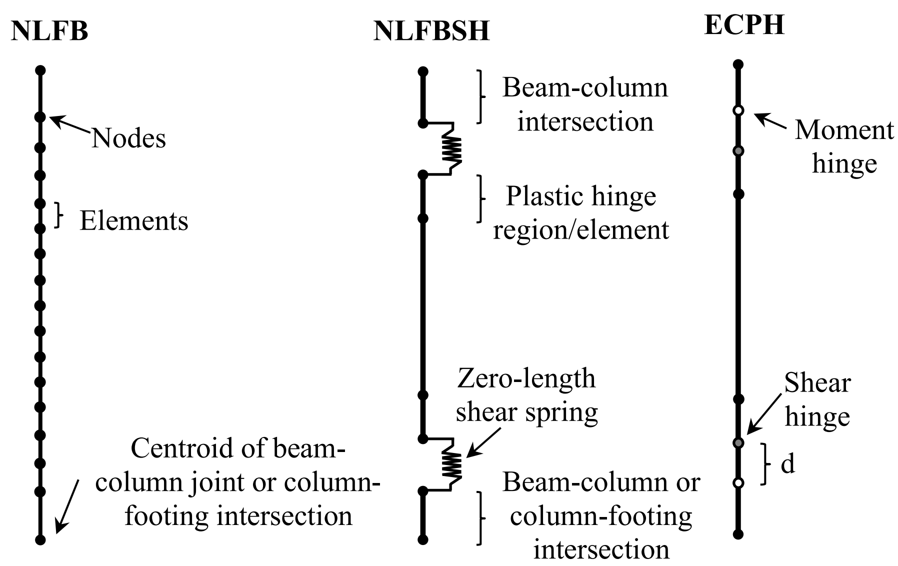

Figure 2-4: Beam-column element model approaches.

The NLFB model incorporated a nonlinear concrete model with plastic offsets proposed by [28]. In this model, the concrete unloads to a plastic offset strain, not to the origin of the stress-strain diagram, following a nonlinear Ramberg-Osgood formulation. The reinforcing steel hysteretic response was based on the Seckin model with Bauschinger effect [29] in tension, and the refined Dhakal-Maekawa model for compression [21] as shown in Figure 2-3. The primary energy dissipation mechanism considered in this study occurred due to the nonlinear hysteretic material constitutive models incorporated in each numerical model. Consequently, no additional damping was necessary, due to the fully nonlinear elements of the NLFB model. However, for all the models in this study, the dynamic analyses were performed based on the average Newmark integration method, which typically requires a minimal amount of damping for numerical stability. The NLFB model achieved numerical stability with a Rayleigh damping ratio of 0.5% for the first two modes, in addition to an inherent hysteretic damping.

2.6.2 Nonlinear Fiber-Based Shear-Hinge Model (NLFBSH)

The NLFBSH model was utilized in this study to serve as a simplification of the NLFB model. Consequently, fewer and longer elements were included with a simplified material model formulation. The material constitutive models incorporated the flexure and axial effects only. Second-order reinforced concrete material behaviors were not included (see Table 2.4). To account for the shear effects, localized shear-hinges were incorporated (see Figure 2-4). These simplifications were made to reduce the computational effort while still modeling the critical global structural response mechanisms.

The mesh consisted of closely-spaced elements in series with uncoupled shear-springs at the ends of the beams and columns (i.e., the regions where most of the inelastic deformation was likely to occur). Longer elements were used in between the ends of the beams and columns due to the reduced inelastic response of these regions (see Figure 2-4). This mesh layout was based on a study conducted by Leborgne and Ghannoum [30].

The model was developed in OpenSees [31]. OpenSees is the only structural analysis package in this study with no pre- or post-processor capabilities. The output is given in a numbered-list, text-file format, leaving the interpretation to the discretion of the analyst. Additionally, the program requires input text files written in the tcl programming language, which greatly limits the use of OpenSees to researchers and expert engineers with significant knowledge on computer programming and nonlinear structural modeling (see Table 2.4).

The constitutive model of the shear-hinge developed by Leborgne and Ghannoum [30] was employed based on the rotation of the plastic-hinge element (see Figure 2-4). The spring exhibits stiffness degradation with hysteretic and pinching cyclic response, as shown in Figure 2-5. The rotation-based shear failure was based on an element which yields in flexure prior to a shear failure. The nominal shear strength was calculated as per ASCE 41 [32], with 20% residual strength, and the degradation stiffness was calculated using a regression model calibrated with 56 flexure-shear-critical column experiments. The plastic-hinge length was conservatively chosen to be 1.5 times the cross-section height to contain the plastic rotation [30].

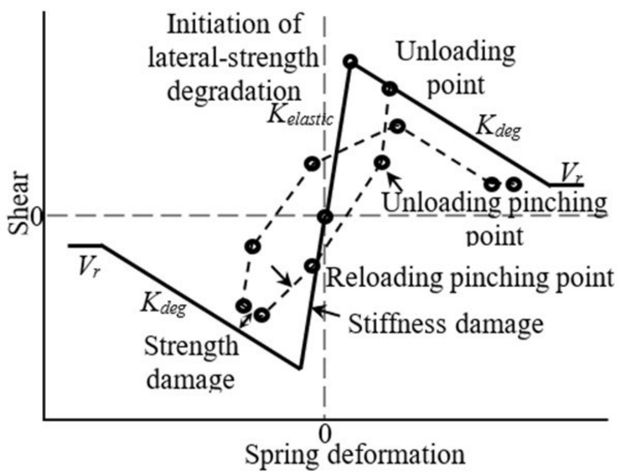

Figure 2-5: Shear-hinge nonlinear model [30].

The concrete constitutive compressive stress-strain distribution was modeled using the Hognestad parabola and linear models for the pre- and post-peak responses [33]. OpenSees does not automatically consider concrete confinement due to shear reinforcement. Thus, the core concrete properties had to be calculated using a suitable model [34]. The longitudinal steel reinforcement was discretely modeled with the three-partite stress-strain response, similar to the NLFB model (see Figure 2-6a).

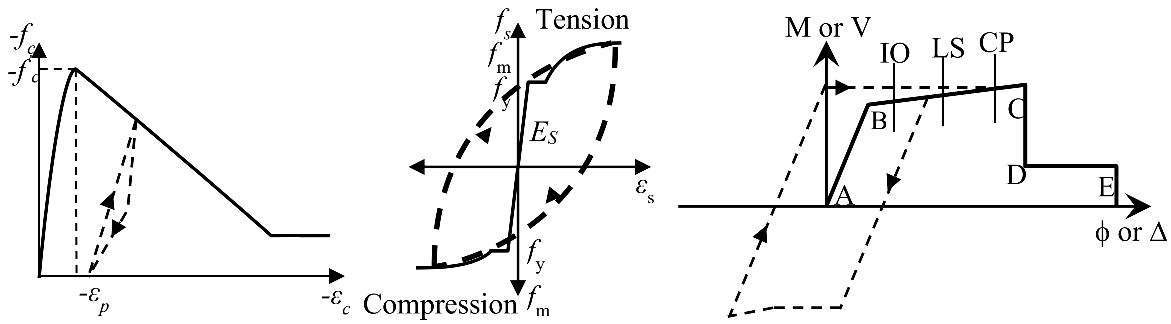

(a) **(b)**

Figure 2-6: a) NLFBSH hysteretic concrete and steel reinforcing material models; b) ECPH hysteretic model.

The NLFBSH model employed a trilinear concrete hysteresis model with pinching effects developed by Filippou [33]. The concrete unloads to a plastic strain following a linear path. The reinforcing steel hysteretic model was incorporated using the Menegotto-Pinto model (see Figure 2-6a). A Rayleigh damping ratio of 3% for the first two modes was required for numerical stability, in addition to the hysteretic damping. The damping ratio used in the NLFBSH model was considerably higher than the ratio used in the NLFB model (i.e., 0.5%) due to the reduced number of elements, the simpler constitutive models, and the mix of nonlinear (i.e., full hysteretic behavior) and linear elements (i.e., no hysteretic behavior) employed by the NLFBSH model.

2.6.3 Elastic with Concentrated Plasticity Hinges Model (ECPH)

The ECPH model was the simplest model considered in this study to evaluate the accuracy of the linear-elastic models with concentrated plasticity hinges under dynamic loads. In this model, each beam or column was modeled using linear-elastic elements. The concentrated-plasticity hinges were the only mechanism that simulated material's nonlinear behavior of the elements. Geometric nonlinearities were included based on large displacement and P-delta effects. The constitutive model of the hinges was derived as per the recommendations in ASCE 41 [32] (see Figure 2-6b). In this model, point B represents hinge yielding; point C represents the ultimate capacity of the hinge; and points D and E represents the residual strength and total failure conditions, respectively. ASCE 41 [32] defines three building performance levels: immediate occupancy (IO), life safety (LS), and collapse prevention (CP), as shown in Figure 2-6b. Despite the nonlinear behavior of the hinge, the concentrated-plasticity hinges do not typically account for the nonlinear state of the element; rather, they limit the load capacities of the elements (i.e., moment, shear, or axial) at the specific location at which they are placed.

The model was developed using the computer program SAP2000 [35]. The SAP2000 package includes powerful pre- and post-processing capabilities (see Table 2.4). However, since the focus of the program is on elastic analysis of structures, these tools are limited to structural information predominant of elastic models. SAP2000 post-processor displays the deformed shape of the structure, element forces diagrams, and hinge response with distinct hinge colors. No cracking information is displayed (i.e., the elastic elements do not simulate the cracked conditions) and no concrete or reinforcement stress-strain response is calculated.

The coupled flexural-axial and uncoupled shear-hinges were used in the beam-column elements. The flexure-axial hinge response was used as automatically calculated by SAP2000, which is based on ACI 318-02 [35]. The shear-hinge response, on the other hand, was manually calculated to conform with the newer ACI 318 [36]. Flexure-axial interaction hinges were incorporated at the face of the beam-column or column-footing interfaces. Shear-hinges were placed d away (i.e., the effective depth of the element) from the beam-column or column-footing interface as per ACI 318 [36] (see Figure 2-4). For the hinge lengths, CSI [35] recommends a moment-hinge length to be equal to the cross-sectional height. However, no information is given for the shear-hinge lengths. A shear-hinge length of 1.5 times the cross-section height was adopted as in the NLFBSH model. To account for the cracked conditions of the members, the moment of inertia of the elements was reduced by factors of 0.35 and 0.7 for beams and columns, respectively, as per ACI 318 [36].

The ECPH model employed no hysteretic material behavior in its linear-elastic elements. Only the nonlinear-hinges exhibited a simple hysteretic response. The hysteretic model of the hinges followed a linear path as shown in Figure 2-6b. By default, SAP2000 limits the unloading of the hinge (i.e., CDE path in Figure 2-6b) to follow a negative stiffness path of 10% the elastic stiffness of the hinge (i.e., AB path in Figure 2-6b). This limitation is intended to avoid 'unrealistic' sudden strength loss of strength of ductile elements. However, due to the brittle nature of the shear-hinge, sudden strength loss represents the realistic behavior. Thus, brittle failure of the shear hinges was considered using the recommended element subdivision of 2% or 0.02 [35]. A Rayleigh damping ratio of 5% was used for the first two modes as per ASCE 41 [32] due to the fully-elastic elements employed.

2.6.4 Mechanisms Not Included

The beam-column joint and bar-slip damage mechanisms should be included in the numerical models of the pre-1970s structures. However, the joints of the frame examined in this study were designed as per the modern seismic codes to prevent beam-column joint failures. Consequently, rigid end offsets were incorporated in the beam-column and column-footings connections in this study.

2.7 Numerical Models Calculated Response

A dynamic time-history analysis was performed to evaluate the simulation accuracy of the developed models. The dynamic acceleration-history was obtained from the shake table tests performed by Ghannoum and Moehle [18]. To increase the convergence and accuracy of the calculated results, each data point of the experimentally recorded shake-table time-history data was linearly divided into 100 sub-steps [37]. The calculated results were compared with the experimental values in terms of the base shear, first-story drift, damage progression, and failure conditions.

The NLFB and the NLFBSH models were subjected to the half-yield test so that the cracked structural condition could be included at the start of the dynamic test 1. The half-yield test does not affect the ECPH model since it does not simulate cracking in its members. The first-story drift and base shear responses of each model in dynamic test 1 are shown in Figure 2-7. The drift was calculated as the average of the displacements of the nodes at the first-floor level divided by the height of the first-floor.

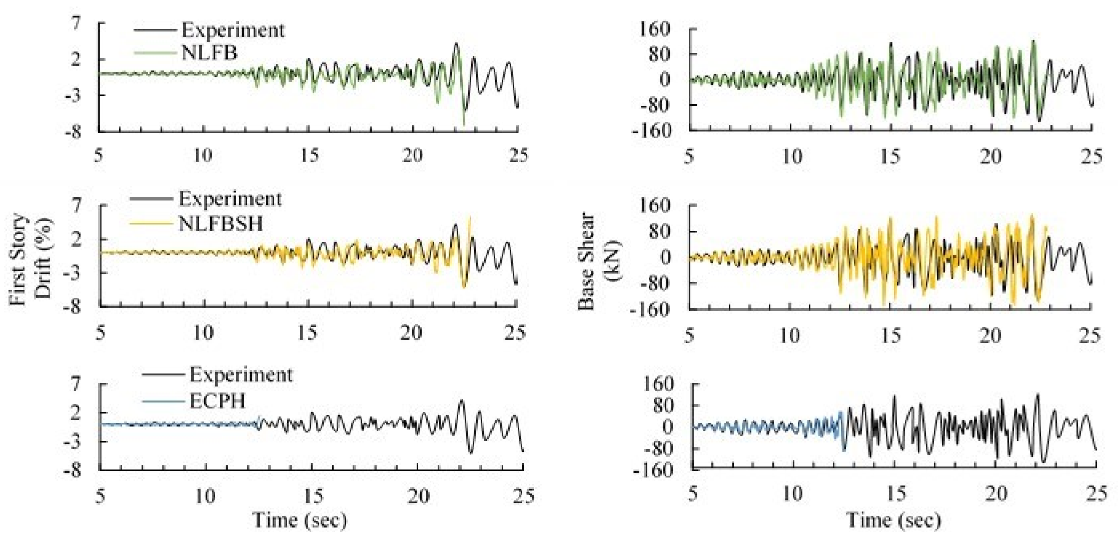

Figure 2-7: Numerical models and experimental first-story drift and base shear responses for dynamic test 1.

The NLFB and the NLFBSH models failed at the first story level of column 3 at a time of approx. 22 seconds (see Figure 2-7 and 2-8), which correlated well with the 22.5 seconds at which the shear failure occurred in the experiment. Furthermore, the calculated first-story drift and base shear values corresponded reasonably well to the experimental response with the calculated-to-experimental discrepancies below 15%, as shown in Figure 2-9. The ECPH model failed at a significantly lower time of 12.6 seconds (see Figure 2-7) and calculated the highest deviation from the experimental response (see Figure 2-9). The maximum calculated drift ratio corresponded to 27% of the maximum experimental response and the base shear resistance was 67% of the resistance obtained experimentally. The ECPH model resulted in a significant underestimation of the structural capacity due to the failure of the moment hinge at the first story level of column 3 (see Figure 2-8). Note that the failure calculated by the ECPH model could not capture the lack of shear capacity of the specimen. The use of code-prescribed axial-flexure and shear resistances, used for the plastic hinges capacities, could not accurately predict the response of the building during the dynamic load.

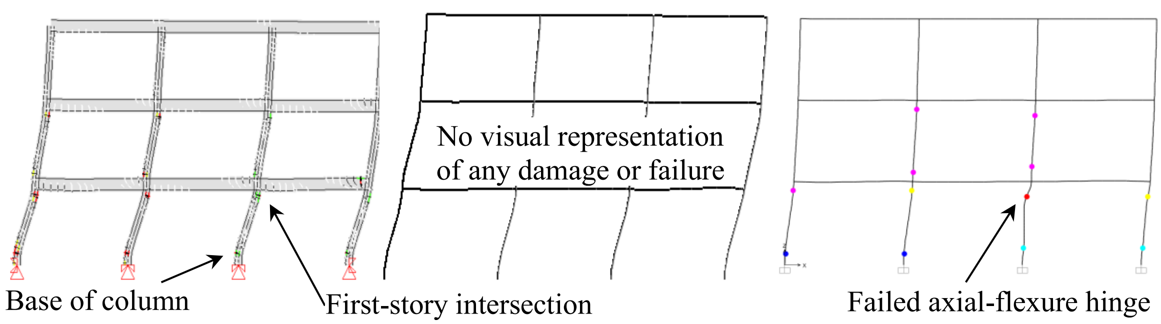

Figure 2-8: Failure load stage for a) NLFB, b) NLFBSH, and c) ECPH models.

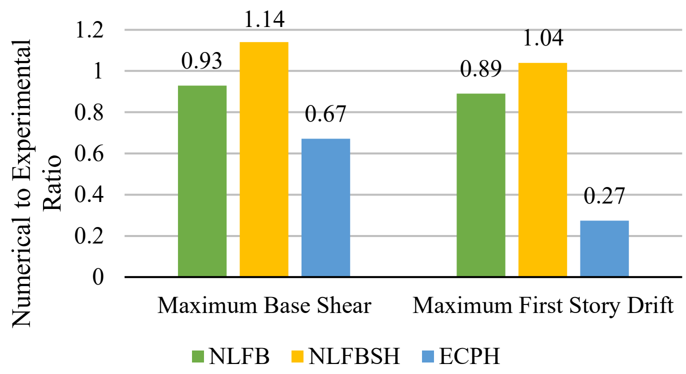

Figure 2-9: Numerical to experimental ratio in dynamic test 1.

Figure 2-10 shows the hysteresis responses obtained from each model and the envelope of the experimental response. The NLFB and the NLFBSH models satisfactorily captured the experimental responses. The ECPH model calculated a slightly stiffer response due to the use of the cracked moments of inertia for the columns and beams, as per ACI 318 [36]. The hysteretic response of the ECPH model stopped at the failure of the moment hinge shown in Figure 2-8. The inability of the numerical model to account for the force redistribution after the hinge failure resulted in a numerical instability and terminated the entire analysis (see Figure 2-10).

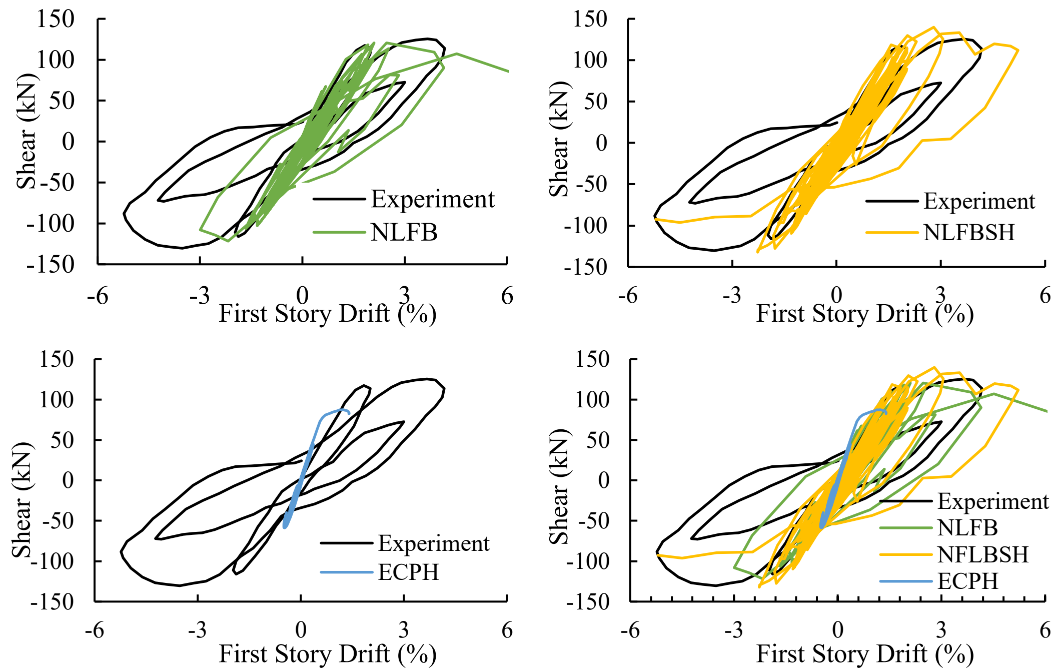

Figure 2-10: Numerical models and experimental hysteresis response.

2.7.1 Time Demand

The total time demanded by a numerical analysis can be divided into three phases: the development time, the analysis time, and the results acquisition time. The development time is the time required to develop and create the model, i.e., selecting the appropriate material models, element types, creating nodes, element connections, applying loads, etc. The analysis time is the time required for the computer to execute the structural analysis. The results acquisition time is the time required to understand the analysis results, such as the failure modes, failure progression, stresses, strains, etc., and extract several types of data to create load versus deflection and other plots. While the analysis time is a pure computational process, with no analyst involvement, the model development and result acquisition times demand significant hands-on effort from the analyst. Consequently, the consideration of the model development and result acquisition times is critical when assessing the practicality of any numerical analysis procedure.

In Figure 2-11, the total time demanded by each numerical model developed in this study is presented. The time required by each model was visually broken down into the three phases discussed above. It should be noted that the model development and result acquisition times will vary from analyst to analyst. In this study, these times were consistently obtained by a single analyst with similar levels of previous experience with each software program used.

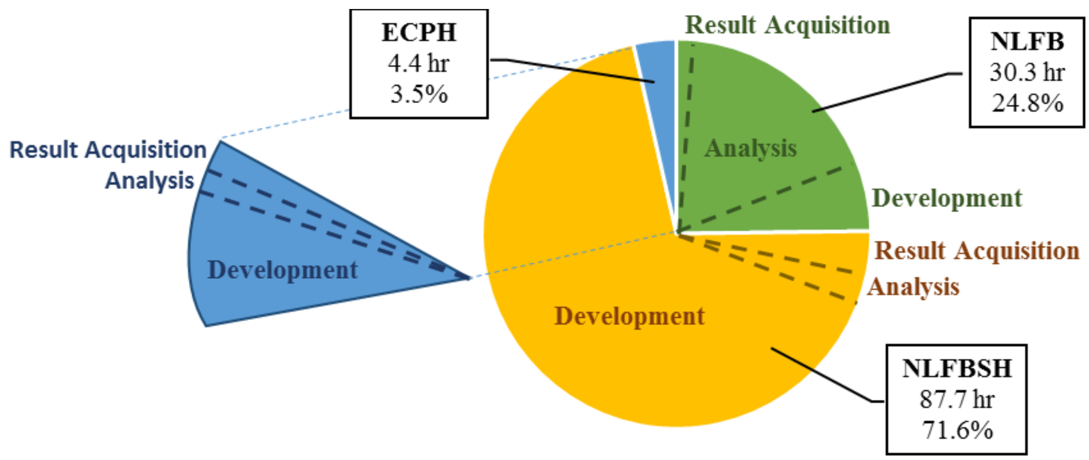

Figure 2-11: Total time demanded by each numerical model.

The numerical model with the highest computational time demand was the NLFBSH model due to the very high model development time (i.e., approx. 80 hours). This was caused by the lack of any user interface such as a pre-processor program, and limited and inconsistent users' manual for the use of available elements and models. These drawbacks made the modeling process difficult and tedious, requiring the analyst to make use of trial-and-adjustment methods in the model preparation phase, which significantly increased the time demanded. In general, a user-friendly interface and a well-presented and comprehensive documentation are essential in minimizing the model development time and modeling mistakes. Both the NLFB and ECPH models possessed these features, which translated into a much lower model development time of approx. 8 and 4 hours, respectively.

The analysis time required by the numerical models was, as expected, directly proportional to the comprehensiveness level of each model. The type of the analysis performed was also highly influential on the analysis time demand. The time-history dynamic analyses, for example, required significantly more analysis time due to the large number of acceleration points considered. The half yield and the dynamic test 1 were comprised of 900 and 1500 thousand acceleration points, respectively. For each of these points, iterations were performed to achieve numerical convergence by means of matrix algebra; the analysis time spent on each iteration was directly proportional to the stiffness matrix size and the material modeling formulation. Consequently, the NLFB model, which considered the most comprehensive material modeling and employed the highest number of nodes and elements (see Figure 2-4), required the highest analysis time of approx. 22 hours (see Figure 2-11). The NLFBSH model and the ECPH model had the second and third longest analysis time of approx. 2.7 and 0.08 hours (i.e., 5 minutes), respectively. All analyses were performed on an Intel® Core™ i5-2500 quad-core 3.3GHz CPU with 8GB DDR3 1333MHz RAM.

The result acquisition time, similarly to the model development time, highly depended on the availability of a graphical post-processing program. Consequently, the model with the highest result-acquisition time was the NLFBSH model with approx. 5 hours. In addition to the drawbacks mentioned for the model development time, the NLFBSH model output the analysis results in text files, which required additional effort from the analyst to translate and interpret the tabulated results into meaningful structural response information. The availability of powerful post-processing tools for both the NLFB and ECPH models resulted in a significantly lower result acquisition time of approx. 0.5 and 0.3 hours, respectively (see Figure 2-11), and encouraged a more thorough examination of the analysis results.

2.8 Performance Assessment and Fragility Functions

Fragility functions, which defines the probability of incurring a performance limit as a function of ground motion intensity [14], were derived to study the probability of exceeding the performance levels considered in this study. The performance of the structure was quantified by comparing the calculated engineering demand parameters (EDP), in terms of maximum first-story drift (θ_{max}), to the three performance levels of immediate occupancy (IO), life safety (LS), and collapse prevention (CP) as per ASCE 41 [32]. The spectral acceleration, S_a, was chosen as the intensity measure parameter for the ground motions.

The choice of which damage measure the structure is going to be assessed for is a subject that depends on regulatory agencies, code specifications, and the building owner requirements. The maximum drift ratio for the IO is commonly considered to be the value at which the frame enters the inelastic range. A drift ratio of 1.5% was determined from the results of a pushover analysis, conducted using the NLFB analysis, for the IO performance level. The LS drift ratio was established as 2% as per FEMA 356 [38] and ASCE 41 [32]. The CP drift ratio was taken as approx. 3%, which represented 75% of the ultimate drift ratio [39].

The fragility curves were derived using a cumulative probability distribution as per Eq. (1).

$$P[d \geq D] = 1 - 1/2\left\{1 + \text{erf}\left[\frac{ln\left(\frac{D}{\mu}\right)}{\frac{\beta}{2}}\right]\right\} \tag{1}$$

where P[d≥D] indicates the probability of the defined engineering demand parameters (EDP) (i.e., drift ratio in this study) to exceed the allowable threshold D (i.e., IO, LS, or CP θ_{max}); erf is the Gauss error function; μ is the median value of the EDP at a given ground motion intensity; and β is the standard deviation of the natural logarithm of the ground motion index of the damage state. The median value of the EDP is calculated by exponential regression of the θ_{max} - Sa plot (see Figure 2-12).

A parametric study using the seven previously selected ground motions was performed. Each ground motion was scaled several times to produce a range of spectral accelerations at the first natural period of the structure. The imposed spectral accelerations were: 0.3g, 0.6g, 0.8g, 1g, 1.25g, and 1.5g. A total of 126 NLDAs were performed (i.e., 42 for each numerical model). Approx. 260 hours of analysis time were required to perform all the NLDAs, excluding the model development and result acquisition time.

In Figure 2-12a, b, and c, the black diamond-shape points are the recorded maximum first-story drifts calculated by the numerical models on each nonlinear dynamic analysis. The red lines show the standard deviation from the mean, expressed by the red 'x' point. Calculated drifts within the standard deviation lines are considered 'normal', whereas the drifts that fall above or below the standard deviation are considered 'abnormally' high or low, respectively, for the collected dataset. The dotted black lines show the exponentially fitted curve from all the first story-drift points, which was used in

Eq. (1) to calculate the fragility curves. In Figure 2-12c, the variability of the calculated maximum first-story drifts is presented by the means of the coefficient of variation. In Figure 2-12d, the statistical box and whiskers plot is presented, where the calculated maximum first-story drift are clustered in their respective quartiles. The outlier data points represent 'abnormal' values, calculated as the drifts that exceeded 1.5 times the interquartile range from the first (if below) or third quartile (if above).

When compared to the NLFB model, the structural response calculated by the NLFBSH model provided a slightly better statistical fit in this study. In Figure 2-12a, b, and c, the NLFBSH model had the lowest number of calculated drifts outside the plus or minus standard deviation range (i.e., 6 points compared to 10 from the NLFB model). In Figure 2-12d, the NLFBSH model is shown to have a slightly lower coefficient of variation, when compared to the NLFB model. In Figure 2-12e, the NLFBSH model calculated three outlier points, while the NLFB model calculated four. The ECPH model provided the poorest data dispersion and curve fitting characteristics of all three models (see Figure 2-12c and d). Structural collapses were calculated even at low spectral ground motion acceleration levels: for the spectral acceleration above 1g, all the ground motions calculated a structural failure. This response of the ECPH model resulted in considerably high drift values. Consequently, the coefficient of variation of the ECPH model up to the 0.8g spectral acceleration was the highest of all three models while for spectral accelerations above 1g, the coefficient of variation of the ECPH model was the lowest of all three models. The low calculated coefficient of variations does not mean that the ECPH model was the most precise, but rather that all the calculated drifts were uniformly high (i.e., due to failure), resulting in a low variation.

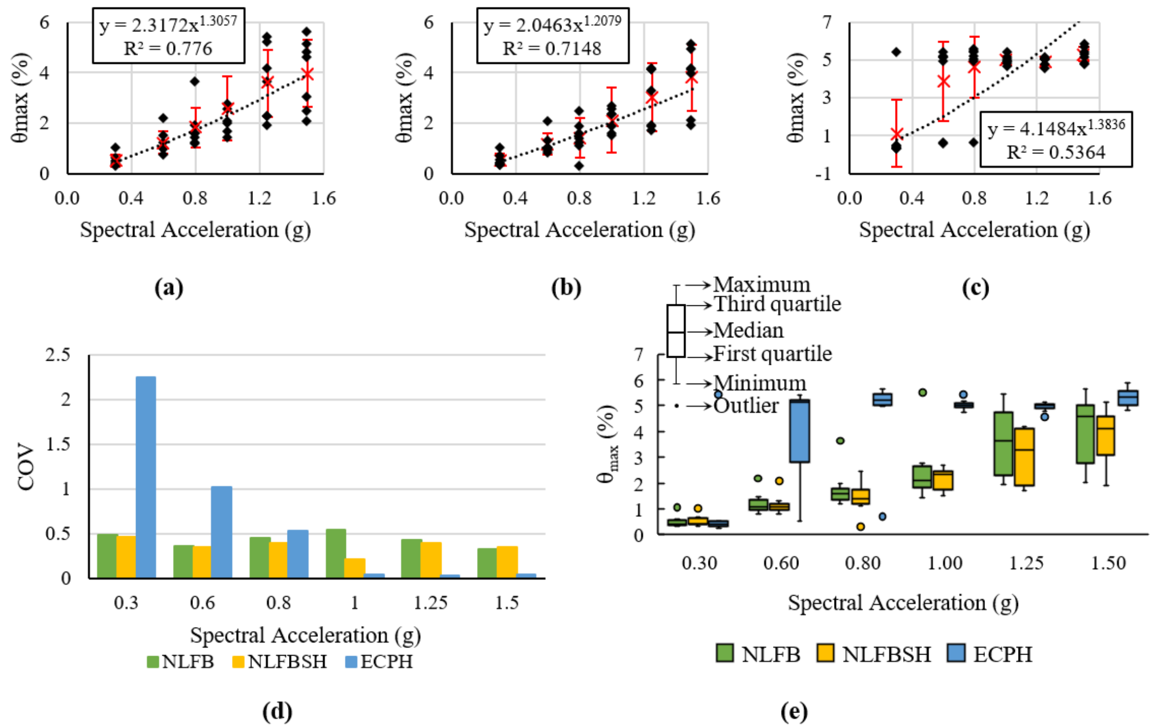

Figure 2-12: Calculated structural response for models (a) NLFB, (b) NLFBSH, (c) ECPH, (d) coefficient of variation comparison, and (e) response distribution.

The developed fragility curves for the three performance levels considered are shown in Figure 2-13. When the NLFB and NLFBSH models were considered, the calculated probability of exceedance was similar for all the performance levels, with the highest calculated difference between the models occurring at the CP level. The NLFB model calculated a higher, more conservative probability in all performance levels for lower-to-medium spectral acceleration ground motions whereas, in the high spectral acceleration ranges, the NLFBSH model calculated the highest probability. Figure 2-14a shows that the maximum difference in the probability calculated by both models was approx. 20% in all the performance levels. The ECPH model calculated the most conservative results due to the higher overestimation of the drift response of the structure caused by the inability of the ECPH model to redistribute forces once the first hinge fails. It presented a significant deviation from the other two models; the maximum difference in calculated probability of the ECPH and the other two models (see Figure 2-14b and c) was approx. 40% and 55% in all performance limits for the NLFB and NLFBSH models, respectively.

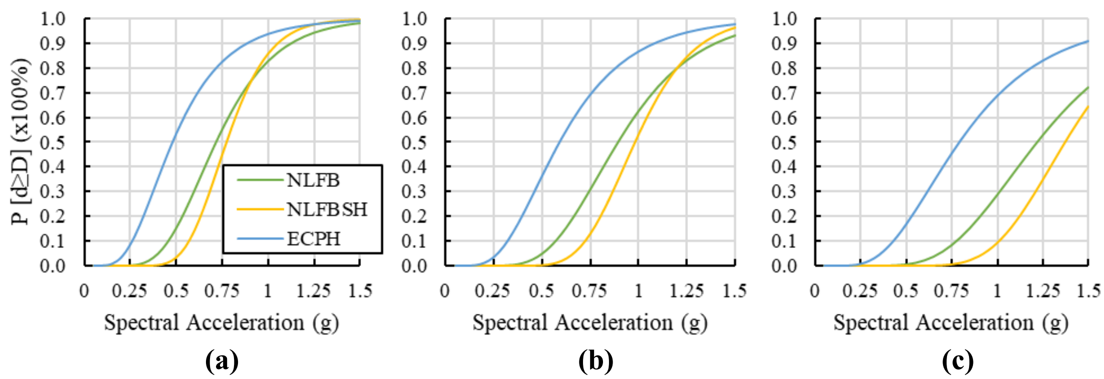

Figure 2-13: Fragility functions for the (a) immediate occupancy (IO), (b) life safety (LS), and (c) collapse prevention (CP) performance levels.

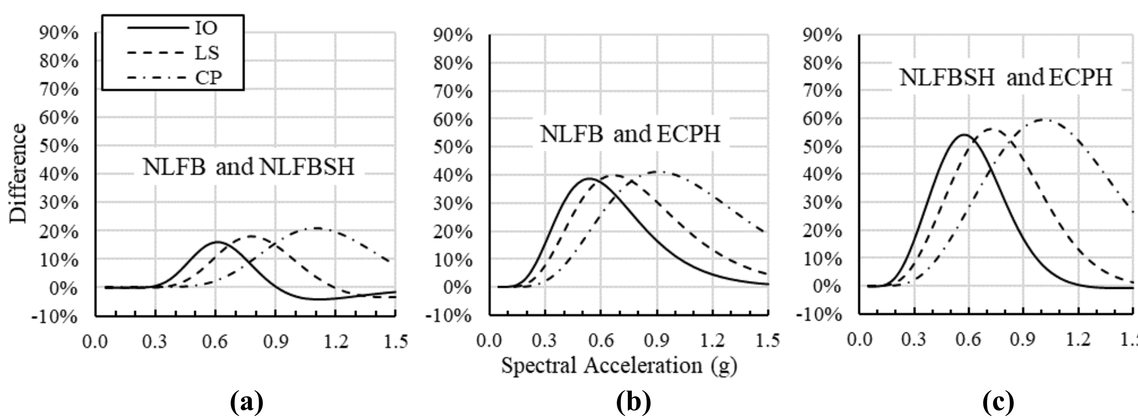

Figure 2-14: Calculated probability difference between (a) NLFB and NLFBSH, (b) NLFB and ECPH, and (c) NLFBSH and ECPH numerical models.

The accuracy of the response calculated by the NLFBSH model was similar to that of the NLFB model despite its simplified material model formulation (i.e., no coupled shear effects, no second-order behaviors) and element layout. It should be noted, however, that the frame examined primarily exhibited a column shear failure, which was accounted for the by the NLFBSH model. If other failure mechanisms had played a more significant role, the prediction accuracy of the NLFBSH model would have deteriorated significantly.

2.9 Summary and Conclusions

Three numerical models with different computational demand characteristics were created to evaluate their effectiveness in a performance-based earthquake engineering analysis. A nonlinear fiber-based numerical model (called NLFB), a simplified nonlinear model with coupled axial-flexure and uncoupled shear-hinges (called NLFBSH), and a fully-elastic numerical model with simplified nonlinear plastic hinges (called ECPH) were studied. The performance assessment of a planar reinforced concrete frame was performed employing each numerical model developed. The nonlinear dynamic analysis was performed to verify the accuracy in capturing the experimentally observed behavior and obtain the required computational time demand of each model. A set of seven ground motion acceleration histories were used to determine the calculated performance level, statistical parameters, and derive fragility curves for each of the studied models.

The findings of this study support the following conclusions:

- The developed nonlinear models satisfactorily predicted the drift and base shear responses of the studied structure within 15% deviation from the experimentally observed behavior. The ECPH model significantly underestimated the structural capacity by 40% and the drift response by a factor of four. The inability of the ECPH model to redistribute forces once a plastic hinge fails resulted in the premature termination of the analysis and, thereby, provided an unrealistically high underestimation of the structural capacity.

- The plastic hinges used in the ECPH model could not predict shear failure observed in the experimentally tested specimen. The ECPH model calculated an axial-flexural failure mode, without triggering the shear plastic hinges. Thus, the use of the axial-flexural and shear capacities provided by the ACI building code in the plastic hinges of the ECPH model did not result in an accurate structural response in the dynamic analyses performed.
- The structural response calculated by the NLFB and the NLFBSH model presented a similar overall fit to the four studied statistical parameters, i.e., curve-fitting, number of calculated drifts outside the plus or minus standard deviation range, coefficient of variation, and outlier points. The NLFBSH model however, presented the best statistical fit and, in this study, it was the most suitable model to provide a statistically meaningful performance-based assessment of the studied structure.
- Despite the use of a simplified modeling approach in the NLFBSH model, the fragility curves derived in this study calculated a 20% maximum difference probability between the NLFB and NLFBSH models for all the studied performance limits. Thus, simplified nonlinear models can be used for performance-based analysis to maintain a reasonable level of accuracy while significantly reducing the analysis time demand. Caution should be exercised for cases in which the simplified model may lead to inaccurate results due to the high reliance on the prior knowledge of the governing material behaviors and failure modes, which are not typically known for real structures.

- The fragility curves derived with the ECPH model calculated an unrealistically high probability of structural exceedance of all the three performance limits studied (i.e., immediate occupancy, life safety, and collapse prevention). The reason for this was the combination of the inability of the ECPH model to perform force redistribution once the first plastic hinge failed and the conservative hinge capacity provided by ACI building code.
- When evaluating the required time demand of a numerical model, little or no attention is given to the model development and result acquisition phases. In this study, the model development and result acquisition times represented a significant part of the numerical modeling process, when considered from start to finish. The availability of graphical pre- and post-processor programs and a well-organized user documentation were essential in reducing the model development and result acquisition times. The NLFBSH model, which lacked pre- and post-processors and a well-organized user documentation, required a much longer total time – more than twice that of the NLFB and ECPH models combined – despite having a shorter analysis time.
- The analysis time of each model increased exponentially with the number of material behavior models and elements used. Thus, there is a need for simple but accurate nonlinear dynamic analysis methods due to the large number of analyses required by the performance-based earthquake engineering methodology.

2.10 Acknowledgments

The authors would like to thank Wassim M. Ghannoum for providing the experimental shake-table ground motion data for the frame examined in this study.

Chapter 3

Journal Paper II - A Numerical Analysis Methodology for the Strengthening of Deep Cap Beams[2]

3.1 Abstract

A significant number of in-service bridges have been subjected to loads above their original design capacities due to the increase in traffic and transported freight in the past decades. Externally bonded fiber reinforced polymers (FRP) is a non-destructive retrofit technique that has become common for the strengthening of overloaded cap beams of bridges. However, there is a lack of analysis methods for the retrofitted cap beams that can accurately predict the retrofitted structural response while accounting for the critical material behaviors such as bond-slip relationships, confinement effects, and redistribution of stresses. In this study, an analysis methodology using nonlinear finite element models is proposed for cap beams retrofitted with externally bonded FRP fabrics. A two-stage verification of the proposed methodology was employed: a constitutive modeling and critical behavior of materials verification using experimental results available in the literature; and a system-level load capacity determination using a large, in-situ structure.

---

[2] Reprinted from ACI Technical Publication, Vol 333, Rafael A. Salgado & Serhan Guner, A Numerical Analysis Methodology for the Strengthening of Deep Cap Beams, 1-18, © 2019, with permission from the American Concrete Institute (ACI). For the published version, please refer to https://www.utoledo.edu/engineering/faculty/serhan-guner/docs/JP14_Salgado_Guner_2019.pdf.

The proposed methodology was able to capture the FRP-concrete composite structural behavior and the experimentally observed failure modes. The FRP retrofit layout created using the results of this study increased the capacity of the initially overloaded cap beam in 27%, granting it a 6% extra capacity under its ultimate loading condition.

3.2 Introduction

Externally bonded fiber reinforced polymer (FRP) is a non-destructive and efficient retrofit technique that has been increasingly common for the strengthening of overloaded bridge cap beams. Despite its large applicability, there is still a lack of analytical methods for the retrofitted cap beams that can accurately predict their structural response due to the added FRP fabrics. Despite some simple equations given by codes [1,2] to obtain an estimate of the added flexural and shear capacity due to the FRP fabrics, several material behaviors that are critical to obtain an accurate response of the retrofitted structure such as bond-slip relationships, confinement effects, and redistribution of stresses are not considered. On top of that, due to their small shear spans, cap beams are usually classified as deep elements that form a direct strut action (i.e., a diagonal compressive stress field between the load application point and the supports) and do not satisfy the Euler-Bernoulli theory (i.e., plane sections remain plane). By neglecting these important structural behaviors when performing retrofit studies using FRP fabrics, the calculated FRP retrofit layout is at risk of being ineffective or even detrimental to the original cap beam. Thus, the complexity and uniqueness of each cap beam require an effective analysis approach with an accurate FRP modeling methodology to substitute any ‘guess-work’ with a better understanding of the structural behavior.

This study proposes an analysis methodology for deep cap beams retrofitted with externally bonded FRP fabrics. The methodology is presented in two stages with respective verifications: constitutive modeling of the critical behavior of materials; and an overall methodology application using a large, in-situ structure. The material behavior models and the modeling procedure proposed are verified using experimental results available in the literature. The overall modeling process is presented to assist in accurately analyzing cap beams using the proposed methodology.

3.3 Research Significance

FRP fabrics have been commonly used to retrofit deep cap beams of in-service bridges that have become structurally deficient due to the increase in loading condition over the decades. There is a lack of holistic analysis approaches to accurately calculate the load capacity of retrofitted cap beams while accounting for the concrete's deep beam actions and the composite behavior introduced by the FRP fabrics. This study details a finite element approach that aims to provide a holistic understanding of the structural behavior and to accurately calculate the load capacity of FRP retrofitted deep cap beams.

3.4 Proposed Cap Beam Numerical Modeling and System-Level Analysis Methodology

A numerical modeling and system-level analysis methodology for deep cap beams retrofitted with externally bonded FRP is proposed using nonlinear finite element analysis (NLFEA). NLFEA models are suitable for the assessment of deep cap beams due to its implementation of the nonlinear effects that are characteristic of deep elements, such as the nonlinearity of the strain distribution and the effects of cracking on the stress distribution [3,4]. Using NLFEA, the performance of the structure under both the serviceability and ultimate limit state conditions can be verified and it allows for the prediction of the progression of nonlinear events (i.e., concrete cracking, reinforcement yielding, concrete crushing, and the formation of the failure mechanism). Using the proposed methodology, if the NLFEA analysis of an un-retrofitted cap beam calculates an overloaded structural state, then a retrofit study using externally bonded FRP fabrics must be conducted to ensure the adequacy of the cap beam to its ultimate loading condition. In such cases, an NLFEA analysis is essential to get an accurate capacity of the deep beam and to determine an FRP retrofit layout that effectively captures the deficiencies of the beam.

3.4.1 Finite Element Material Modeling Approach

The proposed approach was developed using a two-dimensional continuum finite element model. When analyzing reinforced concrete structures, proper modeling of the constitutive response and important second-order material behaviors are crucial [5,6]. Thus, in this study, the model was developed using the computer program VecTor2 [7]. Other specialized programs could also be used for this purpose; however, the selection of VecTor2 was made because it accounts for several second-order material behavior models that are particular to cracked reinforced concrete (see Table 3.1). VecTor2 uses a smeared rotating crack model based on the equilibrium, compatibility, and constitutive models of the Disturbed Stress Field Model [8], which is a refined version of the Modified Compression Field Theory [9] (MCFT), a theory that has been recognized and adopted by the AASHTO [10] and CSA A23.3 [4] codes.

Table 3.1: Material models included in VecTor2.

Material behavior	Default model
Compression base curve	Hognestad parabola [11]
Compression post-peak	Modified Park-Kent [13]
Compression softening	Vecchio 1992-A [15]
Tension stiffening	Modified Bentz 2003 [16]
Tension softening	Linear [7]
Confinement strength	Kupfer/Richart [19,20]
Concrete dilatation	Variable – Orthotropic [19]
Cracking criterion	Mohr-Coulomb (Stress) [12]
Crack width check	Max crack width of Agg/5 [14]
Concrete hysteresis	Nonlinear w/plastic offsets [7]
Slip distortion	Walraven [17]
Rebar hysteresis	Seckin w/Bauschinger [18]
Rebar dowel action	Tassios (Crack slip) [21]
Rebar buckling	Refined Dhakal-Maekawa [22,23]

In the proposed methodology, the concrete is modeled using 8-degree-of-freedom quadrilateral elements (in geometrically uniform regions) or 6-degree-of-freedom triangular elements (in geometrically non-uniform regions such as inclined sections). The concrete material stress-strain response is accounted for using a plastic-offset-based nonlinear model [7]. Several pre- and post-peak models that vary in complexity and applicability are available in the literature; Table 3.1 summarizes the models used in this study with detailed formulation available elsewhere [7]. The concrete model includes nonlinear hysteresis rules for the unloading and reloading conditions [7] (see Figure 3-1a). Even though the proposed methodology includes a static pushover analysis, some parts of the cap beam will unload and some other parts will reload, as the concrete cracking and reinforcement yielding take place, thereby requiring the use of a hysteretic material behavior.

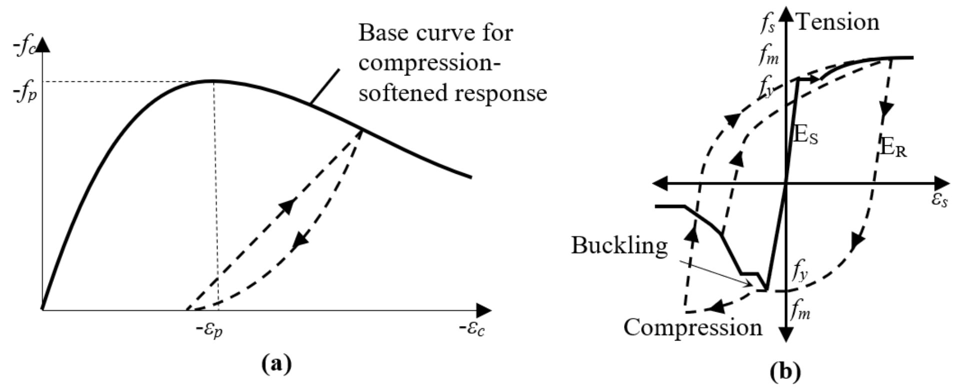

Figure 3-1: (a) Concrete and (b) reinforcing steel material constitutive models.

The shear reinforcement is accounted for through a smeared material model due to their even space across the element. On the other hand, the longitudinal reinforcement is modeled using discrete truss elements (1-degree-of-freedom per node) due to the large amount of steel in specific locations of the structure. The response of the reinforcing bars is modeled using a three-partite constitutive model (see Figure 3-1b), including a parabolic strain hardening region as per the model of Seckin [18].

The FRP fabrics are accounted for in the model through tension-only truss elements aligned vertically, horizontally, or in both directions depending on the fiber orientations of the fabrics. If the fabric has fibers oriented vertically, horizontally, or in both directions, the cross-sectional area of the truss elements is comprised of the effective width of each truss and the thickness of the combined FRP layers. On the other hand, if the fabric has fibers oriented in arbitrary directions, the vertical and horizontal truss-elements' sectional area are comprised of the equivalent horizontal, or vertical, fiber amount. Figures 3-2a and 3-2b show the case of FRP fabric with fibers oriented in an arbitrary direction, which is the most general case. The constitutive model of the fabrics is elastic up to their maximum tensile stress (see Figure 3-2c).

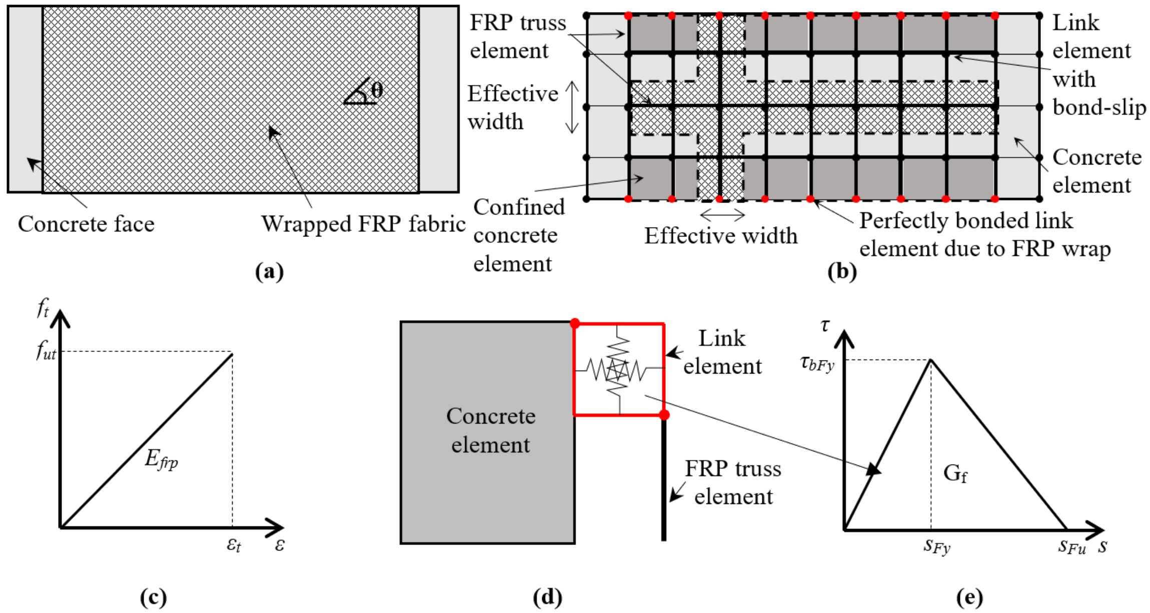

Figure 3-2: (a) FRP fabric wrapped around the concrete element, (b) finite element modeling of FRP fabrics, (c) FRP constitutive model, (d) detail of link element between concrete and FRP fabric, and (e) bond-slip constitutive model.

The modeling of the bond-slip response of the fabrics is crucial for an accurate model because it is a dominant failure mode for structures retrofitted with FRP fabrics [24]. Thus, to account for the bond-slip behavior, link elements (i.e., bi-directional springs) are used to connect the FRP truss elements to the existing concrete elements (see Figure 3-2d). A bi-linear constitutive model based on the fracture energy of concrete (G_f) created for the tangential bond-slip relationship between Carbon FRP (i.e., CFRP) and concrete is attributed to the link elements (see Figure 3-2e), with characteristic points calculated as per Equations 1 to 4 [25,26]. For the FRP fabrics that are completely wrapped around the concrete element, perfect bonding of the fabrics nodes at the edges of the concrete element is considered (see Figure 3-2b). Similarly, wrapped fabrics also confine the longitudinal fabrics and provide an effective anchorage to help avoid de-bonding of the longitudinal fabrics [24,27] Thus, the nodes of the fabrics at the anchorage regions are also perfectly bonded to the concrete. Perfect bond is modeled by specifying a high maximum bond stress for the link elements.

$$\tau_{bFy} = (54f_c')^{0.19} \leq f_r = 0.6(f_c')^{0.5} \quad (1)$$

$$G_f = \left(\tau_{bFy}/6.6\right)^2 \quad (2)$$

$$s_{Fy} = 0.057G_f^{0.5} \quad (3)$$

$$s_{Fu} = 2G_f/\tau_{bFy} \quad (4)$$

where τ_{bFy} is the maximum bond stress in MPa, f'_c is the concrete compressive strength in MPa, f_r is the modulus of rupture of the concrete in MPa, G_f is the fracture energy in N/mm, s_{Fy} is the slip at the maximum bond stress in mm, and s_{Fu} is the slip at the ultimate bond stress (i.e., zero stress) in mm.

When the FRP fabrics are wrapped around the concrete element, they provide confinement to the concrete beam. The confinement is accounted for using a smeared FRP reinforcement component in the out-of-plane direction (referred as z-direction) of the concrete elements at the edges of the beam that are wrapped by the FRP fabrics (see Figure 3-2b), as per Equation 5.

$$f_{c3} = -f_{sz}\rho_z \quad (5)$$

where f_{c3} is the resulting confining pressure, f_{sz} is the stress in the out-of-plane reinforcement, and ρ_z is the out-of-plane reinforcement ratio.

3.4.2 System-Level Capacity Determination

To determine the structural capacity of the cap beam, a pushover analysis, where the finite element model is subjected to a monotonically increasing load up to the structural failure, is performed. Three loading procedures can be used, depending on the objective of the analysis:

The first procedure is used to assess the structural capacity of a non-existing cap beam, the pushover analysis is conducted from no load up to the maximum capacity of the structure, following the Strength I ultimate load combination as per the AASHTO [10] specifications of 1.25 x (Dead Load) + 1.75 x (Live Load). The second procedure is used when assessing the capacity of an existing cap beam, the pushover analysis is first conducted up to the Strength I ultimate load combination. Then, only the factored live load (LL) is continued to increase up to the structural failure. This loading procedure results in a more realistic assessment since the dead load (DL) that acts on the cap beam (i.e., the cap beam's own weight and bridge superstructure) is not expected to increase. The third procedure is used when analyzing the retrofitted structure, the FRP fabrics do not contribute to the original dead load that acts on the beam. Thus, a more realistic procedure is employed: the model is first loaded up to 100% factored dead load and no live load (i.e., 1.25DL + 0LL) with the retrofit elements turned off. From this point on, the retrofit elements are activated, and the dead load is kept constant while the factored live load (i.e., 1.75LL) is progressively increased up to the structural failure.

A global capacity factor method is preferred when calculating the design resistance of a member using NLFEA because nonlinear finite element constitutive models are highly sensitive to the material properties input values, particularly to the concrete strength (f'_c) and the reinforcement yield stress (f_y). Thus, the use of material resistance factors can artificially influence the response of the beam and may even change the failure mode. A full probabilistic analysis that considers the random distribution of the input parameters (i.e., material strengths) is considered the 'ultimate tool' for numerical performance assessments. However, such an approach would require several analyses (between 32 and 64 [28]), which is not feasible for practical applications. In the proposed analysis methodology, the global capacity factor method proposed by Cervenka [28] is used. Cervenka studied different methods to calculate the design resistance of nonlinear analysis models and concluded that the estimate of the coefficient of variation method (ECOV), using only two analyses, yields results that are consistent with the full probabilistic method [28]. In the ECOV method, a global capacity factor (γ_G) is probabilistically obtained based on the coefficient of variation of the resistance (V_R) (see Equation 6), which is estimated based on the resistance of the structure using its characteristic (R_k) and mean (R_m) properties of materials, as defined by Equation 7. The design resistance is obtained from the mean resistance (R_m) and the calculated global capacity factor, as shown in Equation 8.

$$\gamma_G = \exp(\alpha_R \beta V_R) \tag{6}$$

$$V_R = \frac{1}{1.65} \ln\left(\frac{R_m}{R_k}\right) \tag{7}$$

$$R_d = \frac{R_m}{\gamma_G} \tag{8}$$

where α_R is the sensitivity factor for the resistance reliability, β is the reliability index, and R_d is the design resistance of the model. For a structural service life of 50 years, the recommended values of α_R and β are 0.8 and 3.8 [29], respectively, for the ultimate limit state condition. For a service life of 75 years, α_R and β are 0.8 and 3.2, respectively. Similarly, AASHTO [10] recommends a reliability index of 3.5 for bridges. In this study, the reduction factor is calculated considering the service life of 50 years. As such, the global factor can be calculated using Equation 9.

$$\gamma_G = \exp(3.04V_R) \quad (9)$$

The mean material properties of the reinforcing steel and concrete strengths can be calculated using Equations 10 and 11 [30]. Since there is a lack of studies that indicate the mean tensile strength of FRP fabrics, this study used 25 technical sheets of different FRP fabrics manufacturer (15 of CFRP and 10 of GFRP) to obtain this factor for FRP fabrics. The factor for CFRP fabrics was calculated to be 1.18, which was slightly lower than the 1.20 factor for GFRP fabrics (see Equation 12). The mean bonding properties are inherently accounted for by the consideration of the mean concrete properties (see Equations 1-4).

$$f_{ym} = 1.1f_{yk} \quad (10$$

$$f_{cm} = 1.1\left(\frac{\gamma_s}{\gamma_c}\right)f_{ck} \quad (11)$$

$$f_{tm} = 1.18{\sim}1.20f_{tk} \quad (12)$$

where f_{yk} and f_{ck} are the characteristic material properties for the reinforcing steel and concrete, respectively; γ_s and γ_c are the partial factors for materials for the ultimate limit states; and f_{tk} is the characteristic tensile strength of the FRP.

3.5 Verification of the Proposed Modeling Approach

The accuracy of the proposed material modeling approach was verified using two simply-supported beams experimentally retrofitted with CFRP fabrics: one with continuum CFRP U-wrap fabrics for shear strengthening [31] (see Figure 3-3a); and another with longitudinal CFRP fabrics for flexural strengthening anchored by U-wrapped fabrics [32] (see Figure 3-4a). The first specimen (originally referred to as SO3-4) was used to verify the bond-slip constitutive models (i.e., Equations 1-4) and the confinement effect of the fabrics (i.e., Equation 5). The second specimen (originally referenced as B70PW) was used to verify the bonding of the flexural FRP fabrics due to the provided anchorage fabrics.

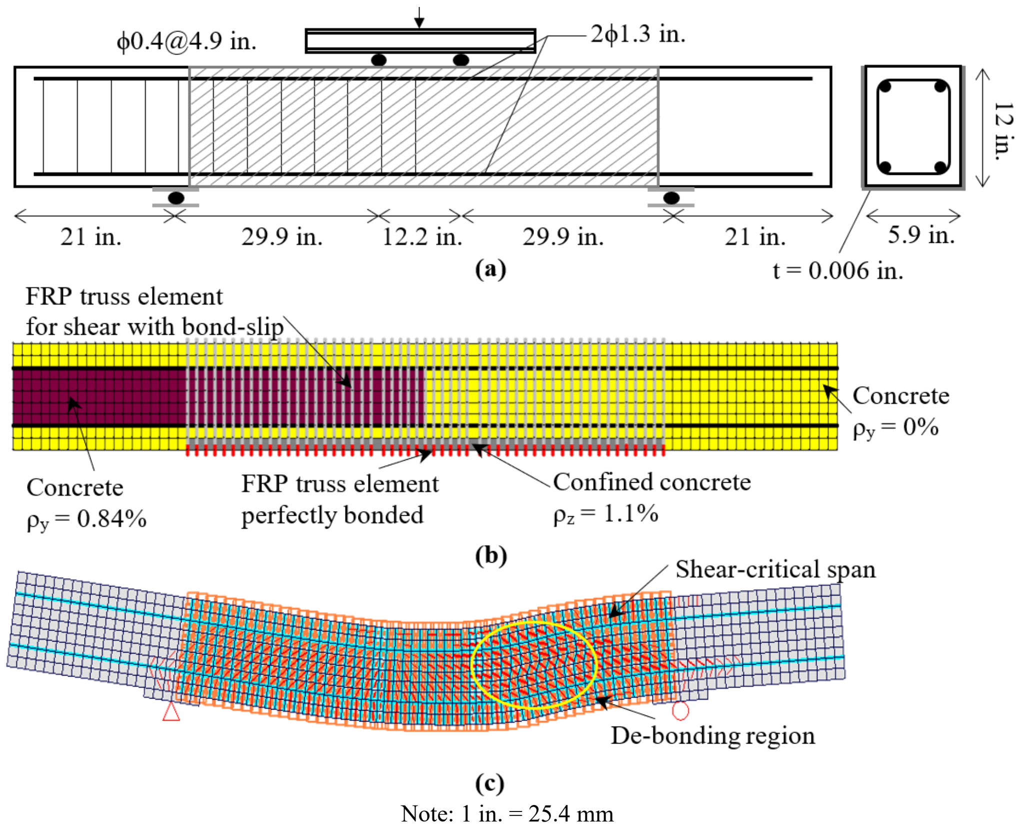

Figure 3-3: (a) SO3-4 experimental setup, (b) finite element model, and (c) deflected shape at failure condition.

The details of the experimental setup of each reinforced concrete beam are discussed elsewhere [31,32]. In short, the material properties experimentally reported and used in the NLFEA discussed herein were, for the SO3-4 beam [31]: concrete strength of 4 ksi (27.5 MPa), reinforcing steel modulus of elasticity, yield stress, and ultimate stress of 29000 ksi (200 GPa), 67 ksi (460 MPa), and 106 ksi (730 MPa), respectively, and CFRP modulus of elasticity and tensile strength of 33000 ksi (228 GPa) and 550 ksi (3790 MPa), respectively; and for the B70PW beam [32]: average concrete strength of 8 ksi (54 MPa), steel reinforcement modulus of elasticity and yielding strength of 29300 ksi (202 GPa) and 89 ksi (611 MPa), respectively, and CFRP modulus of elasticity and tensile strength of 31200 ksi (215 GPa) and 363 ksi (2500 MPa). Figures 3-3 and 3-4 presents the experimental setup, the created finite element model, and the beam deformations at failure for each specimen. Because U-wrap CFRP fabrics were used, only the nodes at the bottom edge of the beams were modeled as perfectly bonded. Similarly, the out-of-plane confinement reinforcement was modeled only for the concrete elements wrapped in the fabrics at the bottom edge of the beams (see Figures 3-3 and 3-4).

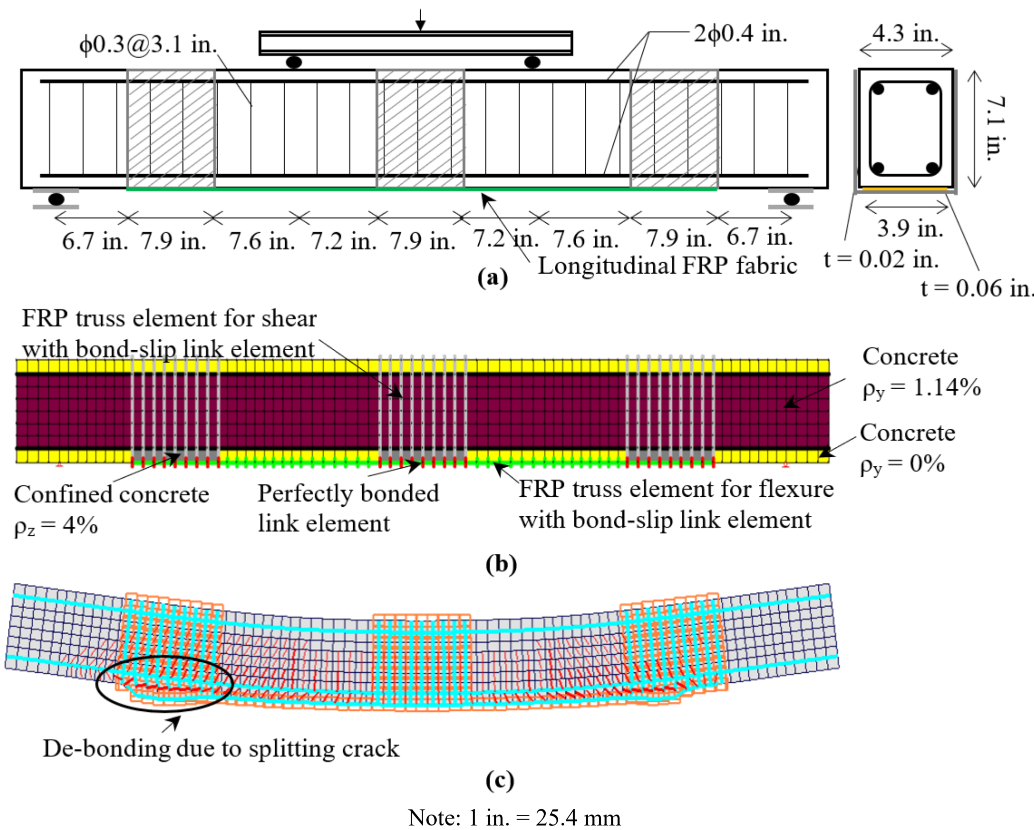

Figure 3-4: (a) B70PW experimental setup, (b) finite element model, and (c) deflected shape at failure condition.

Figure 3-5 shows the load-deflection response experimentally obtained and numerically calculated by the created finite element model. The peak load, peak displacement and overall stiffness response of both beams were well captured by the finite element model. The calculated-to-experimental ratios (i.e., $1\text{-}P_{cal}/P_{exp}$) of the peak load capacity were -2.5% and 5.9% for the SO3-4 and the B70PW specimens, respectively. For the peak displacement, the calculated-to-experimental rations were 32.9% and 2.9% for the SO3-4 and the B70PW specimens, respectively. It is believed that the difference in peak displacement in the SO3-4 beam, despite its good overall response, was due to differences in the experimentally reported and actual material properties, which resulted in a slight stiffness deviation. The failure mode of the SO3-4 beam was experimentally reported to be the de-bonding of the CFRP U-wrap fabrics at a load of 65 kips (289 kN) [31]. The finite element model successfully calculated the failure mode as de-bonding of the CFRP fabrics starting at a load of 64 kips (285 kN) at the shear-critical span (see Figure 3-3c). The criteria used to identify de-bonding on the beams were based on the relative displacements between the CFRP fabrics and the concrete exceeding the slip at the maximum bond stress, after which bonding stresses decrease (i.e., as shown in Figure 3-2e). For the B70PW beam, the experimentally reported failure mode was a shear-tension failure with the initial flexural-shear cracks followed by the de-bonding of the flexural CFRP fabrics due to splitting cracks in the concrete [32]. The calculated failure mode of the beam captured the experimental response successfully as shown in Figure 3-4c, with splitting cracks at the bottom part of the beam that caused the de-bonding of the flexural CFRP reinforcement.

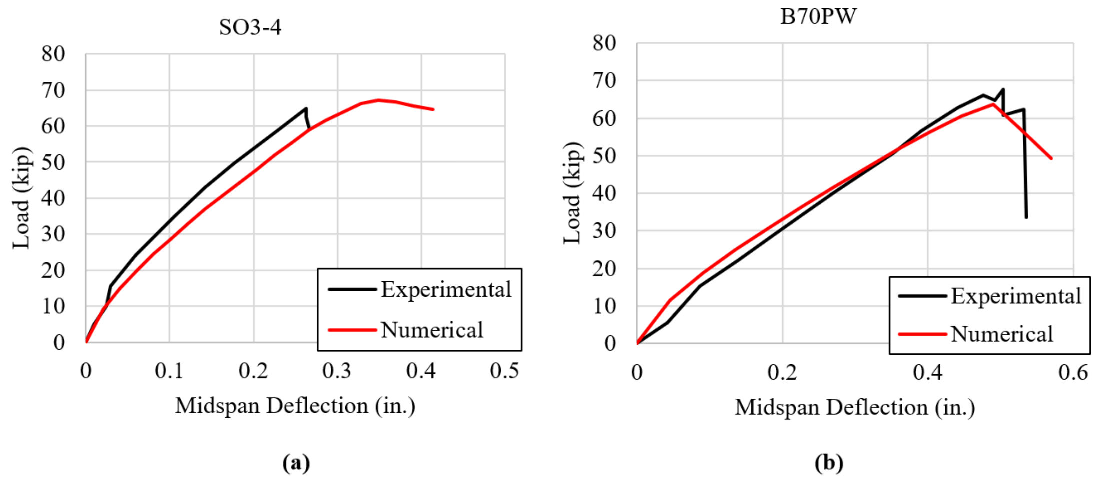

NOTE: 1 in. = 25.4 mm; 1 kip = 4.45 kN.

Figure 3-5: (a) Cantilever and (b) inner span total load versus displacement response.

3.6 System-Level Verification of The NLFEA Approach

The proposed NLFEA approach was verified using a cap beam of an existing overpass structure (see Figure 3-6). Cross-sectional and a strut-and-tie model (STM) analyses calculated the cap beam to be overloaded. Thus, an NLFEA following the proposed modeling methodology was employed to calculate an accurate loading capacity of the cap beam.

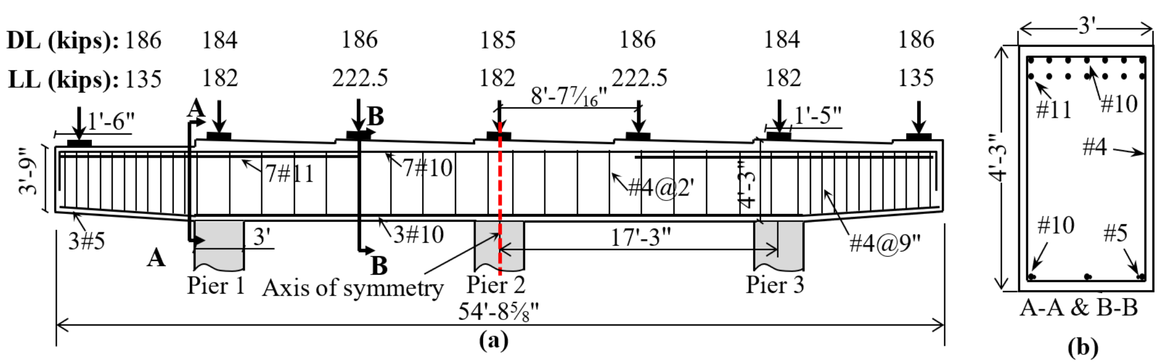

NOTE: 1 in. = 25.4 mm; 1 ft. = 0.305 m; 1 kip = 4.45 kN

Figure 3-6: Cap beam examined: (a) elevation and (b) cross-section.

The finite element model was developed in VecTor2, as shown in Figure 3-7, with the cross-sectional dimensions, reinforcement layout, beam configuration, and unfactored loading condition shown in Figure 3-6. The concrete compressive strength and steel reinforcement yield stress were reported on the original design drawings as 4 ksi (27.6 MPa) and 40 ksi (275 MPa), respectively. The geometric symmetry of the beam allowed for a half-model of the cap beam, which significantly reduced the numerical model size and lowered the modeling efforts. The support conditions applied included rollers on the axis of symmetry and pins at the lowermost ends of the pier columns (not shown in Figure 3-7).

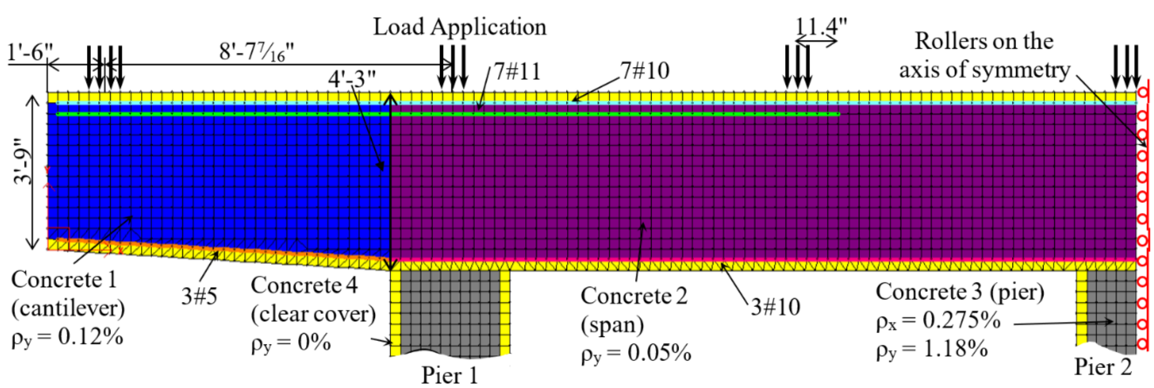

NOTE: 1 in. = 25.4 mm; 1 ft. = 0.305 m; 1 kip = 4.45 kN

Figure 3-7: Finite element model developed for the NLFEA.

Three of the considered second-order models (see Table 3.1) were found to be particularly important for the cap beam examined: the concrete compression softening (i.e., the reduction in the uniaxial compressive strength and stiffness due to transverse tensile cracking), the concrete tension stiffening (i.e., the ability of cracked reinforced concrete to transmit tensile stresses across cracks), and the dowel action (i.e., the additional shear strength provided by the main reinforcing bars). The very low amounts of stirrup reinforcement present in the cap beam make it prone to shear cracking, which reduces the effectiveness of the concrete struts and, thus, requires the consideration of the ‘concrete compression softening’. The cap beam is also prone to flexural cracking due to the lack of well-distributed layers of reinforcement, and thus its response is sensitive to the amount of tension transmitted across cracks, requiring the modeling of the ‘concrete tension stiffening’ effects. Finally, the low amount of stirrups reduce the shear capacity of the beam, such that the additional shear resistance due to the ‘dowel action’ becomes important.

The pushover loading procedure was performed for the assessment of existing cap beams (i.e., as the second proposed pushover loading method, see the “System-Level Capacity Determination” section). To obtain the design resistance of the cap beam, two analyses were performed: one with characteristic and one with mean properties of materials (as discussed in the “System-Level Capacity Determination” section). The mean values of the reinforcing steel and concrete strengths were calculated, using Equations 10 and 11, to be 44 ksi (275 MPa) and 3.32 ksi (22.9 MPa). For brevity, only the analysis results using the characteristic material properties are shown in this paper.

The characteristic pushover analysis calculated a maximum load capacity of 3447 kips (15333.2 kN), which represented approximately 90% of the ultimate load combination. At the failure condition (see Figure 3-8), an extensive shear and flexural cracking pattern were calculated at the cantilever span, which indicated the formation of the deep beam strut-action through shear cracks spanning from the point loads to the pier supports. The yielding of both top and bottom flexural reinforcement of the cap beam at the cantilever span caused the crushing of the concrete (i.e., high compressive strains) at the beam-column interface, contributing significantly to the propagation of the cracks (i.e., vertical cracks), resulting in a flexure-shear failure of the cap beam.

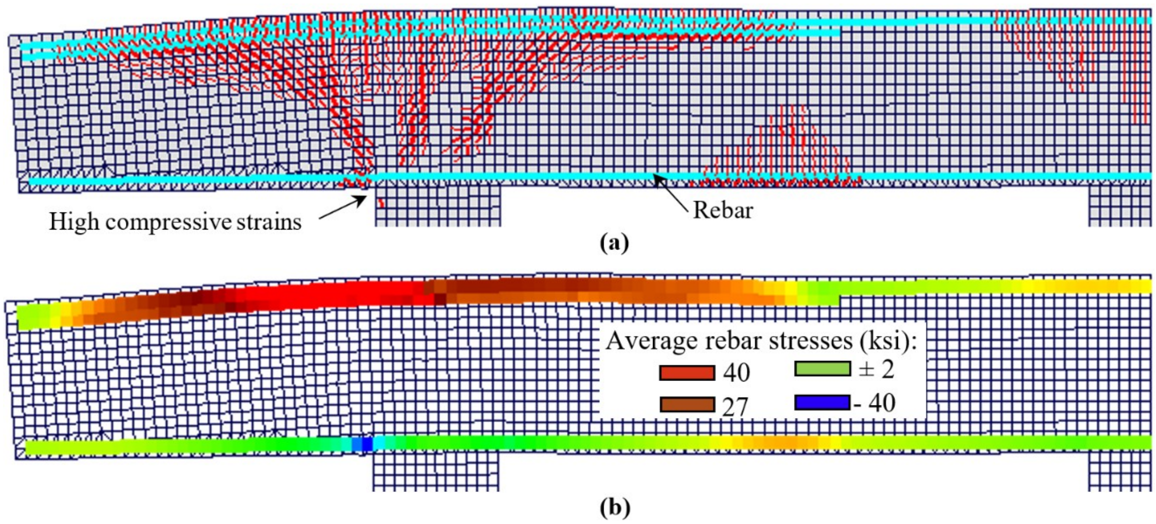

NOTE: 1 ksi = 6.9 MPa

Figure 3-8: Pushover analysis (a) crack pattern and (b) rebar stresses at failure loading condition (10 times actual deflection).

To obtain the system-level load capacity, the two performed pushover analyses were combined using Equations 7 and 9. The applied force versus displacement of the cantilever and inner span of the beams, for both analyses, are shown in Figure 3-9. The global capacity factor was calculated to be 1.10 and the design capacity of the cap beam was calculated, as per Equation 8, to be 3178 kips (14135 kN). Consequently, the un-retrofitted cap beam was found to be 17% overloaded. Thus, a retrofit study of the cap beam shall be performed to guarantee that the load resistance of the retrofitted cap beam surpasses its ultimate load demand.

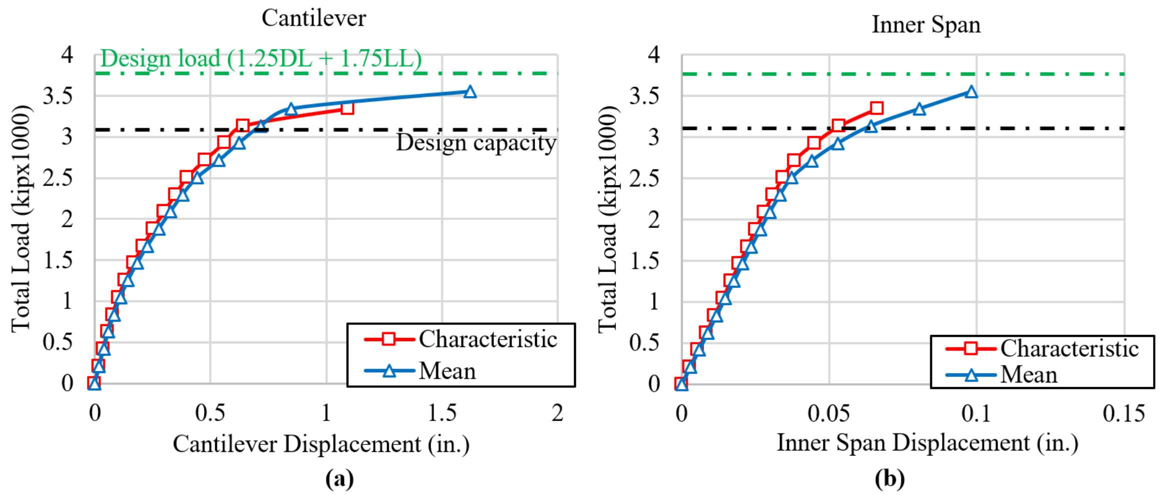

NOTE: 1 in. = 25.4 mm; 1 kip = 4.45 kN

Figure 3-9: (a) Cantilever and (b) inner span total load versus displacement response.

3.6.1 Retrofit of the cap beam using externally bonded FRP

A suitable FRP retrofit layout needs to be developed based on the failure mechanisms developed on the un-retrofitted structure. When studying an effective FRP retrofit layout, it is important to ensure that the new cap beam is capable not only to resist its un-retrofitted failure mechanisms but also to be able to resist new failure modes that can occur due to the redistribution of stresses caused by the added FRP fabrics. The critical failure modes for externally bonded FRP retrofitted structures are: concrete shear, concrete flexure, concrete compression (i.e., crushing), fabric de-bonding, and fabric rupture. A general FRP retrofit layout that covers the critical failure modes is proposed. As shown in Figure 3-10, this layout includes fabrics to increase shear capacity that are completely wrapped (i.e., black fabrics on Figure 3-10) and U-wrapped (i.e., gray fabrics on Figure 3-10) around the concrete beam, and longitudinal fabrics that are bonded to the top and bottom of the beam to increase the flexural capacity (i.e., blue and green fabrics, respectively, on Figure 3-10). The completely wrapped FRP fabrics also provide effective anchorage to the longitudinal fabrics and confinement effects to the edges of the concrete beam. Consequently, besides its effective flexural and shear retrofit, this layout also improves the compressive capacity of the concrete (i.e., increasing its crushing resistance) and the bond-slip mechanism of the fabrics.

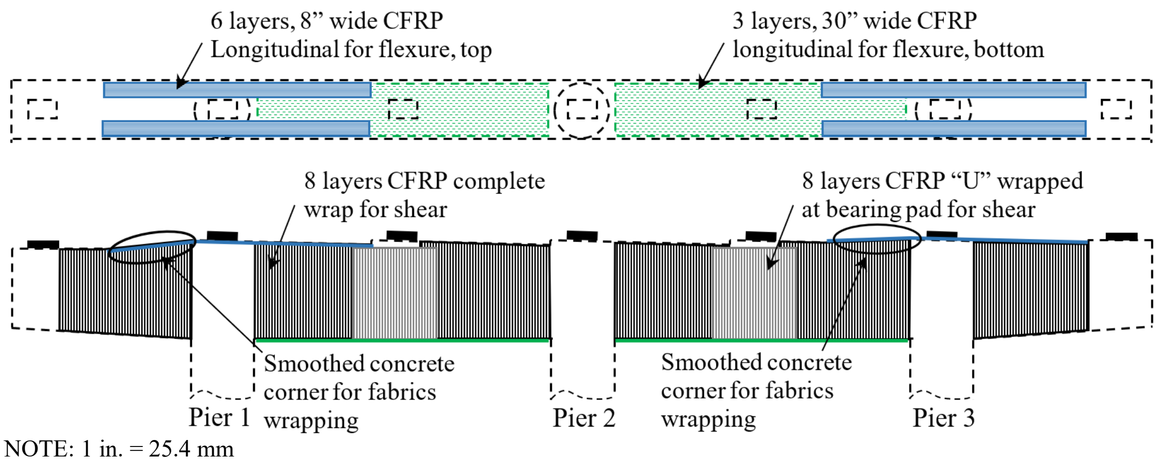

Figure 3-10: FRP retrofit layout.

To determine the amount of FRP fabrics necessary to strengthen the beam (i.e., thickness and width of each fabric section of the FRP retrofit layout), different numerical models can be created (i.e., each one with a proposed amount of FRP fabrics) until the NLFEA calculates a safe structural condition under the ultimate loading condition. This process allows to effectively visualize the contribution and importance of each section of the FRP retrofit layout to the deficient structure. For conciseness, the fabric amounts for the final retrofit layout implemented on the studied cap beam is presented in Figure 3-10. The top longitudinal FRP fabrics were separated in two sections due to the locations of the bearing plates and some corners of the concrete beam were smoothed to help the fabrics application (see Figure 3-10). Similarly, the completely wrapped FRP fabrics were substituted by U-wrapped due to the presence of the bearing plates.

Once the externally bonded FRP layout was determined, it was implemented in the NLFEA model of the un-retrofitted structure (see Figure 3-11). The proposed FRP finite element material modeling approach was essential to ensure an accurate structural response and assessment of the additional capacity of the cap beam. In addition, the material modeling approach also modeled the critical failure modes (as discussed above): the concrete flexural and shear failure modes are covered by the employed concrete constitutive models; the compressive failure mode is covered by the concrete and FRP confinement effect models; the de-bonding is covered by the presented bond-slip relationship and the discussed perfect bonded regions; and the fabrics rupture is covered by the employed linear-elastic FRP material model. Thus, the determined effective FRP retrofit layout could be accurately incorporated in the NLFEA modeling approach, which makes it a suitable analysis procedure for accurate responses calculation.

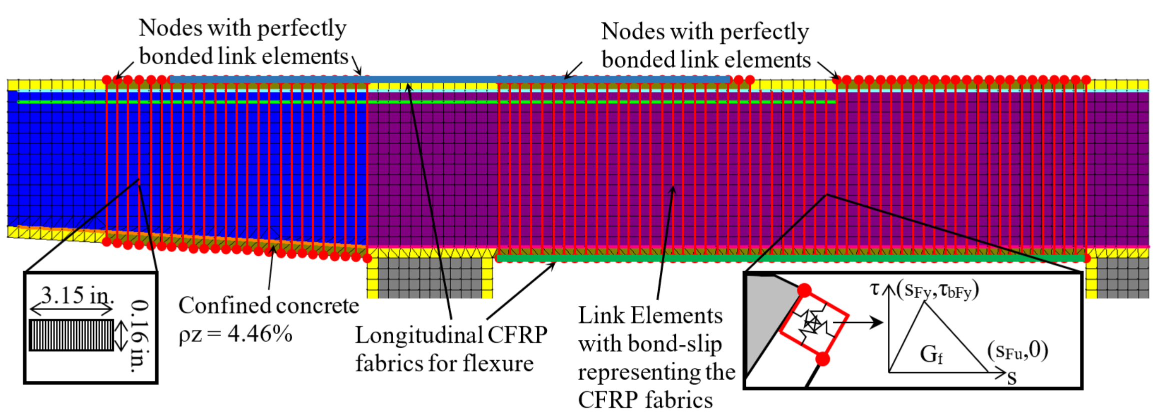

Figure 3-11: Retrofitted finite element model.

The CFRP fabrics used had a modulus of elasticity, tensile strength, and thickness of 8200 ksi (56.5 GPa), 105 ksi (724 MPa), and 0.02 in. (0.51 mm), respectively. Using Equations 1-4, the calculated bond-slip properties of maximum bond stress, the slip at the maximum bond stress, and the slip at the ultimate bond stress were, 0.4 ksi (2.87 MPa),

9.83×10^{-4} in. (0.025 mm), and 5.20×10^{-3} in. (0.132 mm), respectively. Figure 3-11 shows the numerical model of the cap beam with the applied CFRP fabrics. Following the proposed FRP modeling approach, the CFRP fabrics were modeled with truss elements using the effective area of each truss and the bond-slip relationship. The wrapped fabrics (i.e., red truss elements in Figure 3-11) were perfectly bonded on the top and bottom edge of the concrete beam due to their complete wrapping (except over the bearing plate at the inner span). The bottom flexural fabrics were modeled as perfectly bonded due to the anchorage provided by the wrapped CFRP fabrics, and the top flexural fabrics were perfectly bonded at the anchorage regions. Out-of-plane confinement reinforcement was added to the concrete elements at the edges where the fabrics are wrapped.

For the system-level load capacity determination, the pushover loading procedure was performed following the method for the assessment of retrofitted structures (i.e., the third proposed pushover loading method, see the "System-Level Capacity Determination" section). The characteristic pushover analysis of the retrofitted structure showed an improvement in structural performance when compared to the same loading condition that caused the failure of the un-retrofitted cap beam (see Figure 3-12). Besides reducing the shear and flexural cracking condition at the cantilever and the inner span of the cap beam, the FRP retrofit layout also lowered the bottom reinforcement stress state and, in consequence, the concrete compressive strains at the cantilever-column interface.

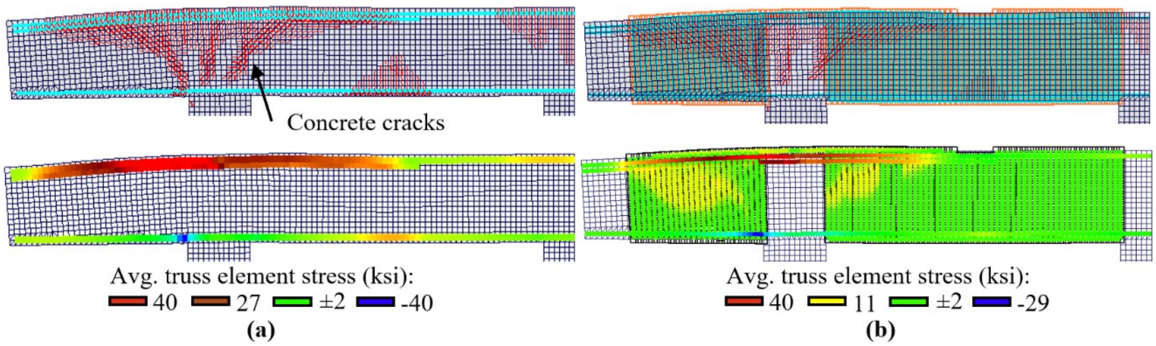

NOTE: 1 ksi = 6.9 MPa

Figure 3-12: (a) Un-retrofitted model at failure condition and (b) retrofitted model at same loading condition.

The characteristic pushover analysis of the retrofitted cap beam calculated a maximum capacity of 4050 kips (18018 kN). At the structural failure condition (exaggerated in Figure 3-13), extensive shear and flexural cracking patterns were observed. The high shear stresses on the cantilever span caused the FRP fabrics to de-bond following the main shear crack pattern (see Figure 3-13). The top and bottom reinforcing steel yielded and high compressive strains (i.e., concrete crushing) developed at the cantilever-column interface. The flexural capacity of the cantilever section relied mainly on the top longitudinal FRP fabrics, which, due to the high-stress demand, de-bonded through the split cracking of the adherent concrete, causing a flexure-shear failure of the cap beam.

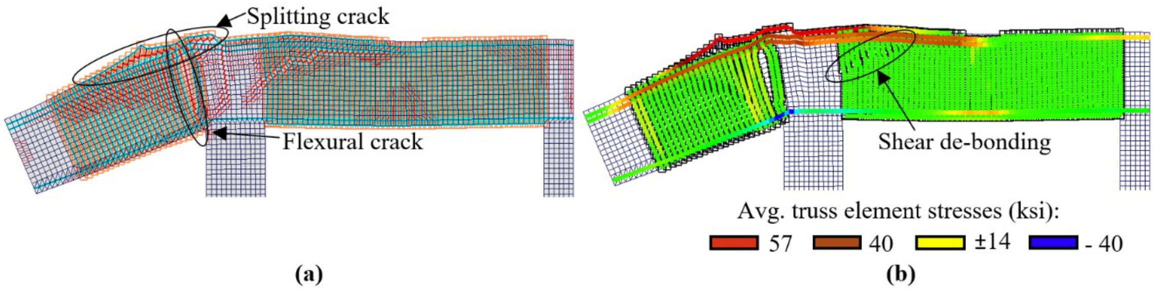

NOTE: 1 ksi = 6.9 MPa

Figure 3-13: (a) Retrofitted cap beam response and (b) rebar stresses at failure loading condition (20 times actual deflection).

Using Equations 7 and 9 with the results of the two analyses performed with the retrofitted finite element model (i.e., one with characteristic properties of material and one with mean properties of material), the calculated global capacity factor was 1.00 (both analyses calculated the same resistance) and the system-level load capacity of the retrofitted cap beam was determined to be 4050 kips (18018 kN). Figure 3-14 compares the characteristic pushover analysis responses of the un-retrofitted and retrofitted structure. In Figure 3-14, the last data point of each curve (i.e., the failure load and displacement) was selected for the loading condition at which the failure mechanisms that developed in each beam (and were described above) occurred. After this loading condition, the subsequent load stages of the numerical model were no longer representative of the real structural behavior (excessive displacements, zero-stresses, etc.) since failure mechanisms had already developed. The curves in Figure 3-14 do not present a strength peak (and subsequent loss of strength) due to the force-based nature of the numerical analysis performed. The calculated load capacity represented an increase of 27% in strength, when compared to the un-retrofitted cap beam (3178 kips or 14135 kN) and indicated an extra capacity of 6% over the ultimate loading condition. These results corroborate the benefits of the determined CFRP retrofit layout and the effectiveness of the modeling approach. As a result, the proposed methodology was successful in providing an effective FRP retrofit to the overloaded cap beam.

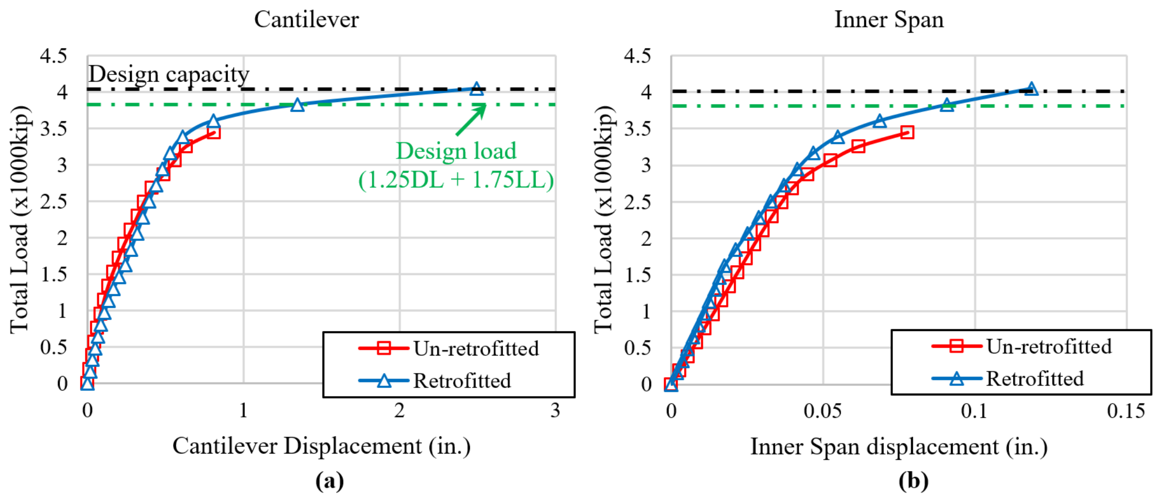

Figure 3-14: (a) Cantilever and (b) inner span total load versus displacement response of the retrofitted model.

3.7 Summary and Conclusions

Deep bridge cap beams retrofitted with fiber reinforced polymers require special analysis methods in order to effectively account for behaviors that are characteristic of deep elements (such as the nonlinearity of the strain distribution and the effects of cracking on the stress distribution) and retrofit-related mechanisms (such as bond-slip relationships, confinement effects, and redistribution of stresses are not considered). Despite some equations given by available retrofit codes to calculate the extra capacity that FRP fabrics might produce on a general concrete element, no provisions account for the aforementioned behaviors that directly affect deep cap beams retrofitted with FRP fabrics. This study proposed an analysis methodology for deep cap beams retrofitted with externally bonded FRP fabrics. Details were given regarding the constitutive modeling of the critical behavior of materials, which were verified using experimental results available in the literature. Finally, to exemplify the application of the proposed methodology, a real/large structure was analyzed, and an effective retrofit solution was calculated based on the calculated beam response. The results of this study support the following conclusions:

- The proposed analysis methodology presented a comprehensive set of material behaviors and numerical modeling formulations that are essential for the analysis of deep cap beam elements. Three different loading approaches were defined to obtain a more accurate response of cap beams depending on the state of the bridge, i.e., non-existing bridge, existing bridge, retrofitted bridge. Finally, the proposed methodology presented a global capacity factor procedure based on probabilistic fundamentals for the determination of the design resistance of a cap beam.
- The proposed methodology and its constitutive modeling approaches were successfully verified using two different experimental studies from the literature. The overall load-displacement deviation between the experimental results and the created methodology was calculated to be within 6%. In addition, the verification studies successfully verified the proposed FRP-concrete composite structural behavior, including the bond-slip constitutive model, concrete confinement effects caused by the fabric wrap, and the perfectly bonded conditions of longitudinal fabrics anchored by U-wrapped fabrics. As a result, the numerical model created using the proposed methodology was able to capture the experimentally observed failure modes.
- An existing deep cap beam structure was analyzed to illustrate the benefits and in-depth information provided by the proposed methodology. The analyzed cap beam

was calculated to be 17% overloaded considering the design ultimate load condition. The calculated response of the cap beam confirmed the deep beam action occurring on the beam through the calculated crack pattern, which also helped identify the most critical spans of the beam, the type of failure (i.e., flexure, shear, or flexure-shear), and critical effects that should be considered in the retrofit design.

- The detailed damage pattern and failure mechanism calculated by the numerical model of the un-retrofitted cap beam were essential in the determination of an efficient distribution of the FRP fabric throughout the analyzed cap beam to capture the critical failure mechanisms. Such a design approach differs significantly from the use of code provisions, in which simplified equations are given to obtain the added capacity of the member due to the usage of FRP fabrics retrofit while neglecting important behaviors such as the deep beam effects, confinement effects, and bond-slip interaction.
- The information obtained from the un-retrofitted numerical model was used to determine a CFRP retrofit layout on the overloaded cap beam. The proposed methodology was again used to create a retrofitted numerical model of the analyzed cap beam, which enabled an increase in the load carrying capacity of the cap beam by 27%, allowed it to be safe under its ultimate loading condition, and developed an additional 6% extra capacity.
- The general FRP retrofit layout configuration used in the studied cap beam (i.e., position and distribution of fabrics, but not their quantities) could be applied for a general cap beam as long as its failure conditions follow the trend observed in the structure analyzed in this paper. The number of fabric's layers and material

properties on each section of the FRP retrofit layout can be studied to result in the desired structural performance.

3.8 Acknowledgments

The authors would like to thank the Ohio Department of Transportation for providing the structural design drawings and the contributions of Dr. Douglas K. Nims and Mr. John R. Morganstern for extracting the main structural details and participating in several meetings to discuss the various aspects of the bridge.

Chapter 4

Journal Paper III - Characterization of the Out-of-Plane Behavior of CLT Panel Connections[3]

4.1 Abstract

The increasing damage caused by earthquakes and tsunamis has stimulated the research for new construction systems that can perform well during both seismic and subsequent tsunami events. Cross Laminated Timber (CLT) is a relatively new and robust construction material that has been extensively investigated under seismic load conditions, during which it exhibited good performance. However, its potential as a tsunami-resilient alternative has not yet been explored. The first step to assess the performance of CLT buildings to tsunami loads is to understand and characterize their out-of-plane behavior because, unlike seismic loads, tsunami loads primarily engage the out-of-plane CLT panels. However, there is a major lack of knowledge on the behavior of CLT panel connections subjected to out-of-plane load conditions. This creates a significant barrier in the adoption of CLT structures for tsunami-resilient wood buildings and communities. The objective of this study is to advance the current understanding and characterize the behavior

[3] Manuscript submitted to and under review in Engineering Structures, Rafael A. Salgado & Serhan Guner, Characterization of the Out-of-Plane Behavior of CLT Panel Connections, © 2020, with permission from Elsevier. For the published version, please refer to https://www.utoledo.edu/engineering/faculty/serhan-guner/publications.html.

of CLT panel connections under tsunami-induced out-of-plane load conditions. A secondary objective is to identify key connection design parameters and quantify their influences on the out-of-plane behavior. To achieve these objectives, high-fidelity nonlinear numerical models of CLT panel connections are developed, experimentally validated, and investigated under two tsunami-induced out-of-plane load conditions. A numerical investigation with 48 numerical models is performed and the analysis of variance (ANOVA) method is used to quantify the influences of three key connection design parameters on the out-of-plane behavior of CLT panel connections. The results indicated that the crushing of the wall panel's wood fibers dictated the behavior in one of the out-of-plane directions considered while the axial withdrawal of the nails on the wall side of the connections dictated the behavior in the other direction. A simplified equation and a mechanics-based procedure were developed for estimating the load capacity and quantifying the nail contribution to the capacity of the connections under the out-of-plane load conditions considered.

4.2 Introduction

Every year, sixteen major earthquakes are expected to occur around the world [1]. Although no data indicates that this number has been rising in recent years, the damage caused by these events has been rapidly increasing due to the urbanization of vulnerable areas. As a result, the ten most costly earthquakes of all time have occurred in the past 30 years – three of them in the past decade – and have inflicted more than $260bn in damage [2]. This increasing damage has fostered research for new infrastructure systems to create more resilient communities. Cross Laminated Timber (CLT) is a relatively new and robust construction material comprised of strong panels formed from wooden boards placed crosswise. The seismic performance of CLT buildings has been extensively investigated over the past decades, where it has been shown to perform very well subjected to earthquake excitations [3–12].

Earthquakes are the most common source of tsunamis. Major tsunamis occur about once per decade [13] and, similar to earthquakes, the damage caused by these events has been greatly amplified by vulnerable coastal areas becoming more densely populated. The 2004 Indian Ocean and 2011 Japan events, for example, resulted in approximately 250,000 fatalities, dislocation of more than 350,000 people, and astronomical costs of more than $350 bn. [14–16]. These two events alone have surpassed the aggregated damage cost of the ten most costly earthquakes of all time. Consequently, to increase the resilience of coastal communities, new infrastructure systems must perform well during both seismic and subsequent tsunami events. Although CLT buildings have shown good performance under seismic events, the potential of this new material as a tsunami-resilient structural system has not yet been explored.

Unlike seismic loads that primarily engage the in-plane behavior of CLT panels, a tsunami wave impact creates a load pattern that predominantly engages the out-of-plane behavior of CLT panels (see Figure 4-1). A few available studies have examined the out-of-plane behavior of isolated CLT panels [17–20] while neglecting the behavior of the panel connections. To this date, there are no studies in the literature that have attempted to characterize the out-of-plane behavior of CLT panel connections. However, this characterization is critical (and considered the first steps) for the performance assessment of CLT buildings to tsunami loads because CLT panel connections are known to dictate the performance of CLT structures, supplying most of the flexibility and providing the necessary strength, stiffness, and ductility [3,21–26]. Consequently, they are expected to dictate the out-of-plane performance of CLT buildings under tsunami loads.

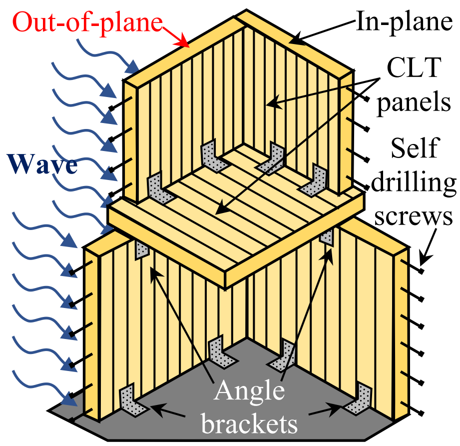

Figure 4-1: Different CLT building elements.

CLT panel connections are used to join the CLT wall panels to another CLT floor panel or to the foundation, as shown in Figure 4-1. These wall-to-floor and wall-to-foundation panel connections are commonly comprised of metal connectors (such as angle brackets), steel fasteners (such as nails or bolts), and the local section of the connected CLT panels or the foundation. Consequently, their behavior is usually governed by certain key connection design parameters, such as the number of fasteners on the wall and floor sides of the connection, and the wood species used in the CLT panel. There is a major lack of knowledge on the behavior of wall-to-floor and wall-to-foundation CLT panel connections subjected to tsunami-induced out-of-plane load conditions. In addition, it is not known what key connection design parameters are significant and how they influence the global out-of-plane response of the connections. This knowledge gap creates a significant barrier for the adoption of the CLT material for the creation of tsunami-resilient buildings and communities.

The main objective of this study is to take the first steps to advance the current understanding and characterize the behavior of wall-to-floor and wall-to-foundation CLT panel connections under out-of-plane load conditions. Another objective is to identify the key connection design parameters and quantify their influences on the out-of-plane behavior, including the load and displacement capacities.

4.3 Methodology

To achieve the research objectives, experimentally validated high-fidelity nonlinear numerical models of wall-to-floor and wall-to-foundation panel connections were developed and subjected to two out-of-plane load conditions. For brevity, panel connections will simply be referred from now on as connections. The angle brackets, fasteners, and CLT panel layup (i.e., number of layers used and their thickness) selected for use in this study are shown in Figure 4-2. This selection was made because they are commonly used in today's CLT buildings and their in-plane behaviors are characterized in other studies [6,27–35], the results of which were used in this study for experimental validation purposes. The validated models were used to advance the current understanding and characterize the tsunami-induced out-of-plane behavior of the connections. A numerical investigation with 48 models was performed and the results were assessed using the analysis of variance (ANOVA) method [36] to statistically identify and quantify the influence of each parameter on the out-of-plane behavior of the connections. Using the results, a simplified equation and a mechanics-based procedure were developed for estimating the load capacity and quantifying the nail contribution to the capacity of the connections under the out-of-plane load conditions considered.

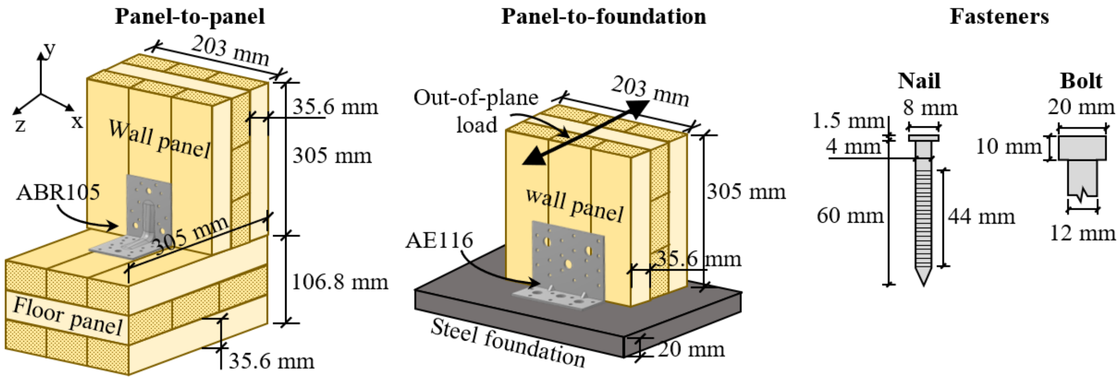

Figure 4-2: Connections analyzed.

4.4 High-Fidelity Nonlinear Numerical Modeling

The objective of the high-fidelity numerical model is to enable the accurate simulation of the nonlinear response that involves the contact, plasticity, and large deformations of the components of the connection shown in Figure 4-2. 8-node 24 degrees-of-freedom 3D continuum brick elements were used in combination with suitable nonlinear material models (to be discussed below) in the Abaqus program [37]. To ensure an accurate simulation, the employed modeling approach deviated from commonly adopted simplified techniques to model CLT structures, such as the use of zero-length link elements to model the connections (e.g., [29]), springs to simulate the fastening components (e.g., [38]), and layered shell elements to simulate the CLT panels (e.g., [34]).

The wood panels were modeled using two distinct formulations. The first formulation employs an orthotropic uniaxial stress-strain wood response idealized as a linear-elastic region followed by a post-elastic brittle (i.e., for tension failure modes) or ductile behavior (i.e., for compressive failure modes) as shown in Figure 4-3c. This formulation was used to model the wood regions at 4.5d (i.e., nail diameter) or greater distances from the nails, termed herein regular wood region (see Figure 4-3a and Figure 4-3c). The second formulation employs the Hong and Barret [39] wood foundation approach (see Figure 4-3a and Figure 4-3b). This formulation was used to model the wood regions in the vicinity of the nails (i.e., closer than 4.5d from the nails) because it accounts for the softening of the wood's mechanical properties due to the damage caused by the installation of the nails [40].

An isotropic hardening plastic material model was employed to simulate the nonlinear behavior of the fasteners and angle brackets, which are typically manufactured from stainless-steel or high-carbon alloy steel. The response of these elements was numerically idealized with a bilinear stress-strain model as shown in Figure 4-3d. The combination of the employed wood and steel modeling approaches numerically accounts for the bending failure modes of the European Yield Model [41] of dowel-type fastening components embedded in wood, adopted by Eurocode 5 [42] and the National Design Specification for Wood Construction [43]. The axial withdrawal behavior of the nails embedded in the wood was modeled following a bilinear axial force-displacement curve dictated by the initial axial withdrawal stiffness (K_{ax}) and the axial withdrawal capacity (F_{ax}) as shown in Figure 4-3e. The models of Eurocode 5 [42], shown in Eq. 1, and Uibel and Blaß [44], in Eq. 2, have been shown to provide a good estimate of K_{ax} and F_{ax} [23,45]. The nails are typically fastened using torque-controlled tools, which prestresses the nails under service load conditions. Consequently, in the numerical models, an axial compressive pressure load was applied on the nail heads using a recommended installation torque based on the diameter of the nails [46].

$$K_{ax}=\frac{4}{90}\rho^{1.5}d^{0.8} \tag{1}$$

$$F_{ax}=0.35d^{0.8}l_{ef}^{0.9}\rho^{0.75} \tag{2}$$

where ρ is the density of the wood (kg/m^3); d is the diameter of the fastening component's shank (mm); and lef is the threaded length of the fastening component (mm).

The developed numerical models of the wall-to-floor and wall-to-foundation connections are shown in Figure 4-3a and Figure 4-3b, respectively. A surface-to-surface discretization method was used to define the mechanical interface interaction between the CLT panels, fasteners, and angle brackets. The behavior of each contacted interface was characterized in both the normal and tangential directions. The normal direction was dictated by a hard contact algorithm while the tangential behavior was dictated by a friction contact algorithm with friction coefficients of 0.3, 0.35, and 0.4 for steel-on-steel, wood-on-steel, and wood-on-wood contact, respectively – except for the tangential behavior between the fastening component and the CLT panel, which was governed by the axial withdrawal behavior discussed above.

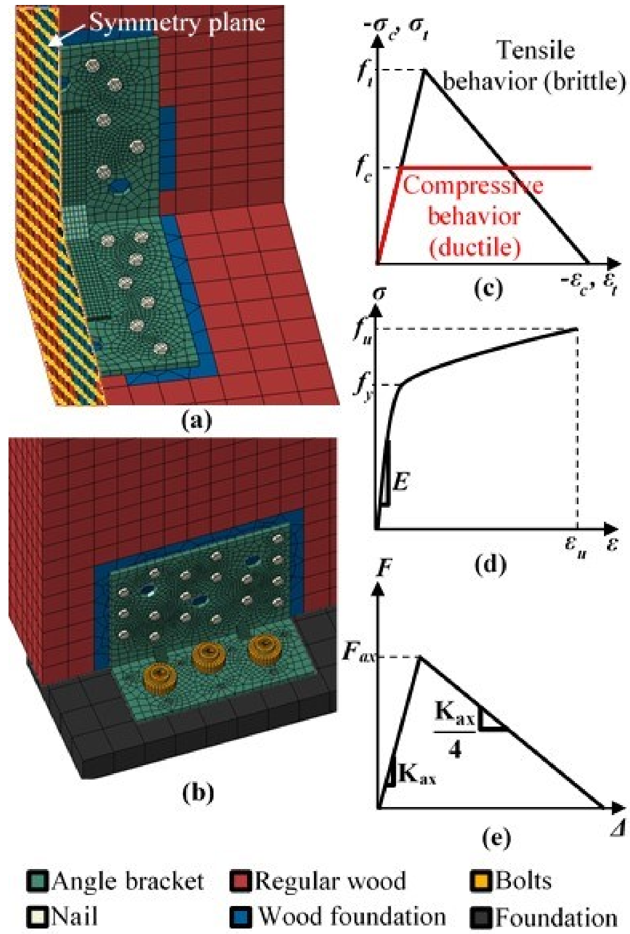

Figure 4-3: Numerical models of the connections and material models used.

Under all load conditions considered, monotonically increasing displacement was applied to the CLT wall panel while the floor panel or foundation steel plate had the bottom face completely fixed. The angle bracket of the wall-to-floor connection has a symmetric configuration, which allowed the half-modeling of the entire system as shown in Figure 4-3a. The boundary conditions applied to the symmetry plane depended on the symmetry of the applied load. Under load conditions that were symmetric in relation to the symmetry plane, fixed translation perpendicular to the symmetry plane was considered, while under load conditions that were asymmetric in relation to the symmetry plane, fixed translations in the symmetry plane axes were considered.

4.5 Validation of the Modeling Procedure

An experimental study from the literature was used to validate the high-fidelity nonlinear numerical models developed. As previously discussed, due to the lack of literature data on the out-of-plane response of CLT connections, extra effort was taken to ensure that the finite element model created well captured the mechanisms observed for the connection responses available in the literature. Mahdavifar et al. [35] tested the connections with the nailing patterns shown in Figure 4-4 on CLT panels made of Douglas-Fir. The specimens had the dimensions shown in Figure 4-2. Each connection was subjected to axial and in-plane shear load conditions (i.e., towards the y and x axes, respectively, in Figure 4-2). More details on this experimental study can be found elsewhere [35].

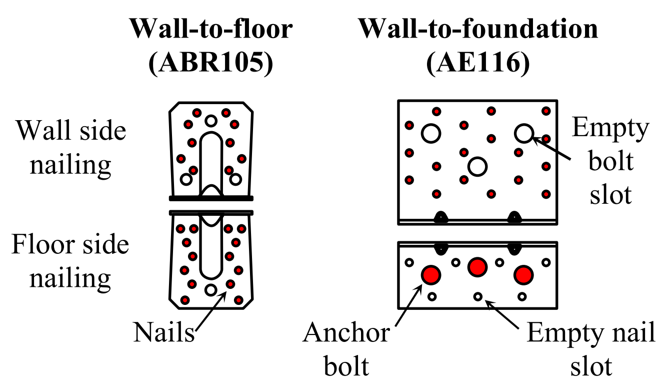

Figure 4-4: Nailing patterns used in the experimental investigation.

The numerically predicted behaviors are compared with the experimental ones in Figure 4-5. The results yielded a good agreement with the experimental response. The calculated axial responses were able to accurately capture the nonlinear stages of the experimentally observed behavior. A softer initial stiffness was calculated by the models, which can be attributed to the uncertainties in both the material properties of the wood panel and the determination of the parameters of the nail's axial withdrawal model. The calculated shear responses were able to accurately predict the stiffness in the wall-to-floor model while slightly overestimating it for the wall-to-foundation connection. This phenomenon can be attributed to the higher experimental flexibility resultant of, for example, the top flange of the steel C-section used as foundation versus the perfectly fixed foundation steel plate used in the numerical model.

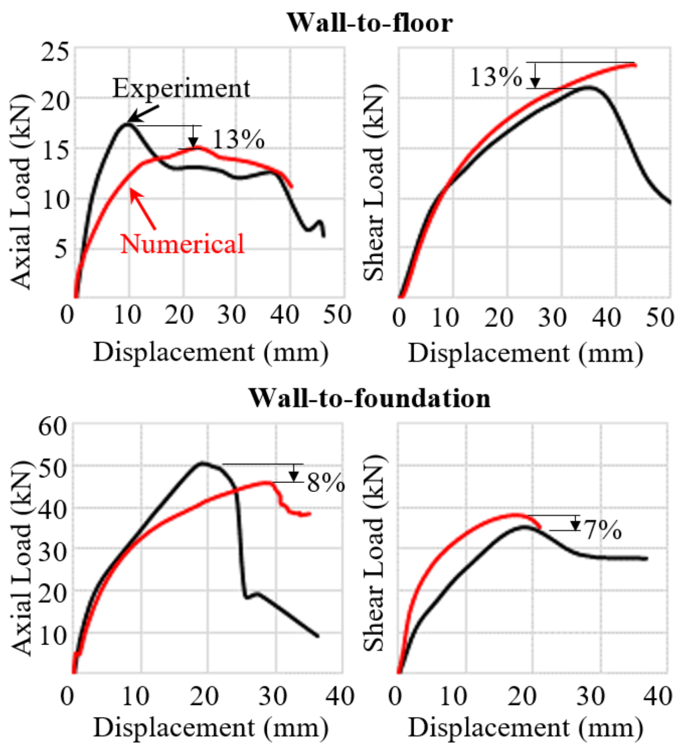

Figure 4-5: Validation of the numerical models.

The developed models were also able to capture the failure mechanisms. As reported in Mahdavifar et al. [35], for the axial load condition, the wall-to-floor connection failure occurred due to damage on the floor side of the connection caused by the axial withdrawal of the nails. This failure mechanism started at the nails closest to the wall and propagated towards the nails further away from the wall as the axial load increased as shown in Figure 4-6a, where the von Mises stress is the square-root of a sum of stress values squared; therefore, it is a positive scalar quantity. The wall-to-foundation connection failure occurred due to the rupture of the steel connector around the bolt holes on the floor side of the connection with minimal damage on the wall side as shown in Figure 4-6c. In Figure 4-6c, the anchor bolts are omitted due to its significantly larger yield strength as compared to that of the angle bracket and the nails. This was also done for all the other figures that show the failure stress condition of the wall-to-foundation connection to improve the visualization of the stresses in the angle bracket and the nails. For the shear load condition, both connections failed in similar ways. The crushing of the wood fibers in contact with the nail shanks on the wall side of the connection led to the bending of the nail shanks and subsequent formation of plastic hinges as shown in Figure 4-6b and Figure 4-6d. This nail behavior formed within the topmost layer of the CLT panel and did not penetrate to the core layers.

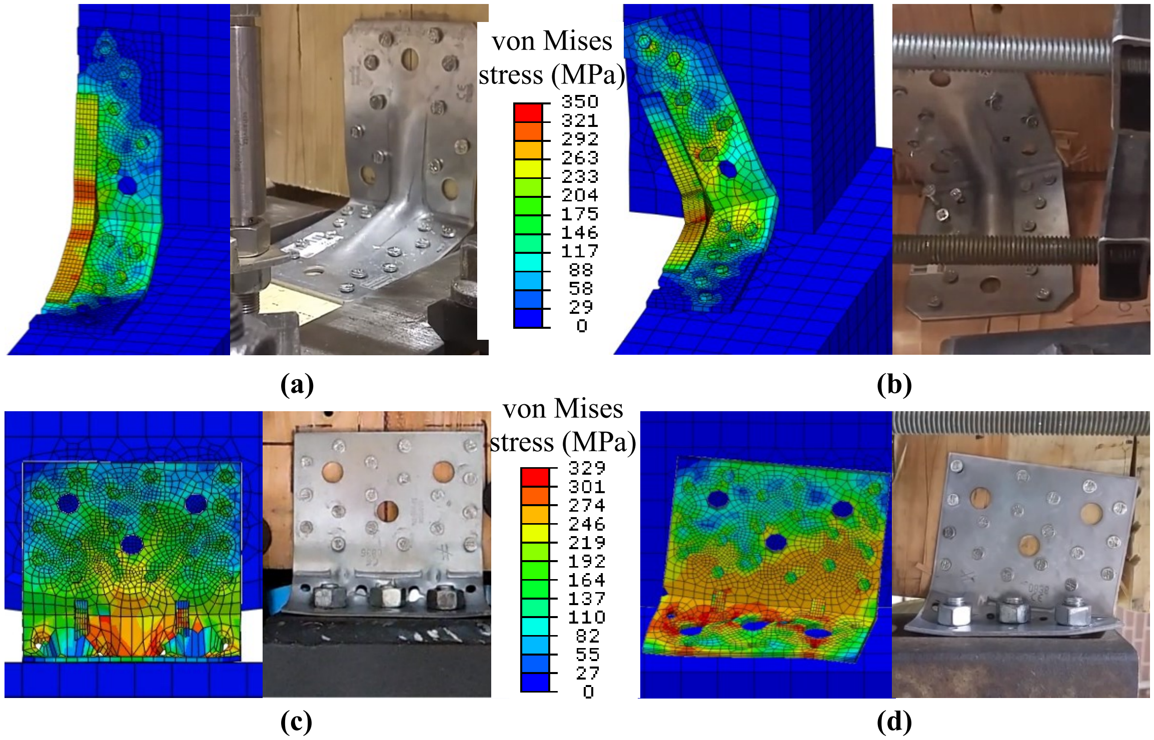

Figure 4-6: Side by side comparison of the numerical and experimental [35] behaviors under a) axial and b) shear load for the wall-to-floor and c) axial and d) shear load for the wall-to-foundation connectors.

4.6 Out-of-Plane Behavior of CLT Connections

The connection models experimentally validated in Section 4 were used to develop a fundamental understanding and characterize their behavior under two tsunami-induced out-of-plane load conditions shown in Figure 4-7. The first condition is representative of a tsunami force that impacts the exterior wall of the building, forcing the out-of-plane CLT panel to move towards the inside of the structure (referred to out-of-plane exterior, or OPE). The second condition is representative of the interior pressure exerted by the tsunami inundation that has entered the building, forcing the out-of-plane CLT panel to move towards the outside of the building (referred to out-of-plane interior, or OPI).

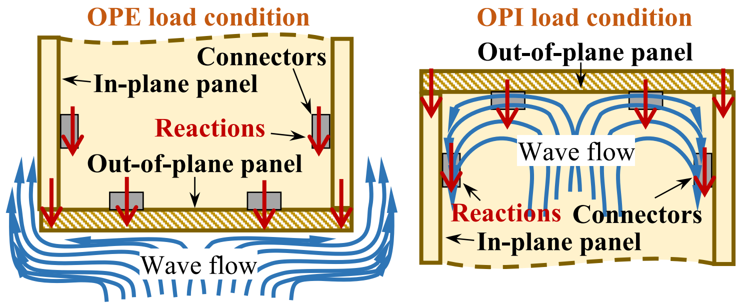

Figure 4-7: OPE and OPI load conditions investigated.

The numerically predicted behaviors of the connections under OPE load condition are shown in Figure 4-8. When subjected to the OPE load condition, the wall panel moves towards the interior of the building, pushing the angle brackets against the lower section of the panel. As a consequence, in both wall-to-floor and wall-to-panel connections, the OPE behavior was dictated by the crushing of the wall panel's wood fibers onto the lower section of the angle brackets as shown in Figure 4-8a and Figure 4-8b. This occurred because the fasteners on the floor side of the connections are the primary out-of-plane shear resistant elements for both connections, which resulted in higher stresses in the wall panel around this region. In addition to the damage of the wall panel, significant vertical bending of the nail shanks on the wall side of the connection was observed due to the tendency of the connection to move upwards as the OPE load increased as shown in Figure 4-8a. On the other hand, no significant bending or axial withdrawal was observed in the nails or the anchor bolts on the floor side of the connections. This can be explained by the bending imposed on the angle bracket by the crushed wall panel, which causes a "push down" effect as shown in Figure 4-8a. This effect applied a downward force on the floor flange of the angle bracket that increased the friction between the floor panel and the bracket.

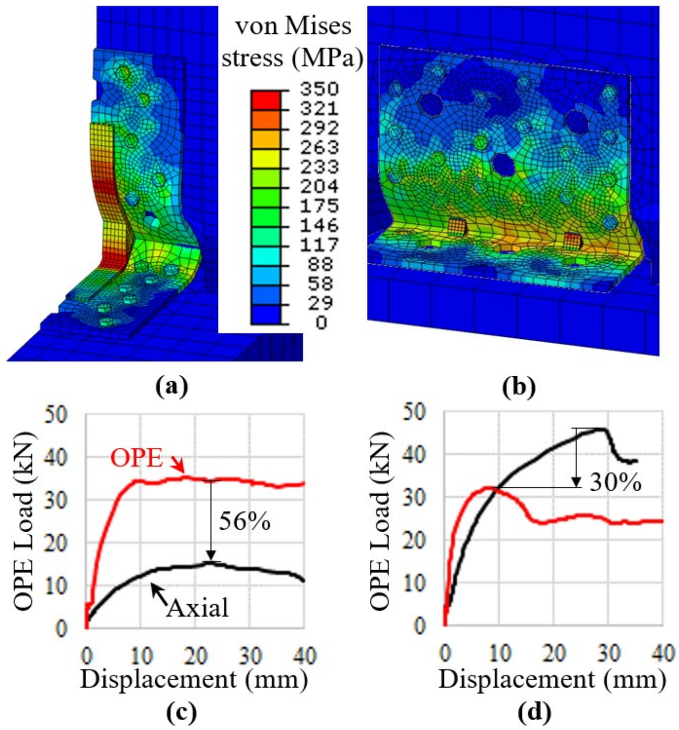

Figure 4-8: Numerical behavior of the wall-to-floor and wall-to-foundation connections under OPE load condition.

Figure 4-8c and Figure 4-8d show the force-displacement response of the connections as compared to their axial response obtained in Section 4. The OPE response was significantly stiffer than the axial response for both connections and significantly stronger than the axial response for the wall-to-floor connection. Despite the load capacities of the connections under OPE load condition being attained at an average of 40% lower displacements than under axial load, the post-peak behavior presented a favorable plateau. The plateau reflected the modeled post-peak compressive ductile behavior of the wood panels. The similar axial and OPE load capacities in the wall-to-foundation connection can be explained by the types of fasteners used on the floor side of the connection. As a result, the three high-strength anchor bolts fastened to the foundation steel plate provided significantly more strength against the out-of-plane movement imposed by the wall panel.

The numerically predicted behaviors of the connections under OPI load condition are shown in Figure 4-9. When subjected to OPI load condition, the behavior of both connections was governed by the axial withdrawal of the nails on the wall side of the connection. This behavior is similar to the one observed under the axial load condition (discussed in detail Section 4) where the axial withdrawal of the nails on the floor side of the connection dictated the behavior of the wall-to-floor connection. At the failure condition, no significant damage was observed on the floor side of the connections as shown in Figure 4-9a and Figure 4-9b. The OPI response was significantly weaker than the axial response as shown in Figure 4-9c and Figure 4-9d. This occurred due to the lower number of nails on the wall side of the connection compared to the floor side of the connection. Furthermore, the OPI response of the wall-to-floor connection was more ductile than that under the axial load (i.e., 2 times higher the peak displacement) while the response of the wall-to-foundation connection had approximately the same ductility. Despite the axial withdrawal of the nails on the wall side of the connection dictating the behavior, it was observed that not all the nails used on the wall side contributed to the load capacity of the connections. Figure 4-9a and Figure 4-9b show the nails that did and did not contribute to the load capacity of the connections with solid and dashed circles, respectively. Only the first four nails of the ten and the first six nails of the eighteen on the wall side of the wall-to-floor and wall-to-foundation connections, respectively, contributed to the load capacity of the connections. This result revealed a 60% inefficiency (i.e., only 40% of the available nails contributed in the load capacity) of both connections to OPI load conditions. Furthermore, the comparison of the load-displacement response of the connections under OPI and OPE load conditions (see Figure 4-8 and Figure 4-9) show that the load capacity in the OPE direction was, on average, 2.3 and 1.7 times higher than the OPI for the wall-to-floor and wall-to-foundation connectors, respectively.

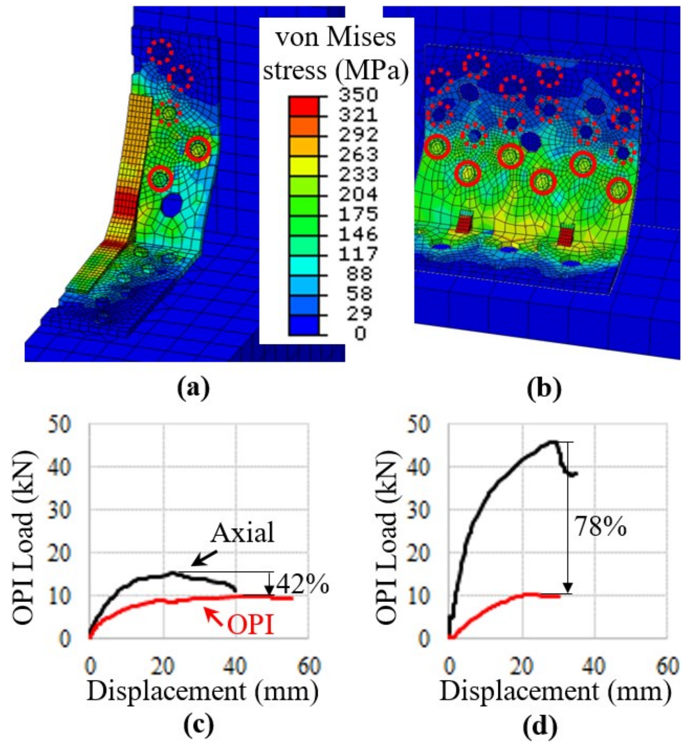

Figure 4-9: Numerical behavior of the wall-to-floor and wall-to-foundation connections under OPI load condition.

4.7 Influence of Key Connection Design Parameters on the Out-of-Plane Behavior

A numerical investigation with 48 models under the two out-of-plane load conditions was performed to study the influence of three key connection design parameters on the behaviors of each connection. Half of the models were subjected to OPE load condition while the other half were subjected to OPI load condition. Each model employed a different combination of the levels of the analyzed key connection design parameters shown in Figure 4-10. The behavior of each model was assessed based on the engineering demand parameters (EDP) of load capacity and peak displacement. The influence of the key connection design parameters was identified and quantified based on the analysis of variance (ANOVA) method. This is a useful method to assess if the variation in the calculated EDPs due to the changes in single or multiple parameters is statistically significant [47]. The analysis of variance relies on partitioning the total variability of the collected dataset, which is measured as the total sum of squares of the dataset, into components associated with each considered parameter. The contributions of each parameter and their respective interactions are then determined as the percentage of their associated components relative to the total sum of squares. Table 4.1 numerically presents the ANOVA analysis results, while Figure 4-11 visually presents the calculated EDP values for each combination of the key connection design parameters considered.

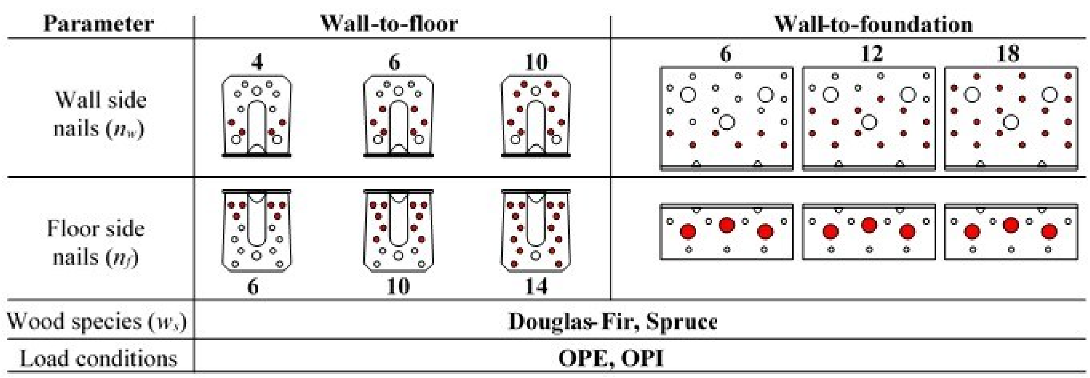

Figure 4-10: Key connection design parameters considered for the wall-to-floor and wall-to-foundation connections.

Table 4.1: ANOVA results for the OPE and OPI load conditions.

OPE load condition					
Wall-to-floor			**Wall-to-foundation**		
	Contribution			**Contribution**	
Param.	**Load Capac.**	**Peak Disp.**	**Param.**	**Load Capac.**	**Peak Disp.**
w_s	80.4%	13.9%	w_s	96.9%	77.0%
n_f	0.1%	60.8%	n_w	0.2%	0.2%
n_w	17.7%	21.0%	w_s - n_w	2.9%	22.8%
w_s - n_f	1.0%	0.1%	***Total***	***100%***	***100%***
w_s - n_w	0.0%	0.3%			
n_f - n_w	0.2%	2.3%			
w_s - n_f - n_w	0.5%	1.6%			
Total	***100%***	***100%***			
OPI load condition					
Wall-to-floor			**Wall-to-foundation**		
	Contribution			**Contribution**	
Param.	**Load Capac.**	**Peak Disp.**	**Param.**	**Load Capac.**	**Peak Disp.**
w_s	2.1%	0.0%	w_s	16.3%	19.6%
n_f	0.4%	65.0%	n_w	82.1%	80.2%
n_w	96.3%	34.8%	w_s - n_w	1.5%	0.2%
w_s - n_f	0.2%	0.0%	***Total***	***100%***	***100%***
w_s - n_w	0.7%	0.0%			
n_f - n_w	0.1%	0.1%			
w_s - n_f - n_w	0.1%	0.0%			
Total	***100%***	***100%***			

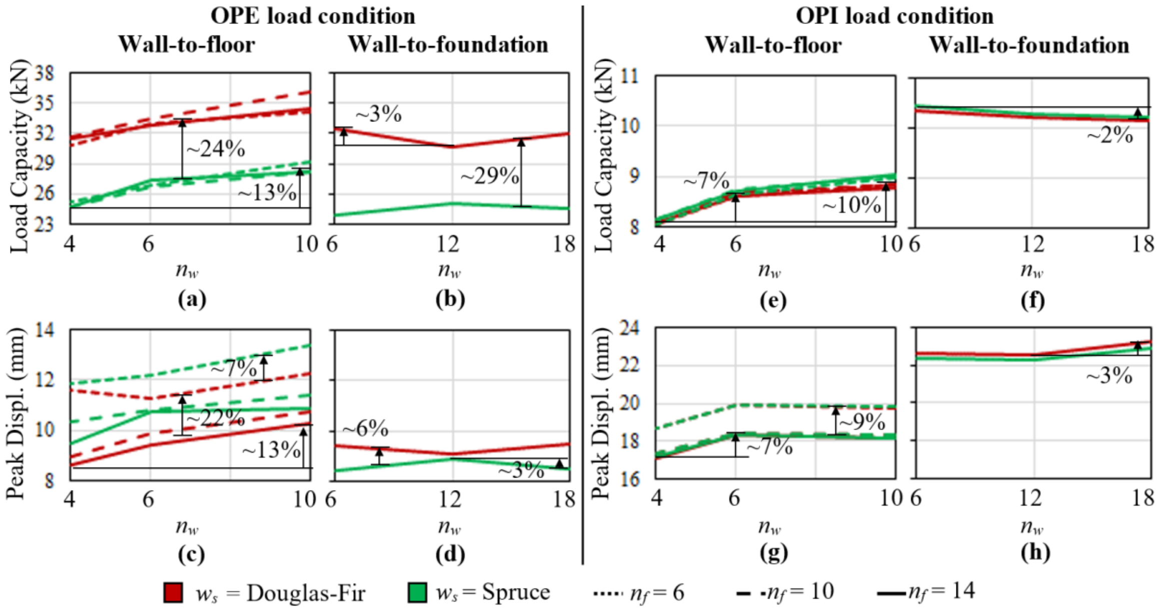

Figure 4-11: Calculated load capacities and peak displacements of the models subjected to OPE and OPI load conditions.

4.7.1 Influence on the OPE Behavior

For the load capacity of the wall-to-floor connection, the analysis results indicate that the w_s and n_w parameters had the most significant contribution to the behavior with 98.1% of the total variability (see Table 4.1). The calculated contribution of w_s was significantly higher than the contribution of n_w, which made the load capacity more sensitive to the change in w_s as shown in Figure 4-11a. For the load capacity of the wall-to-foundation connection, the analysis results indicate that the w_s parameter alone had the most significant contribution to the behavior with 96.9% of the total variability (see Table 4.1 and Figure 4-11b). These results are physically confirmed by the calculated failure modes. For both connections, the failure mode was primarily governed by the crushing of the wall panel's wood fibers. For the wall-to-floor connection, the failure mode was secondarily dictated by the bending of the nail shanks on the wall side of the connection. These failure modes were discussed in more detail in Section 5 (see Figure 4-8a and Figure

4-8b) and were observed for all combinations of key connection design parameters investigated. Consequently, w_s was the most influential parameter for the OPE load capacity of both connections.

For the peak displacement of the wall-to-floor connection, the analysis results indicate that the n_w, n_f, and w_s parameters had the most significant contribution to the behavior with 95.7% of the total variability (see Table 4.1). The calculated contribution of n_f was much higher than the contributions of n_w and w_s, which resulted in a higher influence of n_f on the peak displacement of the wall-to-floor connection. Figure 4-11c shows that n_f only significantly influenced the peak displacement at its lowest level (i.e., six nails) while no significant influence occurred at subsequent n_f levels. For the peak displacement of the wall-to-foundation connection, the analysis results indicate that the w_s parameter and the w_s - n_w interaction had the most significant contribution to the behavior with 99.8% of the total variability (see Table 4.1). Figure 4-11d, however, shows that the effective influence of these parameters on the peak displacement of the connection was negligible. These results are physically confirmed by the fasteners on the floor side of the connections, which were the primary out-of-plane shear resistant elements. Consequently, for the wall-to-floor connection, the lowest level of n_f increased the bearing stresses that each nail imposed on the wood panel, which resulted in larger deformations. For the wall-to-foundation connection, no significant influence was calculated for the peak displacement because the anchor bolts were significantly stronger, rigidly attached to the foundation steel plate, and not part of the numerical investigation.

4.7.2 Influence on the OPI Behavior

For the load capacity of the wall-to-floor connection, the analysis results indicate that the n_w parameter alone had the most significant contribution to the behavior with 96.3% of the total variability. This result is shown in Figure 4-11e, where all the lines are approximately concurrent. For the wall-to-foundation connection, the analysis results indicate that the n_w and w_s parameters had the most significant contribution to the behavior with 98.4% of the total variability (see Table 4.1). Figure 4-11f, however, shows that the effective influences of these parameters on the load capacity of the connection were negligible. These results are physically confirmed by the calculated failure modes. For both connections, the failure mode was primarily dictated by the axial withdrawal of the nails on the wall side of the connection. Furthermore, the numerical investigation revealed that despite the level of n_w used in the connections, only the four and six nails closest to the bend line of the angle bracket contributed to the load capacity of the wall-to-floor and wall-to-foundation connections, respectively. As a result, Figure 4-11e indicates a marginal increase in load capacity at n_w levels above four nails for the wall-to-floor connection while Figure 4-11f indicates no significant increase in load capacity at n_w levels above six nails for the wall-to-foundation connection. Figure 4-12 shows the nails that did and did not contribute to the load capacity of the connections with solid and dashed circles, respectively. In Figure 4-12, the stresses were omitted to improve visualization and the responses of the wall-to-floor connection with n_w = 10 and the wall-to-foundation connection with n_w = 18 are shown in Figure 4-8c and Figure 4-8d. These results support two important conclusions: (i) n_w was the most influential parameter for the load capacity of both connections, and (ii) not all the available nails on the wall side of the connection contributed to the load capacity of the connection.

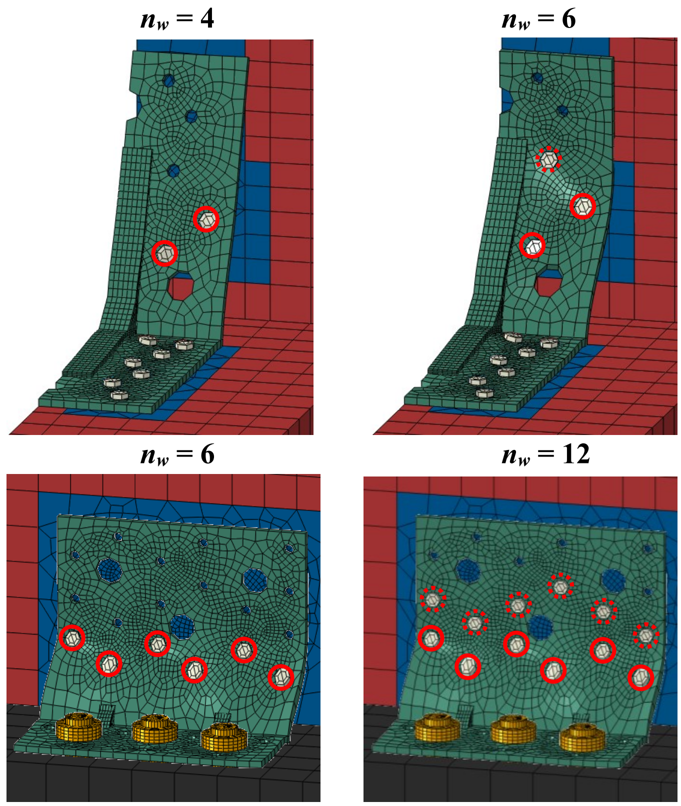

Figure 4-12: Nails that did and did not contribute to the OPI behavior of the connections.

For the peak displacement of the wall-to-floor connection, the analysis results indicate that the n_f and n_w parameters had the most significant contribution to the behavior with 98.8% of the total variability (see Table 4.1). The calculated contribution of n_f was double the contribution of n_w, which resulted in a higher influence of n_f on the peak displacement of the connection, as shown in Figure 4-11g. The contribution of n_f and n_w was only significant, however, at their respective lowest levels while no significance occurred at subsequent levels. For the peak displacement of the wall-to-foundation connection, the analysis results indicate that the w_s and n_w parameters had the most significant contribution to the behavior with 99.8% of the total variability (see Table 4.1).

Figure 4-11h, however, shows that their effective influences on the peak displacement were negligible. The influence of n_w is physically confirmed by the contribution of only part of the nails on the wall side of the connection to the behavior, as discussed for the load capacity of the connections. In addition, the influence of n_f in the wall-to-floor connection is explained by the fasteners on the floor side of the connection, which were the primary out-of-plane shear resistant elements. Consequently, the lowest level of n_f increased the bearing stresses imposed by each nail in the wood panel and resulted in larger deformations.

4.8 Simplified Equations and Procedures

4.8.1 A Simplified Equation for Estimating the OPE Load Capacity

The crushing of the wall panel's wood fibers onto the lower section of the angle brackets was the dominant failure mode for the wall-to-floor and wall-to-foundation connections under OPE load condition, as discussed in Section 5 and Section 6.1. Further analysis of the failure conditions indicated that, for each combination of connection and wood species studied, the crushing occurred throughout the entire length of the connection (L_c in Figure 4-13a) and at approximately the same distance from the bend line of the angle bracket (λHc in Figure 4-13a), called herein the crushing distance. Benefiting from this finding, a simplified equation is proposed to estimate the load capacity of wall-to-floor and wall-to-foundation CLT connections (see Eq. 3). The equation is based on the product of the compressive strength of the wood species of the wall panel in the direction of the OPE load ($f_{c,w}$) by the rectangular area of sides L_c and λH_c. Since the properties of the wood species and the geometry of the connection is usually known, the λ factor is derived in this study based on the statistical analysis of the results of the numerical investigation conducted in Section 6.1. Figure 4-13b and Figure 4-13c show, for both connections, the ratio of the calculated load capacity of each examined connection configuration over the crushing force using the entire height of the connection (i.e., $\lambda = 1.0$ in Eq. 3). The λ factor was then obtained as the average of the dataset for each connection and wood species studied. Figure 4-13b and Figure 4-13c also indicate that the crushing distance is, on average, 13% greater for softer wood species (Spruce in this study), and 18% greater for the wall-to-floor connection. The coefficient of variation (COV), which is a measure of the dispersion of the dataset around the average value, was calculated and shown in Figure 4-13b and Figure 4-13c. The calculated COVs are well within 10% of the average for all the connections and wood species studied. Thus, the λ factors shown in Figure 4-13b and Figure 4-13c are a good representation of the dataset and appropriate for use in Eq. 3 to obtain reliable estimations of the load capacity under the OPE load condition.

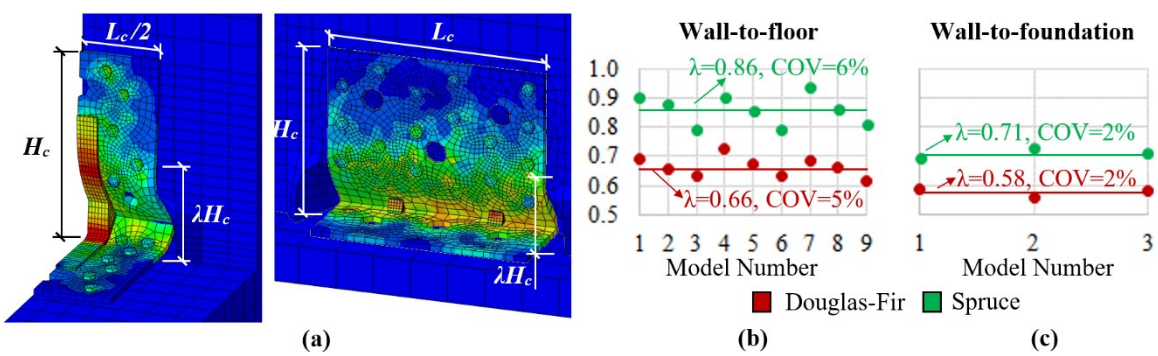

Figure 4-13: a) Failure mode of the connections under OPE load condition (repeated from Figure 4-8) and the λ factor calculation for the b) wall-to-floor and c) wall-to-foundation connections.

4.8.2 A Mechanics-Based Simplified Procedure for Quantifying the Nail Contribution to the OPI Load Capacity

The axial withdrawal of the nails on the wall side of the connections was the dominant failure under OPI load condition. Further analysis of the failure conditions indicated that there was a maximum distance from the bend line of the angle bracket, called herein the withdrawal influence distance (d_{wid}), that dictated which nail contributed to the load capacity of the connection, as discussed in Section 5 and Section 6.2. Thus, a mechanics-based simplified procedure is proposed to determine dwid and enable the quantification of the nail contribution to the OPI load capacity of the connections. The procedure is based on the bending stiffness of the flange of the angle bracket experiencing withdrawal and the axial withdrawal stiffness of the nails. The objective is to determine the distance from the bend line of the angle bracket in which the aggregated axial withdrawal stiffness of the nails ($\sum nK_{ax}$) exceeds the bending stiffness of the angle bracket (K_b) as illustrated in Figure 4-14a. For this purpose, the flange of the angle bracket experiencing the withdrawal is idealized as a fixed cantilever beam with bending stiffness of $3EI/d_i^3$, where E is the modulus of elasticity of the angle bracket's steel; I is the corresponding inertia of the flange of the angle bracket experiencing withdrawal; and d_i is the position of nail i measured from the bend line of the angle bracket (see Figure 4-14a). The procedure is comprised of two simple steps summarized in Figure 4-14b. At the start of the procedure, the index i is set to 1, which refers to the closest nail to the bend line of the angle bracket as shown in Figure 4-14a. In step 1, the bending stiffness of the angle bracket ($3EI/d^3$) and the aggregated axial withdrawal stiffnesses of the nails at position i ($\sum nKax$) are equated and solved for d as shown in Figure 4-14b. In step 2, the calculated value of d and di are compared; if d > di, the index i is incremented by 1, which refers to the next closest nail to the bend line of the angle bracket, and steps 1 and 2 are performed again (see Figure 4-14b). This process is repeated until d exceeds the ith nail position, in which case dwid is determined as d_i-1 – in other words, the last nail position at which step 2 results in a "yes" condition. The nails positioned at a distance within dwid from the bend line of the angle bracket are the ones that contribute to the load capacity of the connection under the OPI load condition.

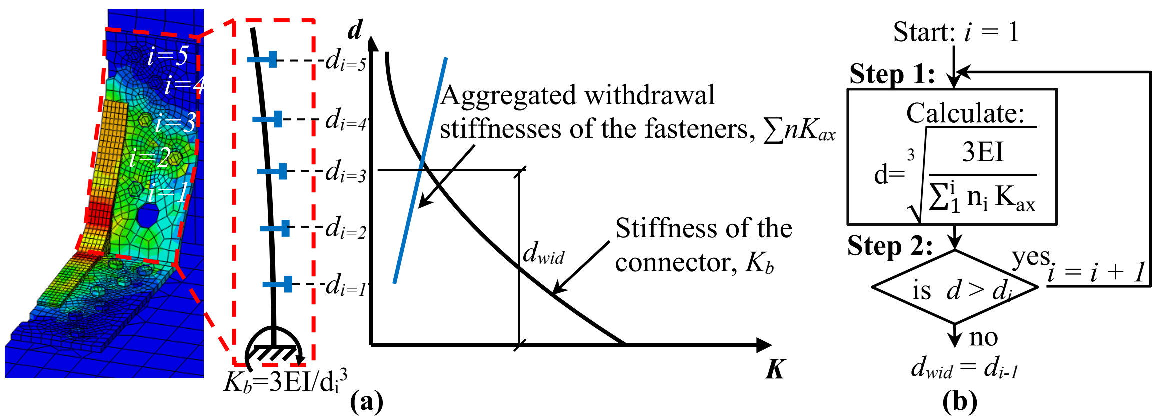

Figure 4-14: Proposed method to determine the withdrawal influence distance.

To verify the accuracy of the procedure, dwid was calculated for the wall-to-floor and wall-to-foundation connections previously investigated. Table 4.2 shows the calculated values of dwid, the number of nails in the angle bracket within this distance, and the number of nails that contributed to the load capacity of the connections under OPI load condition. As it is clear from the table, the proposed method was able to accurately predict which nails contributed to the load capacity of the connections when subjected to OPI load condition.

Table 4.2: Calculated and predicted number of nails that contribute to the load capacity.

	d_{wid} (mm)	# Nails Within d_{wid}	# Nails Contributing to Load Cap.
Wall-to-floor	42	4	4
Wall-to-foundation	29	6	6

4.9 Summary and Conclusions

CLT wall-to-floor and wall-to-foundation connections were studied in order to understand and characterize their behavior under two tsunami-induced out-of-plane load conditions. The first condition is representative of a tsunami force that impacts the exterior wall of the building (referred to as OPE) and the second condition is representative of the interior pressure exerted by the tsunami inundation (referred to as OPI). It was observed that the behaviors of the connections were significantly different in the OPE and OPI load conditions. The OPE behavior was dictated by the crushing of the wall panel's wood fibers onto the lower section of the angle brackets and resulted in a stiff pre-peak with a ductile post-peak behavior. The OPI behavior was dictated by the axial withdrawal of the nails on the wall side of the connection and resulted in a softer pre-peak with a softening post-peak behavior. The load capacity under OPE load condition was, on average, 2.3 and 1.7 times higher than under OPI load condition for the wall-to-floor and wall-to-foundation connectors, respectively.

A numerical investigation with 48 models was performed and the analysis of variance (ANOVA) method was used to quantify the influence of three key connection design parameters (i.e., the number of nails on the wall side of the connection, n_w, the number of nails on the floor side of the connection, n_f, and the wood species, w_s) on the out-of-plane behavior of the connections. The results support the following conclusions:

- The w_s parameter was the most influential parameter for the load capacity of the connections under OPE load condition. The change in w_s from Spruce to Douglas-Fir increased the load capacity by 24% and 29%, on average, for the wall-to-floor and wall-to-foundation connections, respectively.
- The n_f parameter was the most influential parameter for the peak displacement of the wall-to-floor connection under OPE load condition. The lowest n_f level of 6 nails increased the peak displacement by 22%, on average, in comparison to the other two n_f levels of 10 and 14 nails, which resulted in approximately the same peak displacements.
- Under OPE load condition, the crushing of the wall panel's wood fibers occurred throughout the entire length and at approximately the same distance from the bend line of the angle bracket. This distance was referred to in this study as the crushing distance and was shown to be, on average, 13% greater for softer wood species (Spruce in this study) and 18% greater for the wall-to-foundation connection.
- The results of the numerical investigation conducted in this study were statistically analyzed to determine the crushing distance and to derive a simplified equation for estimating the OPE load capacity of the CLT connections.
- The n_w parameter was the most influential parameter for the load capacity and the peak displacement of the connections under OPI load condition. This study showed that only 40% of the nails on the wall side of the connections contributed to their OPI load capacity. This result indicated that the connections were 60% inefficient

to OPI load condition and that there was a maximum distance from the bend line of the angle bracket, referred to in this study as the withdrawal influence distance, that dictated which nail contributed to the load capacity of the connection.

- A mechanics-based simplified procedure for quantifying the nail contribution to the OPI load capacity of the CLT connections was proposed based on their calculated withdrawal influence distance. The accuracy of this procedure was verified with the results of the numerical investigation conducted in this study.

4.10 Acknowledgments

The authors would like to thank Dr. Vahid Mahdavifar for providing the experimental data used in this study.

Chapter 5

Journal Paper IV - Life Cycle Assessment of Seismic Retrofit Alternatives for Reinforced Concrete Frame Buildings[4]

5.1 Abstract

Reinforced concrete structures designed prior to modern building codes are still in use today. These structures are known for their inadequate design and fragile performance during earthquakes. Over the past decades, several seismic retrofitting alternatives have been proposed as strengthening solutions for these buildings. Since the construction industry has a significant environmental burden, the impacts of the retrofit solutions should also be considered in the decision-making process of a possible seismic strengthening intervention. In this study, we performed a life cycle assessment (LCA) analysis of three seismic retrofit alternatives for reinforced concrete structures, namely, RC column jacketing, beam weakening, and shear walls. An 8-story reinforced concrete case-study building available in the literature was adopted for the LCA analysis. The environmental impacts of the selected alternatives were quantified from cradle-to-grave and two disposal phase options were studied in a sensitivity analysis: landfilling and recycling. Detailed

---

[4] Reprinted from the Journal of Building Materials, Vol 28, Rafael A. Salgado, Defne Apul, Serhan Guner, Life Cycle Assessment of Seismic Retrofit Alternatives for Reinforced Concrete Frame Buildings, 101064, © 2020, with permission from Elsevier. For the published version, please refer to https://doi.org/10.1016/j.jobe.2019.101064.

calculations and assumptions were made in order to obtain the inventory data for the impact assessment of the three alternatives. The calculated LCA results were compared and interpreted among the analyzed retrofit alternatives. The shear wall total environmental impacts were the highest of all the studied alternatives. The pre-installation (i.e., production) and disposal of the materials required by each alternative were the phases with the highest environmental impacts, while transportation impacts were comparatively small. Recycling of the construction and demolition waste reduced the environmental impacts in the disposal phase by 29% to 53%, with a lower total environmental impact reduction of 12% to 42% for all the retrofit alternatives studied.

5.2 Introduction

Reinforced concrete (RC) buildings constructed in the 1970s and earlier are still in use today in both the developing and developed parts of the world. These buildings present a risk of poor performance in earthquakes because they were designed before the 1976 Uniform Building Code which was the first to include design guidelines for ductile behavior during seismic conditions. [1–3]. There is a significant concern about inadequate seismic load resistance of these RC buildings. During the past decades, earthquakes of various intensities (e.g.; 1989 Loma Prieta, 1994 Northridge, Indonesia and Italy, 2009; Haiti, 2010; Nepal 2015) have demonstrated the seismic vulnerability of the building stock and caused extensive human and economic losses. Consequently, considerable efforts have been directed towards seismic retrofit alternatives so as to reduce the seismic hazards posed by in-service old RC buildings. For example, in the USA, in 1984, the Federal Emergency Management Agency (FEMA) began its seismic hazard reduction program which resulted in comprehensive rehabilitation design guidelines such as the FEMA 356 [4]. In addition, the state of California has issued mandatory retrofit programs for pre-1978 RC buildings to reduce structural deficiencies and improve the performance of these buildings during earthquakes.

Seismic retrofit actions for RC structures require the production of new materials (e.g., concrete, reinforcing steel bars, bricks, etc.) and construction processes to implement them onto existing structures (e.g., pouring of concrete, transportation of materials to the building site, etc.). The construction industry is responsible for a considerable environmental impact across the globe in the form of nonrenewable resource depletion, waste generation, energy consumption, and CO_2 emissions [5–7]. When considering the large number of seismically deficient buildings eligible for retrofitting, it is expected that the environmental impacts caused by these retrofit operations will have a detrimental contribution to the environmental footprint in the U.S. and around the world. Consequently, there is a need for the assessment of the impacts on the environment created by the available alternatives for the seismic retrofit of RC structures.

The life cycle assessment (LCA) framework is a valuable tool for evaluating the environmental impacts of products, systems, or processes while considering its entire life cycle. Many different aspects of the civil infrastructure have been studied using the LCA framework and much of the literature focused on new buildings. Some example studies include RC compared to structural steel buildings [8–11], RC compared to wood buildings [12,13], the use of precast concrete alternatives [14], energy consumption of buildings with standard or green roofs [15,16], impacts of low-energy-use buildings [17], and impacts of efficient insulation techniques [18]. There is also some literature on life cycle aspects of retrofits but most of these focused on the life cycle cost characteristics [19–25] and very few studies addressed environmental impacts. Sibanda and Kaewunruen [26] studied the life cycle environmental performance of three retrofit solutions to enhance the resilience of reinforced concrete infrastructure at railway stations subjected to two unique extreme events, flooding and terror attacks. Napolano et al. [27] assessed the life cycle impacts of four different retrofit alternatives for masonry buildings: local replacement of damaged masonry, mortar injection, steel chain installation, and grid-reinforced mortar application. To the authors' knowledge, Vitiello et al. [28] is the only study that presented the life cycle environmental assessment of different seismic retrofitting alternatives for a reinforced concrete building. Their LCA was comprised of a cradle-to-gate analysis of four seismic retrofit alternatives: FRP-based strengthening, FPR-RC jacketing, insertion of RC shear wall, and base isolation. One limitation of their study is that the end-of-life, or disposal phase, was not considered in their analysis. Consequently, additional LCA studies of seismic retrofit alternatives for reinforced concrete buildings are required in order to expand the current knowledge and contribute to the emergence of general trends in this field. In addition, there is also a lack of knowledge related to the environmental impacts of the disposal phase of these retrofit alternatives.

In 2014, RC and bricks accounted for 73.2% of the total construction and demolition (C&D) waste generated in the United States, 22.6% of which (i.e., 84 million tons) originated from RC buildings [29]. Although there is not an official number indicating where the majority of this C&D waste is disposed of, European agencies have reported that 75% of the C&D waste was being landfilled in 2011 [30]. Landfilling, however, is quickly becoming a nuisance since it is estimated that, at the current disposal pace, the United States will run out of landfilling space in the next 17 years [31]. As a result, there has been an increasing effort in preventing landfilling of C&D waste and providing a more environmentally friendly alternative such as recycling, which has the potential of reducing C&D landfilling and preserve natural resources. Consequently, it is of critical importance to include and assess different disposal (i.e., end-of-life) phase alternatives such as landfilling and recycling when environmentally assessing RC retrofit alternatives. Given how retrofit efforts have increased in the past decades, the availability of such data is crucial to fully understand the environmental impacts while providing a basis for an effective decision-making process towards a less environment-degrading retrofit alternative.

In this study, we compared the life cycle environmental impacts of three different retrofit techniques: RC column jacketing, beam weakening, and the addition of RC shear walls. We based our analysis on an existing, seismically deficient, 8-story building in Los Angeles, California, which was originally analyzed by Shoraka et al. for these three retrofit options [32]. We also investigated the environmental impact benefits of recycling the C&D waste generated by each alternative as opposed to landfill disposal. We developed detailed cradle-to-grave LCA models with the objective of assisting practitioners in choosing an effective retrofit alternative and making more informed decisions.

5.3 Methodology

The Life Cycle Assessment (LCA) methodology was used to quantify the environmental impacts of the processes and products of the three retrofit alternatives during their life cycle. The methodology is based on the guidelines contained ISO 14040 [33] and

ISO 14044 [34] and consists of four steps: 1) goal and scope, 2) life cycle inventory, 3) life cycle impact analysis, and 4) interpretation of the results.

5.3.1 Goal and Scope Definition

The goals of this study comprise: 1) establish a comparative LCA study on the environmental impacts associated with three different seismic retrofit alternatives for reinforced concrete buildings 2) draw conclusions and recommendations to assist the decision-making process of each retrofit alternative studied; and 3) perform a sensitivity analysis to evaluate the environmental impact benefits of recycling the C&D waste of the retrofit alternatives.

It is important to note that there are several additional aspects that play important roles in the practical decision-making process of which of the seismic retrofit alternatives analyzed in this study should be implemented. Such aspects include, but are not limited to, the construction speed of each alternative, the costs associated with each alternative, the possible relocation of the building occupants, the possible temporary shutdown of commercial facilities that operate on the building, etc. The main focus of this study, however, is to provide valuable data in the form of environmental impacts to assist in the decision-making process related to each retrofit alternative studied herein.

5.3.1.1 Retrofit Alternatives Considered

FEMA 547 - Techniques for the Seismic Rehabilitation of Existing Buildings [1] recommends different seismic retrofit alternatives for reinforced concrete (RC) buildings. In this study, three alternatives for RC buildings were analyzed: 1) RC column jacketing, 2) the addition of RC shear walls, and 3) beam weakening. These alternatives were selected as possible solutions to the most common failure mechanisms identified for RC buildings under seismic loads [35,36]: 1) column failure due to inadequate flexural or shear strength, 2) shear wall failure, and 3) inadequate structural response mechanisms such as weak-column strong-beam (i.e., columns fail before the beam, resulting in a brittle and undesired failure mode).

The RC column jacketing alternative is one of the most frequently used retrofit solution that aims to increase the strength and deformation capacity of a column in order to avoid shear, axial or flexural failure [32]. It can be classified as an 'add element' technique and consists of adding concrete and steel reinforcement to the exterior of an existing column's cross-section (see Figure 5-1). A few advantages of this alternative are that the increased stiffness of the structure is uniformly distributed and that there is no need for the execution of new foundations (i.e., the added reinforcing bars of the jacket can be anchored to the original footings). Special attention must be taken to ensure proper bonding of the new structural elements to the original structure since the success of the procedure is dependent on the monolithic behavior of the composite element. In addition, if required to cross multiple floors, holes in the slabs are needed to allow the longitudinal bars to pass through [37].

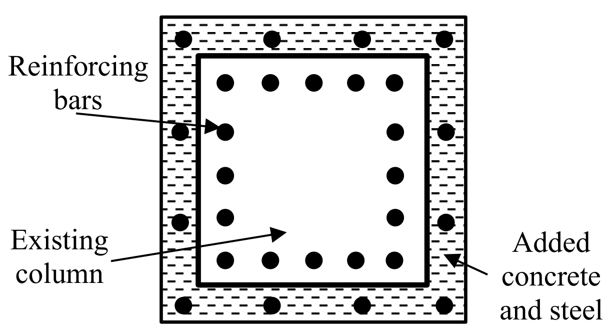

Figure 5-1: RC column jacketing alternative.

The shear wall alternative consists of erecting an entirely new lateral load resisting system through the removal of existing partition walls of the building and construction of a high strength RC shear wall instead (see Figure 5-2). Shear walls are effective in resisting the lateral loads such as those produced by earthquakes and are also effective in resisting uplift forces created by the horizontal loads applied to the top of the wall. The shear wall massive configuration – often top-to-bottom of the building – allows for an effective load transfer to the next shear wall and down to the foundation [38]. In retrofit applications, shear walls resist most of the earthquake loads and limit the displacement behavior of the building while the RC frame system resists very low amounts of earthquake loads [39]. Depending on the height of the building, this alternative can demand large amounts of materials; thus, it is also classified as an 'add element' technique. The shear wall can be constructed on the perimeter or on the inside of the building. Regardless of the location of the shear wall, this alternative typically requires new foundation construction.

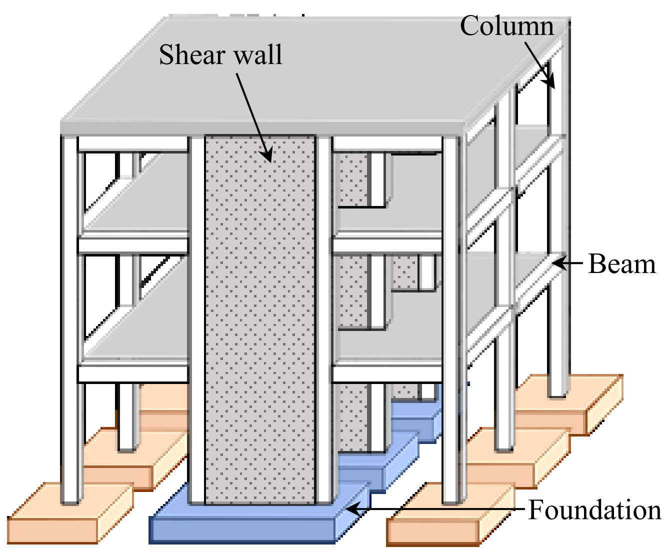

Figure 5-2: Shear wall alternative.

The last alternative studied, the beam weakening technique consists of 'lowering' the strength and stiffness of existing beams in order to shift the building's structural behavior from a brittle strong-beam weak-column to a more ductile strong-column weak-beam behavior (i.e., beams accumulate the damage and provide additional ductility). This alternative is classified as either an 'enhanced performance of existing elements' or 'remove selected components' technique. The beams are weakened by cutting off a portion of the concrete's cross-section and reinforcing steel rebars (see Figure 5-3). By weakening the beams, the structure relies on its capacity to redistribute the loads to the adjacent beams and columns. As such, this technique requires the adjacent structural elements to have enough extra capacity to sustain the added loads. Consequently, the beam weakening alternative might not be suitable to attain strict performance levels as the beams would need to be weakened to a degree greater than the building can safely sustain [28,32].

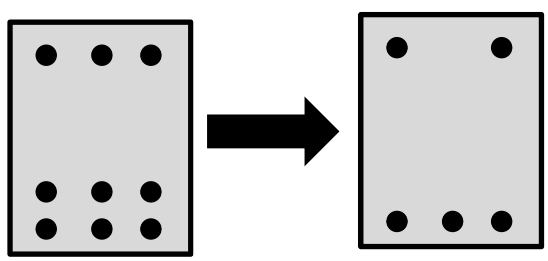

Figure 5-3: Beam weakening alternative.

5.3.1.2 Retrofitted Structure

As a case study for the three retrofit alternatives, a non-ductile seismically deficient RC structure was selected and summarized in Table 5.1 [32]. The RC building is an 8-story moment frame structure with 3 in-plane (see Figure 5-4) and 4 out-of-plane bays (not shown in Figure 5-4). Each floor and each bay (i.e., in- and out-of-plane bays) are spaced at 15 ft. and 25 ft., respectively. The building is located in Los Angeles, California, over class D soil and was designed using the 1967 Uniform Building Code (UBC). The defined earthquake hazard level for the selected performance objectives has a 2% probability of exceedance in 50 years.

Table 5.1: Characteristics of the case-study building [32].

Column Size, h x b (in. x in.)	Column rebar ratio, ρ_{rot}	Column hoop spacing, s (in.)	Beam size, h x b (in. x in.)	Beam rebar ratio, ρ (ρ')	Beam hoop spacing, s (in.)	Floor height (ft)	Bay width (ft)
30x36	3.3%	15	26x36	0.8% (1.0%)	17	15	25

The design of the three retrofit alternatives was performed by Shoraka et al. [32] according to the ASCE 41-13 [40] guidelines considering the earthquake conditions of the building and the target limit state of collapse prevention. Table 5.2 summarizes the design characteristics for each retrofit alternative and Figure 5-4 indicates which structural elements of the original structure required modification. For the RC column jacketing alternative, the calculated retrofit design required modifications on the columns of the first and second floors of all out-of-plane bays, while for the beam weakening alternative, the beams of the first four stories of all out-of-plane bays required weakening. Finally, although Shoraka et al. [32] designed the shear wall retrofit to be placed outside of the building's original structure and connected with it using steel truss elements, in this study, the shear wall was considered to be placed in the middle bay of the building, as in Figure 5-2 and Figure 5-4, for all out-of-plane bays. This consideration aims to avoid the drawbacks of the external shear wall approach such as the noise, dust, and vibration associated with the construction, the potential disruption of access and egress, as well as the requirement that the sides of the buildings be unobstructed for the installation of new shear walls [1,41], which might not be possible in a downtown area. In addition, shear walls constructed outside the original building's frame require careful connection design, since they are responsible to transfer the loads from the new lateral load resisting system to the main building's frame. There have been recent cases of bad performance of these connections under cyclic loads in recent earthquakes, such as the CTV building case in the 2011 New Zealand earthquake, where the entire building's frame collapsed during the earthquake while the exterior shear walls remained standing [42,43].

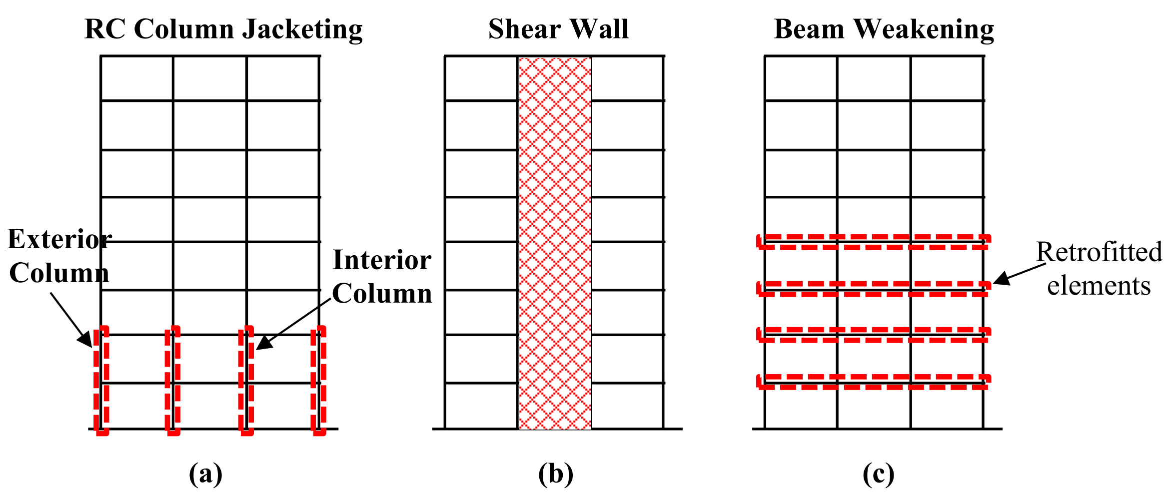

Figure 5-4: Affected elements of the original structure in the calculated design of (a) RC column jacketing, (b) shear wall, and (c) beam weakening retrofit alternatives for the collapse prevention limit state.

Table 5.2: Design properties of each retrofit alternative. ρ_{sh} is the shear reinforcement (i.e., stirrup) ratio; b_f is the width of the flange of the shear wall; t_f is the thickness of the flange of the shear wall; L is the total length of the shear wall; L_w is the length of the web of the shear wall; t_w is the thickness of the web of the shear wall; ρ_f is the longitudinal reinforcement ratio of the flange of the shear wall; ρ_w is the longitudinal reinforcement ratio of the web of the shear wall; ρ is the longitudinal bottom reinforcement ratio of the beam; and ρ' is the longitudinal top reinforcement ratio of the beam [32].

RC Column Jacketing							
Floor	**Columns**	**Original**			**Retrofitted**		
		ρ_{sh}	**b (in.)**	**h (in.)**	**ρ_{sh}**	**b (in.)**	**h (in.)**
1	Exterior	0.36%	26	28	*0.60%*	*27*	*32*
	Interior	0.50%	30	36	*1.00%*	*31*	*40*
2	Exterior	0.31%	26	28	*0.60%*	*27*	*32*
	Interior	0.40%	30	36	*1.00%*	*31*	*40*

Shear Wall						
b_f (in.)	**t_f (in.)**	**L (in.)**	**L_w (in.)**	**t_w (in.)**	**ρ_f**	**ρ_w**
12	5	50	40	8	0.04	0.0025

Beam Weakening								
Floor	**Original**				**Retrofitted**			
	b (in.)	**h (in.)**	**ρ**	**ρ'**	**b (in.)**	**h (in.)**	**ρ**	**ρ '**
1	26	36	0.75%	1.00%	*26*	*30*	*0.75%*	*0.75%*
2	26	36	0.75%	1.00%	*26*	*30*	*0.75%*	*0.75%*
3	26	36	0.755	1.00%	*26*	*30*	*0.75%*	*0.75%*
4	26	36	0.70%	0.93%	*26*	*30*	*0.70%*	*0.70%*

5.3.1.3 System Boundaries

A frequently adopted functional unit for LCA studies on buildings is the unitary internal-usable floor area (e.g., 1m^2 of net floor area) or the unitary mass (e.g., 1m^3 of material) for LCA studies of materials. These functional units provide standardization for comparisons and scalability for buildings with different floor areas or material quantities. In this study, however, three fundamentally different retrofit alternatives that require different amounts of materials and impact a different number of building components are compared. Consequently, the discussed functional units could not accurately compare the impacts amongst the different retrofit alternatives. To enable the direct comparison, the functional unit was considered as a function of their common design goal: to enable the building to meet the collapse prevention limit state (see Section 3). Thus, in this study, the functional unit was chosen as the retrofit design specifications (i.e., the dimensions and materials required by each of the three alternatives) to conform the original structure to the target limit state of collapse prevention.

To estimate the environmental impacts, each retrofit alternative was separated into three distinct phases: pre-installation, installation, and disposal (see Figure 5-5). Previous studies have subdivided the installation phase into two groups of processes, namely, the processes required to be performed in order to prepare the original structure to receive the retrofit (i.e., preparation processes) and the processes required to construct the retrofit on the structure itself (i.e., construction processes) [28]. Table 5.3 shows all the installation phase's processes identified in this study for the three retrofit alternatives separated into the preparation and construction processes groups.

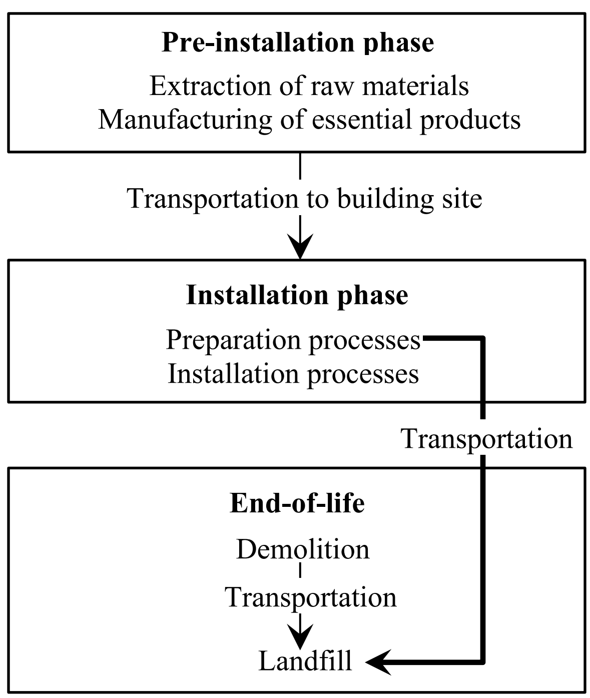

Figure 5-5: LCA phases considered.

Table 5.3: Preparation and installation phases discrete processes.

Preparation processes	Construction processes
Partial demolition of slab	Concrete cast in place
Brick removal	Slab reconstruction
Column/beam concrete cover removal	Foundation construction
Excavation for foundation strengthening	Steel reinforcement placement
Transport of ruins to landfill	Transport of construction materials
	Brick wall reconstruction

The use phase of the retrofit alternatives was not included in the analysis as it is not expected that the retrofit actions will have any significant impact on the energy consumption of the building during its normal usage. In addition, due to the difficulty in estimating the potential maintenance processes that the retrofit alternatives might require in the case of an earthquake of lower-than-designed magnitude hitting the building during its life, each retrofit alternative was considered to perform optimally until the end of its desired lifespan.

The lifespan (i.e., time boundary) of the retrofit alternatives was considered from the moment the retrofit is implemented on the building to the point where the building is demolished (and so is the retrofit system), or the retrofit system needs to be demolished due to damage caused by an earthquake. This lifespan consideration was possible since all the retrofit alternatives were designed to meet the same limit state, which enforces a similar structural performance (e.g., if an earthquake causes one retrofit system to have to be demolished, all the others would need to be demolished as well). Consequently, this lifespan consideration excludes the possibility of one retrofit alternative having a longer lifespan than the others.

In the end-of-life phase – and when processes of the installation phase require demolition of part of the original structure – the construction and demolition waste of the retrofit alternatives was considered to be transported to a landfill facility. By including the disposal, or end-of-life, phase of the retrofit alternatives materials, the boundary condition of the LCA performed can be classified as cradle-to-grave analysis.

5.3.2 Life Cycle Inventory

To collect and calculate the life cycle inventory of the three retrofit alternatives, global (i.e., applies for all retrofit alternatives) and alternative-specific assumptions are considered. The global assumptions are:

- The building is located in downtown Los Angeles. Based on the building's location and existing concrete and rebar industries, the transportation distances for each of these materials are 6.4 km (4 miles) and 4.8 km (3 miles), respectively.
- A lightweight concrete brick with common measurements of 20.32x20.32x40.64 cm (8 x 8 x 16 in.), weight of approximately 5.5 kg (12 lb.), and thickness of the sides of 2.54 cm (1 in.) is used for the wall demolition and reconstruction processes.
- The brick mortar (i.e., cement) necessary to reconstruct the brick walls have commonly used mortar dimensions of 10 mm (0.4 in.) high by 10 mm (0.4 in.) wide along the edges of the concrete brick. The mortar mix is also based on common practice, where 1 part of cement is mixed with 6 parts of sand.
- Two commercially available demolition trucks are used for the demolition of the entire building with a workday of 8 hours per day and taking 8 days to demolish the entire building. The engine power of the trucks is 270 kWh. This energy demand was converted into fuel requirements (i.e., diesel), based on an engine thermal efficiency of 35% and assuming that, on average, the engine works at 65% of full

power during the 8 hours of work (i.e., to consider that the machine will not work at full power during the entire workday).

Each life cycle phases considered were broken down by their specific unit processes, which are presented in a flowchart configuration in Figure 5-6 and are discussed next together with their alternative-specific assumptions.

5.3.2.1 RC Column Jacketing

The pre-installation phase of the RC column jacketing alternative requires the production of concrete and reinforcing steel bars, and their shipping to the building site (see Figure 5-6). In the installation phase, partial demolition of the slabs that intersect the affected columns is required to structurally 'connect' the new column to the existing slab. In addition to the new column size, five inches are added to the demolished dimension of the slabs to allow formwork placement for the column jacketing. Only the concrete portion of the slabs is demolished while the steel reinforcement was kept in place to support the rest of the slab. This demolition process is done using a commercially available concrete saw with a power rate of 2.4 kWh at an assumed operator rate of 2 demolished slabs per hour.

Following the slab demolition, the bricks of the walls that surround the affected columns are removed to enable the expansion of the column dimensions and the position of the formwork. One brick from each side of the column – throughout the floor height – is manually removed (e.g., hammering), with no need for electrical tools. Subsequently, the removal of the concrete cover of the existing column is performed to ensure proper adherence of the new concrete to the core of the existing column. The same saw used to demolish the concrete slabs and an operator productivity of 2 columns per hour were considered in this process. Once the column's core is exposed, new steel reinforcement is manually placed on the retrofitted columns. New concrete is then cast on the columns and on the partially demolished slabs. A commercially available truck-mounted concrete pump capable of pumping 100 m3 of concrete per hour at an energy rate of 150 kWh is used for electricity calculation. Finally, the brick wall is manually reconstructed following the global assumptions stated in this section (see Figure 5-6).

5.3.2.2 Beam Weakening

Because the beam weakening alternative removes concrete and steel reinforcement from existing beams of the building, the pre-installation process produces and ships concrete bricks only, necessary for the wall reconstruction process in the installation phase. The installation phase starts with the removal of the bricks from the walls that intersect the affected beams. Three rows of bricks are removed from the walls below the beams – throughout the length of the beam – to comfortably allow for the sawing tools and human operation. The concrete cover of the existing beams is then removed in order to reach the affected longitudinal reinforcement, which is also removed. The same saw used to demolish the concrete slabs in the RC column jacketing alternative and an operator productivity of 2 beams per hour were considered in this process. Finally, the brick wall is manually reconstructed following the global assumptions stated in this section (see Figure 5-6).

5.3.2.3 Shear Wall

For the shear wall alternative, the pre-installation phase requires the production and shipment of a large quantity of concrete and reinforcing steel bars to the building site. The installation phase starts with partially demolishing the slabs that intersect with the new walls (see Figure 5-6). Differently from the additional 5 inches used in the RC column jacketing, ten inches were added to the demolished dimension of the slabs to accommodate the formwork in the shear wall alternative. All the bricks of the walls where the shear wall is constructed are then manually removed, similarly to all the other alternatives.

Due to its load-bearing structural characteristics, new foundations are required to accommodate the shear walls. The construction of the foundations is comprised of two processes: excavation and foundation construction (i.e., concrete and steel reinforcement placing). Since the details of the foundation required to withstand the loads of the added shear wall used in this study were not given, a shear wall foundation design from the literature was used [41]. To be conservative, the amount of steel reinforcement considered in this study was doubled in comparison to the amount reported in the literature foundation design. The soil removed from the excavation was assumed to be re-used on the construction site. Once the foundation is constructed, the shear wall steel reinforcement is manually placed, and the new concrete is cast. The same truck-mounted concrete pump used to cast concrete in the RC column jacket alternatives was considered for all the concrete pumping operations in the shear wall alternative.

5.3.2.4 Disposal phase

To allow the direct comparison of the impacts generated by each retrofit alternative, the calculation of the environmental impacts of the disposal phase was isolated to each retrofit alternative and did not include the disposal impacts of the rest of the building, which is independent of the chosen retrofit alternative. At the end of their lives, each retrofit alternative produces construction and demolition (C&D) waste when they are demolished. In addition, C&D waste is also produced during their installation phase, as a result of processes such as slab demolition, brick wall removal, concrete cover removal, etc. (see Figure 5-6). In this study, the C&D waste generated by the retrofit alternatives is considered to be comprised of only concrete crumble and steel (i.e., other construction materials are such as wood, plastic, metals, glass, etc. is not considered). This consideration is reasonable given that this study focuses on the environmental impacts generated by the retrofit alternatives themselves, which mainly involve reinforced concrete and concrete bricks.

The inventory calculations for the disposal phase were performed using the following approach: first, the energy required to demolish the entire building is calculated based on the global assumptions stated in this section. The ratio between the mass of the materials required by each retrofit alternative and the total mass of the building is used to isolate the demolition energy required by each alternative. The produced C&D waste generated by each retrofit alternative is then transported to an existing landfill facility located 27 km (16.7 miles) from downtown Los Angeles.

5.3.2.5 Inventory Calculation

All LCI data used in this study were site-specific data, based on the recent technologies and normal production conditions mentioned before in this section. The inputs and outputs of each unit process of all the studied retrofit alternatives were calculated and are shown in Table 5.4. The LCA software GaBi [44] was used to calculate the environmental impacts given the inventory inputs and outputs. The life cycle impact assessment was calculated using the TRACI 2.1 [45] impact assessment categories, which are: acidification (AC), ecotoxicity (EC), eutrophication (ET), global warming excluding biogenic carbon (GW-EB), global warming including biogenic carbon (GW-IB), human health particulate air (HHPA), human toxicity cancer (HT-C), human toxicity non-cancer (HT-NC), ozone depletion air (ODA), resources and fossil fuels (R-FF), and smog air (SA).

Table 5.4: Inventory data for each retrofit alternative.

	RC Jacketing	Shear Wall	Beam Weakening
Pre-Installation Phase			
Material Required			
Concrete (kg)	22,434	406,056	-
Steel (kg)	1,954	2,760	-
Bricks (kg)	8,394	-	26,254
Mortar (kg)	387	-	1,786
Installation Phase			
Partial Demolition of Slab			
Energy (kWh)	38.4	76.8	-
Column/Beam Concrete Cover Removal			
Energy (kWh)	38.4	-	57.6
Concrete Cast in Place			
Energy (kWh)	10.5	62.3	-
Slab Reconstruction			
Energy (kWh)	3.5	-	-
Foundation Construction			
Energy (kWh)	-	4.6	-
Disposal Phase			
From Partial Demolition of Slab			
Concrete Waste (kg)	5,670	3,851	-
From Brick Removal			
Brick Waste (kg)	8,394	466,725	26,254
From Column/Beam Concrete Cover Removal			
Concrete Waste (kg)	13,139	-	88,349
From Beam Steel Reinforcement Removal			
Steel Waste (kg)	-	-	3,630
Demolition			
Concrete (kg)	16,764	398,702	-
Steel (kg)	1,954	2,431	-
Energy (kWh)	8,640	16,924	-

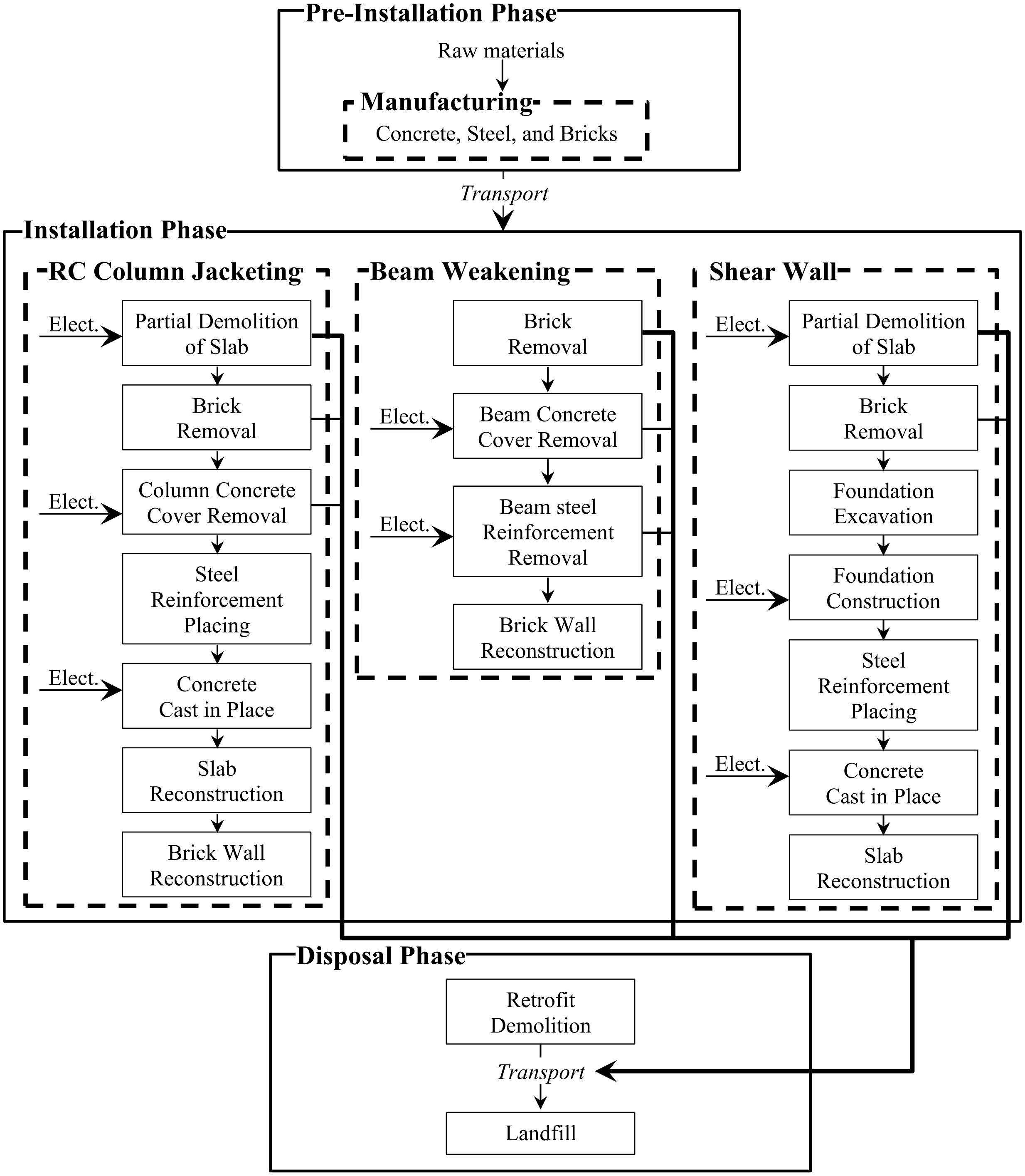

Figure 5-6: Flowchart for the RC Column Jacketing (A), Shear Wall (B) and Beam Weakening (C) alternatives. The assumptions made on each retrofit alternative process are marked with a superscript on the alternative letter.

5.4 Life Cycle Impact Analysis and Interpretation

5.4.1 RC Column Jacketing

Figure 5-7a shows the contributions of each phase to the total environmental impacts of the RC column jacketing retrofit alternative. The results show that the pre-installation and disposal phases accounted for, on average, 64.9% and 34.8% of the total environmental impacts, respectively, while the installation phase contributed to the 0.3% remaining. As shown in Figure 5-7a, the main reason for the high environmental impact of the pre-installation phase was primarily the manufacturing of reinforcing steel for the new columns and the concrete bricks required in the process of wall reconstruction after the columns are jacketed. In general, the manufacturing of the construction materials has a large environmental impact due to the cement's calcination process in the clinker production, fossil fuel usage, and the amount of energy and CO_2 emitted by the steel production. The impacts due to the transportation of the required materials to the building site had an insignificant environmental contribution in the pre-installation phase. It can be easily inferred from the results of the impacts of the disposal phase in Figure 5-7a, which was the second most impactful phase, that the energy required for the demolition of the retrofit and the subsequent disposal of the construction and demolition (C&D) waste on a landfill are the processes that contributed the most to the impacts in this phase. On average, the demolition of the retrofit contributed to 56% and the landfill disposal of the C&D waste contributed to 40% of the total environmental impacts in the disposal phase. Similar to the pre-installation phase, the transportation of the C&D waste to the landfill had an insignificant environmental contribution, representing only 4% of the total environmental impacts on the disposal phase.

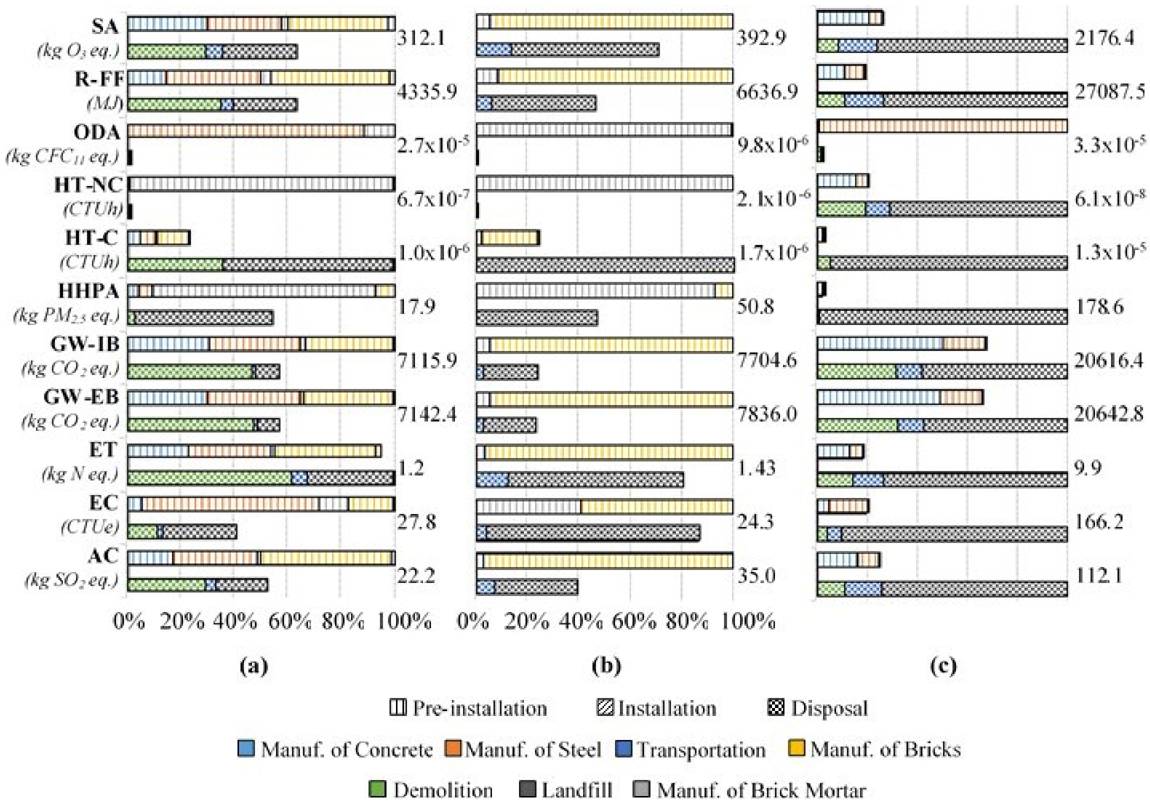

Figure 5-7: Detailed environmental impacts of the (a) RC column jacketing, (b) beam weakening, and (c) shear wall alternative.

5.4.2 Beam Weakening

As shown in Figure 5-7b, the pre-installation and disposal phases accounted for the highest environmental impacts of the beam weakening alternative. On average, the pre-installation phase represented 68.8% and the disposal phase represented 31.1% of the total environmental impacts. Similar to the observed in the RC column jacketing alternative, these phases concentrated the production, demolition, and disposal of the construction materials required by the retrofit alternative. Differently from the other two retrofit alternatives, the beam weakening alternative did not require the production of new reinforced concrete material, only concrete bricks to reconstruct the walls once the beams are sawed. Consequently, in the pre-installation phase impacts shown in Figure 5-7b, the manufacturing of the bricks was responsible, on average, for 66% of the total impacts and the manufacturing of the brick mortar (i.e., cement and sand) was responsible, on average, for 34% of the impacts. Because more bricks are required to be removed along the length of each beam for the sawing process (discussed in Section 4), the impacts for the manufacturing of bricks were even higher than that for the RC column jacketing alternative. On the other hand, similar to the RC column jacketing alternative, transportation of the materials to the building site had an insignificant environmental impact contribution in the pre-installation phase, accounting for less than 1% across all categories. Since the beam weakening alternative performs all of its demolition during the ‘installation’ of the retrofit (i.e., sawing of the beams), there are no demolition impacts related to this alternative once the building is demolished. Consequently, the disposal phase was comprised only of the transportation and landfilling of the C&D waste generated during the installation phase (see Figure 5-7b). The environmental impacts of the landfilling process were responsible to 91%, on average, of the total impacts in this phase while, again, the transportation of the waste to the landfill had a relatively low environmental contribution of, on average, 9% of the total impacts.

5.4.3 Shear Wall

Differently from the previous retrofit alternatives, the disposal phase was the most environmentally impactful phase of the shear wall alternative (see Figure 5-7c). On average, the disposal phase comprised 73.7% of the total environmental impacts, while the pre-installation and installation phases accounted for 26.2% and 0.1%, respectively. The main reason for the high impacts of the disposal phase was the large amounts of reinforced concrete C&D waste that is required to be landfilled. Consequently, as shown in Figure 5-

7c, the landfilling of the C&D waste generated by the demolition of the shear walls represented 72%, on average, of the total environmental impacts while the demolition of the walls contributed to 19%, on average. This result deviates from the conclusions of Vitiello et al. [28], which stated that the pre-installation phase was responsible for 90% of the total environmental impact of the shear wall retrofit alternative. In their study, however, the disposal (i.e., end-of-life) phase was not included. For the pre-installation phase, Figure 5-7c shows that 99%, on average, of the impacts, were a result of the concrete and reinforcing steel manufacturing. Despite significant amounts of material manufacturing required in the pre-installation phase, it is evident that the disposal environmental impacts significantly outweighed the material production impacts, which helps visualize the environmental disadvantage of the use of landfills.

5.4.4 Comparison of All Retrofit Alternatives

When the total impacts of the three retrofit alternatives are compared (see Figure 5-8), the shear wall alternative results in significantly higher environmental impacts than the RC column jacketing and beam weakening alternatives. On average, the shear wall alternative was 3.6 times higher than the RC column jacketing and beam weakening alternatives. The shear wall alternative impacts are considerably higher than the other two alternatives due to the massive amount of reinforced concrete material that is required to build the walls and, subsequently, be disposed of in a landfill. This agrees with the results of Vitiello et al. [28] which, despite comparing the shear wall alternative with three alternatives not analyzed in this study, also concluded that the shear wall alternative was the most environmentally degrading alternative. The RC column jacketing and the beam weakening alternatives resulted in similar total environmental impacts, with, on average, 27.3% and 27.5%, respectively, of the total impacts of the shear wall alternative. The comparison between the RC column jacketing and beam weakening retrofit alternatives revealed that despite the beam weakening alternative not requiring the creation of new members like the other alternatives (e.g., new column sizes in the RC column jacketing alternative, and new shear walls in the shear wall alternative), its environmental impacts were slightly higher than the RC column jacketing alternative. The main reason for these higher impacts was the larger amount of concrete bricks produced in order to reconstruct the walls after the installation is finished. Recall that three rows of bricks were assumed to be removed, throughout the length of the beams, to comfortably fit the sawing tools and human operation in the beam weakening alternative versus one brick from each side of the columns, throughout the height of the floor, in the RC column jacketing alternative.

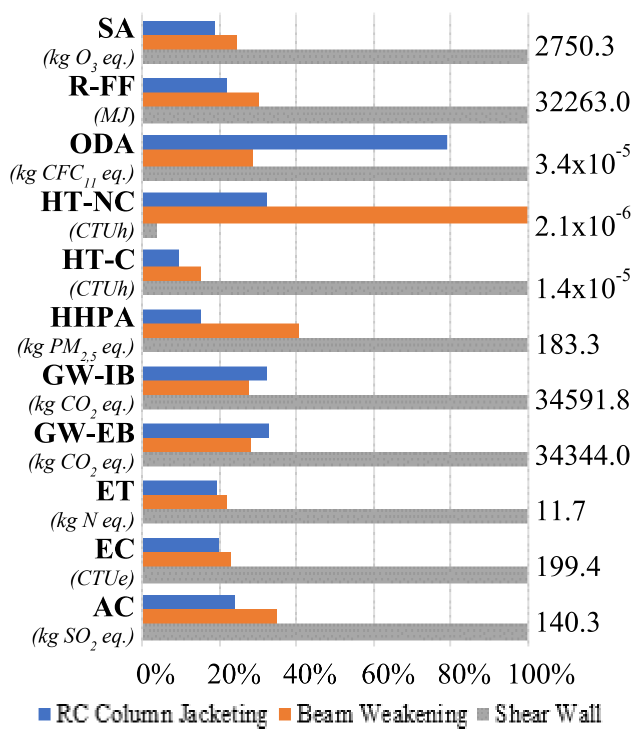

Figure 5-8: Environmental impacts of the three retrofit alternatives.

Amongst the three retrofit alternatives, a trend of three process categories contributed with the majority of the environmental impacts: 1) the manufacturing of the construction materials, 2) the demolition of the retrofit (i.e., except for the beam weakening alternative), and 3) the landfilling of the C&D waste. Together, these three categories comprised the pre-installation (i.e., Category 1) and the disposal phases (Categories 2 and 3), which were shown throughout this section to be the most impactful phases of all the retrofit alternatives. Because the manufacturing of the concrete and reinforcing steel materials in Category 1 are directly tied to the retrofit design of each alternative, it cannot be easily avoided or reduced, without a complete reconsideration of the retrofit alternatives considered. On the other hand, the manufacturing (and consequently disposal) of the concrete bricks is directly related to the type of building considered in this study. In cases where the considered building uses a different wall material (e.g., glass, drywall, etc.), or cases where no walls intersect the retrofitted elements in the moment-resisting frame system, the environmental impacts calculated in this study related to wall demolition and reconstruction could be reduced or avoided. The analysis of building systems that use wall materials other than concrete bricks is out of the scope of this study. However, the environmental impacts of all the processes related to the considered concrete bricked walls can be easily excluded from the performed analysis to illustrate the best-case scenario, where no walls in the moment-resisting frame intersect the retrofitted elements. Under this condition, the reduction in total environmental impacts would be approximately 35%, 75% and 32% for the RC column jacketing, beam weakening, and shear wall alternatives, respectively (see Figure 5-9). In this scenario, the shear wall would continue to be the most environmentally degrading alternative; the beam weakening impacts, on the other hand, would be considerably lower, which would grant this alternative the position of least environmentally degrading of all the three studied alternatives, with 40% less impacts, on average, than the RC column jacketing.

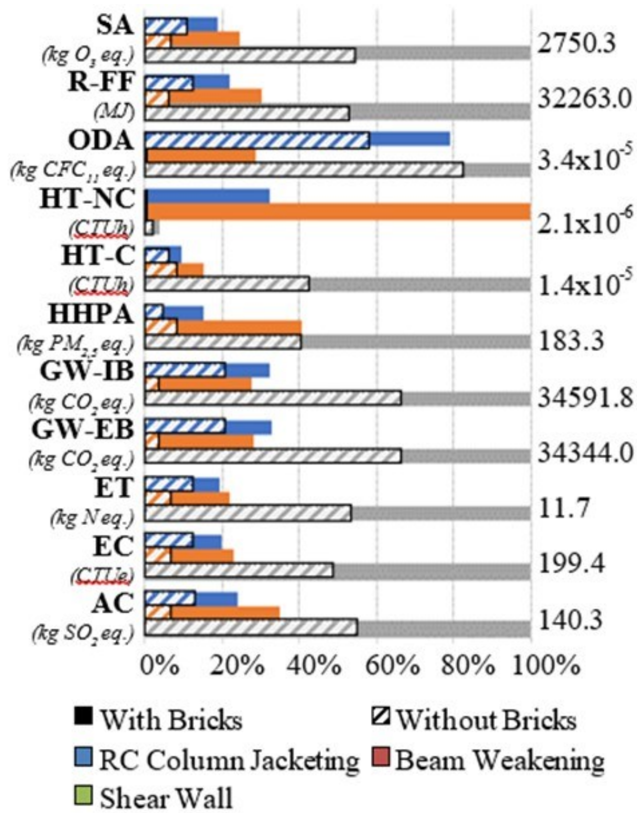

Figure 5-9: Environmental impacts of the three retrofit alternatives with and without concrete bricked walls.

The demolition of the retrofits in Category 2 is also linked to the assumptions made in Section 2 regarding the machinery involved in the demolition process, which the authors believe is representative of current practices. Additional studies could be performed to evaluate the impacts using faster and more efficient demolition techniques such as demolition by explosions, which is out of the scope of this study. Finally, an alternative for the impacts generated by the Category 3 processes would be directing the C&D waste to reinforced concrete recycling plants in order to lower the environmental impacts caused by the use of landfills. In the next section, the recycling of the C&D waste is considered and the LCA results are compared as an alternative to landfill disposal.

5.4.5 Recycling

The C&D waste generated by each retrofit alternative was considered to be disposed of in a landfill facility, which resulted in one of the process categories with higher environmental impacts across all alternatives. In this section, the recycling of the generated C&D waste is incorporated in the analysis in order to quantify its environmental benefits when compared to landfilling. Consequently, a new LCA was performed in which the C&D waste was sent to a reinforced concrete recycling facility to be further processed and become recycled concrete aggregate and recycled steel. These recycled materials can then be used in a variety of future applications such as new concrete production, new reinforcing bars, concrete for pavement, asphalt base layer, etc., replacing the need for the extraction of virgin raw material.

In general, the recycling processes of building's C&D waste (i.e., primarily reinforced concrete crumble) starts with the break of the concrete waste into smaller blocks by an excavator machine. Then, the collected concrete waste is put into a crushing equipment and, through a two-phase crushing process provided by a jaw crusher and a hammer crusher, the concrete waste is produced into recycled concrete aggregate (RCA). During the same time, the rebar and metal connector contained in the concrete waste can be separated by a magnetic separator and shipped to a steel mill, where it will be part of the production of new steel and used in various applications (including new reinforcing bars). Lastly, the reinforced concrete aggregate goes through sieving technologies to produce different particle sizes [46–48].

The recycling of reinforced concrete C&D waste into RCA is not 100% efficient in the sense that 1kg of C&D waste does not produce 1kg of RCA. Previous studies have reported that, in general, the recovery percentage of recycled concrete is about 60% of input C&D waste, while the rest (i.e., 40%) are fine particles produced as a result of the recycling processes [46,49]. These fine particles are generally not recommended to be used as RCA [49] and are usually disposed of in a landfill. Reinforcing steel, on the other hand, can be fully utilized as recycled scrap metal to be used in the production of good quality steel bars with roughly the same characteristics as virgin steel [50]. A case study of a building demolition in Italy identified that 70% of the steel waste was immediately recovered at the worksite after demolition, while the other 30% was recovered as a result of the magnetic separation process in the reinforced concrete recycling plant [50].

Based on the information presented in this section, the disposal phase LCA of each retrofit alternative was modified to include the environmental impacts of the recycling operations using the following approach: the reinforced concrete C&D waste generated by each alternative (i.e., including the concrete bricks) is transported to the recycling plant, where 60% becomes RCA and 40% becomes fine particles, which are sent to landfilling (the recycling plant and landfill are 13 miles apart). Similarly, 70% of the steel waste is assumed to be immediately recovered at the worksite and transported to a steel mill plant that accepts recycled scrap metal located 16 miles from downtown Los Angeles. The remaining 30% of the steel waste is assumed to be recovered during the recycling of the reinforcing concrete and subsequently shipped to the steel mill (the recycling plant and steel mill are 16 miles apart). The environmental impacts associated with the recycling of the C&D waste are calculated using the LCI data per kg of recycled material provided in [49].

Figure 5-10a, 10b, and 10c show the impacts of the recycling the C&D waste of each retrofit alternative as a ratio of the impacts originally calculated considering landfilling. The results indicate that the beam weakening and the shear wall alternatives benefit the most from recycling, with a reduction of, on average, 53% and 52% in the disposal phase environmental impacts. On the other hand, the reduction in the disposal impacts of the RC column jacketing alternative reaches, on average, 29%. The reduction in total environmental impacts for each alternative is shown in Figure 5-10d where, on average, the impact reductions were 12%, 16%, and 42% for the RC column jacketing, beam weakening, and shear wall alternatives. Despite the beam weakening and shear column alternatives presenting similar ratios of impact reduction due to the recycling of the C&D waste, the reduction in total environmental impacts of the shear wall alternative was significantly higher than the beam weakening alternative (see Figure 5-10d). This occurred because the environmental impacts of the disposal phase of the shear wall alternative were significantly higher (i.e., due to the large volume of C&D waste generated by the demolition of the walls) than the impacts of the beam weakening alternative, which led the same percentage reduction to result in considerably higher impact reduction. Regardless of the significant reduction in total environmental impacts, the shear wall alternative remained two to three times more environmentally degrading than the RC column jacketing and beam weakening alternatives. The results indicated that the recycling of the C&D waste can reduce the environmental impacts of the disposal phase in, on average, 45% for all the retrofit alternatives studied; however, unless the disposal phase accounts for a significant part of the impacts across all phases (e.g., the shear wall alternative), the reduction in the total environmental impacts introduced by recycling can be significantly lower. Finally, a quick comparison with Figure 5-9 reveals that the removal of the environmental impacts related to the concrete bricked walls from the analysis (i.e., simulating a scenario where the retrofit alternatives are performed on a building where no walls intersect the retrofitted elements) resulted in an higher total environmental benefit than the recycling of the C&D waste (i.e., 47% reduction versus 23% reduction due to removal of bricked walls and recycling, respectively).

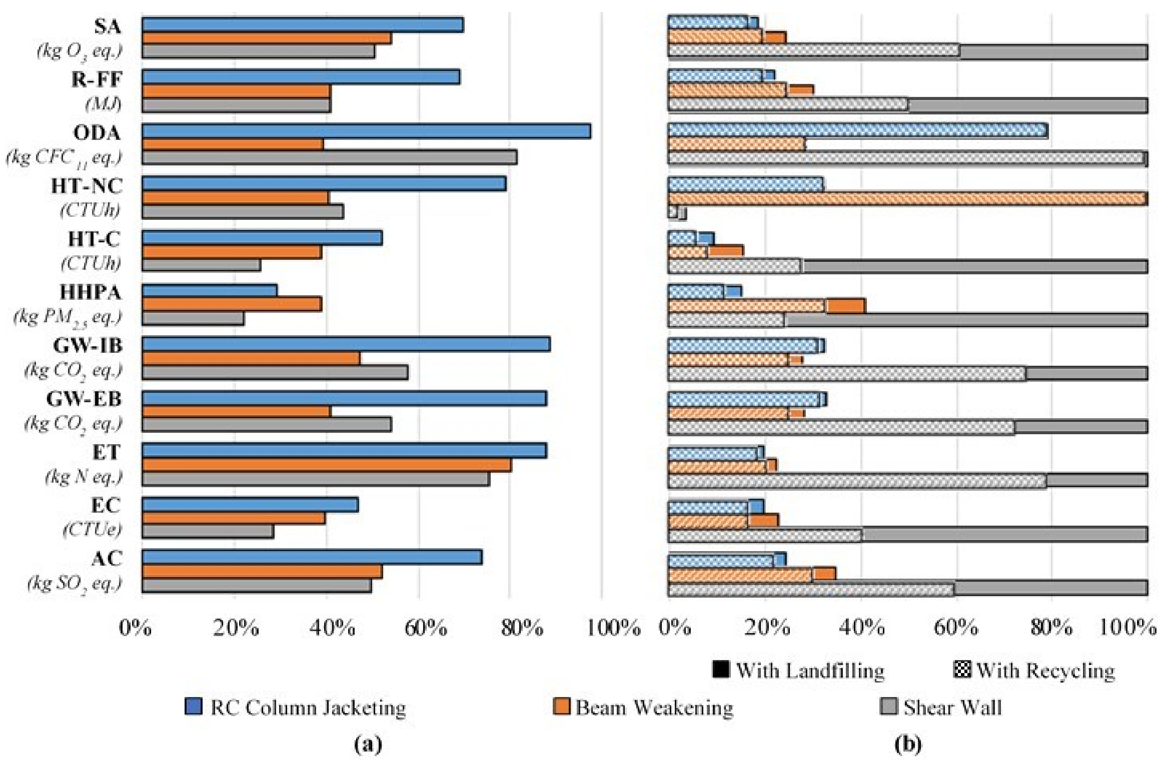

Figure 5-10: a) Recycle / landfill ratio of environmental impacts for the disposal phase of each retrofit alternative and b) total environmental impact comparison with and without consideration of recycling.

5.5 Conclusions

This study performed a life cycle assessment of three seismic retrofit alternatives of an eight-story seismically deficient reinforced concrete frame structure. The retrofitted alternatives were as follows: RC column jacketing, beam weakening, and shear wall addition alternatives. The retrofit designs were performed in the literature to provide compliance with the collapse prevention limit state. The study presented a detailed description of the cradle-to-grave processes considered, and relevant assumptions, for each retrofit alternative. Two distinct disposal, or end-of-life scenarios, were assessed for the construction and demolition (C&D) waste generated by each retrofit alternative: landfilling and recycling.

The shear wall alternative had the highest environmental impact amongst the three alternatives, where the disposal to a landfill was the most environmentally degrading phase, accounting for, on average, 73.7% of the total impacts. This occurred due to a large amount of C&D waste comprised of reinforced concrete and bricks that were required to be landfilled. Similarly, the pre-installation phase accounted for 26.2% of the total impacts due to the manufacturing of large quantities of concrete and steel reinforcement. The RC column jacketing and the beam weakening alternatives resulted in similar total environmental impacts, with, on average, 27.3% and 27.5%, respectively, of the total impacts of the shear wall alternative. Despite the beam weakening alternative not requiring the creation of new reinforced concrete elements like the other alternatives (e.g., new column sizes in the RC column jacketing alternative, and new shear walls in the shear wall alternative), its environmental impacts were slightly higher than the RC column jacketing alternative due to the larger amount (i.e., in comparison to the RC column jacketing alternative) of concrete bricks required to be produced in order to reconstruct the walls after the installation is finished. As a general trend amongst all the investigated retrofit alternatives, the environmental impacts associated with the processes required for the installation of each alternative and the transportation of the materials (i.e., from manufacturing site to building site, or from the building site to disposal) were negligible in comparison with the pre-installation and disposal phases impacts.

The magnitude of the impacts related to the used concrete bricks was investigated by removing all the impacts associated with them (i.e., as if no walls in the building intersected the retrofitted elements), and concluded that approximately 35%, 75%, and 32% of the total environmental impacts could be reduced for the RC column jacketing, beam weakening, and shear wall alternatives, respectively. This study also investigated the change in environmental impacts of all the alternatives when recycling, instead of landfilling, of the generated C&D waste is performed. It was observed that recycling reduced the environmental impacts of the disposal phase between 29% and 53% amongst the retrofit alternatives. The beam weakening and shear wall alternatives were the alternatives that benefited the most from the recycling, with 53% and 52% impact reduction in the disposal phase. When assessing the difference in total environmental impact due to the recycling consideration, the impact reductions were more modest, ranging from 12% to 42% amongst the retrofit alternatives. This reduction was lower than the reduction provided by the removal of the concrete bricked walls from the analysis. Despite the shear wall and beam weakening alternatives presenting the same impact reduction rate in the disposal phase, the shear wall alternative presented considerably higher total environmental reduction than the beam weakening alternative (i.e., 42% versus 16%, respectively) due to recycling. This occurred because the environmental impact of the disposal phase of the shear wall alternative was significantly higher than the disposal phase of the beam weakening alternative. Thus, the recycling effects on the total environmental impacts were more pronounced for the alternatives with high disposal phase environmental impact.

Chapter 6

Journal Paper V - A Resilience-Based Environmental Impact Assessment Framework for Natural Hazard Loads[5]

6.1 Abstract

Urban centres are moving toward sustainable communities while seeking eco-friendlier building alternatives. For communities in natural hazard-prone regions, the structural performance and environmental impacts of eco-friendlier building alternatives should be mutually considered and compared with those of existing solutions adoption. The performance-based engineering and life cycle assessment methodologies are powerful tools to achieve both objectives. However, these methods are fundamentally uncoupled, which raises the following question: Will the environmental benefits come at the expense of structural resilience? The objective of this study is to take the first step in creating a multidisciplinary framework that combines performance-based engineering with life cycle assessment to quantify and compare the structural resilience-based environmental impacts of different building alternatives. The framework provides a powerful means for making science-based decisions when considering newer and seemingly more sustainable building

[5] Manuscript submitted to and under review in Structure and Infrastructure Engineering, Rafael A. Salgado & Serhan Guner, A Resilience-Based Environmental Impact Assessment Framework for Natural Hazard Loads, © 2020, with permission from Taylor & Francis Online. For the published version, please refer to https://www.utoledo.edu/engineering/faculty/serhan-guner/publications.html.

configurations while accounting for their structural resilience to natural hazard loads. For demonstration purposes, the framework is applied to two seven-story building configurations made from cross laminated timber and reinforced concrete materials in a tsunami-prone region. The outcome of the methodology is a normalized quantitative comparison of the environmental impacts that can help decision makers in selecting a suitable building configuration for structural resilience to natural hazard loads.

6.2 Introduction

The use of conventional building materials such as steel, masonry, and concrete has made the construction industry responsible for a considerable environmental impact across the globe in the form of nonrenewable resource depletion, waste generation, energy consumption, and CO_2 emissions [1–3]. Consequently, urban centers have been moving towards sustainable communities while seeking eco-friendlier building configurations (i.e., its materials and structural system). For communities in natural hazard-prone regions, it is important to ensure that this move does not come at the expense of structural resilience. To better assess the feasibility of the adoption of eco-friendlier building configurations, their structural resilience and environmental impacts should be mutually considered and compared with those of existing solutions.

Performance-based engineering (PBE) is a powerful methodology that allows quantifying the structural performance of a building to achieve a desired structural resilience to natural hazard loads. The nonlinear structural analysis method is the primary ingredient of PBE for accurately quantifying the inelastic response that most buildings undergo during natural hazard loads [4,5]. This methodology, however, does not take into account the environmental impacts of the building configurations considered. A life cycle assessment (LCA) analysis, on the other hand, is commonly undertaken to quantify the environmental impacts of building configurations [6,7] with no consideration of their structural resilience. Using these two uncoupled methods leaves the following question unanswered: Will the environmental benefits come at the expense of structural resilience?

The objective of this study is to take the first step in creating a multidisciplinary framework that combines PBE with LCA to quantify and compare the structural resilience-based environmental impacts of different building configurations. The framework aims to provide a powerful means for making science-based decisions when considering newer and seemingly more sustainable building configurations while accounting for their structural resilience to natural hazard loads. For demonstration purposes, the framework is applied to compare two seven-story building configurations made from cross laminated timber and reinforced concrete materials in a tsunami-prone region. The outcome of the methodology is a normalized quantitative comparison of environmental impacts that can help decision makers in selecting a suitable building configuration for structural resilience to natural hazard loads.

6.3 Structural Resilience-Based Environmental Impact Assessment Framework

An overview of the framework is shown in Figure 6-1. As part of the performance-based engineering (PBE) methodology, nonlinear computational modeling methods are employed in two concurrent processes. In Process 1, the building configurations are subjected to the expected natural hazard loads to simulate their responses including structural deformations, damage and cracking behavior, and the failure mode, in a way analogous to physically testing a prototype building in laboratory settings. To characterize their full response from the initial-elastic to the near-collapse nonlinear stages, each building configuration is subjected to a series of natural hazard loads of increasing magnitudes. The predicted structural response at each natural hazard load level has a direct impact on the subsequent LCA analysis in the form of the environmental impacts associated with the building retrofits required by the natural hazard-induced damage. In Process 2, the thresholds for the expected damage levels are determined for the building configurations. These thresholds characterize performance limit states that are used to classify the structural resilience to natural hazard loads of each building configuration. Before the structural resilience-based environmental assessment is achieved, the performance limit states of each building configuration are normalized using Performance Normalization Factors (PNF). Finally, the outcomes of Processes 1 and 2 are combined to provide a normalized quantitative comparison of the environmental impacts versus the structural resilience of the two building configurations.

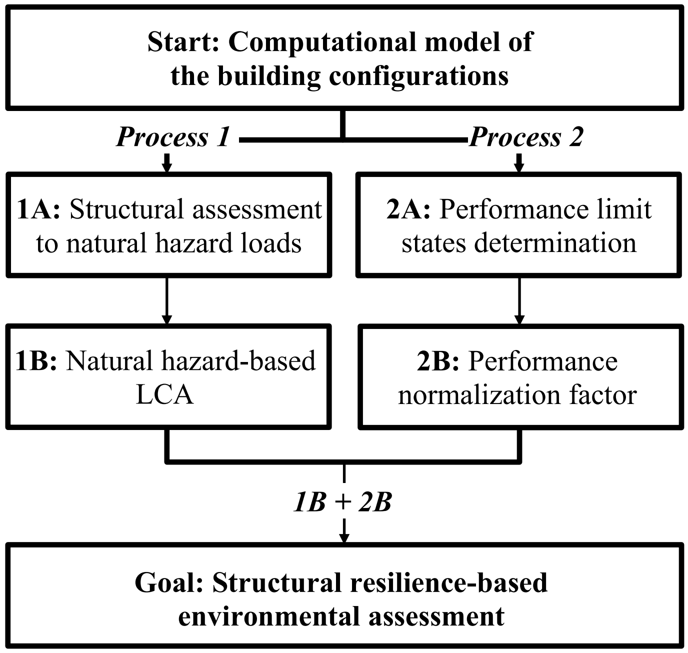

Figure 6-1: Multidisciplinary framework for the combined structural and environmental assessment of buildings.

6.3.1 Start: Computational Model of the Building Configurations

The proposed framework relies on the accurate characterization of the buildings' responses to predict their performance and damage characteristics. Under natural hazard loads, structures are often subjected to stress levels that go well beyond the material's elastic limit, causing residual damage and nonlinear deformations. To capture this behavior and obtain reliable results, computational models in the form of nonlinear finite element models combined with state-of-the-art material model formulations should be employed for the structural system and material of the building configuration investigated (e.g., reinforced concrete moment frames, wood shear wall systems, etc.).

The choice of the finite element model type for a given application requires a fine balance between accuracy, practicality, and computational efficiency, subject to the capabilities of available software and computational resources [8]. For the most accurate results, it is recommended that the building configurations be modeled and analyzed using 3D approaches, which is also the most complex and computationally demanding approach. Depending on the combination of natural hazard and structural system being considered, the main load-resisting mechanisms of the system may allow for the use of modeling strategies that reduces computational costs without compromising the calculated accuracy. For instance, in moment frame building configurations (i.e., beams and columns), lateral loads caused by tsunami hazards are mainly resisted by the frames in the direction of the load. If the building is regular (i.e., box-shaped with no stepped elevations), it is common to analyze only one of the building's bays and reasonably assume the same response for the remaining identical bays (e.g., [31,32]). Thus, for this combination of natural hazard and building configuration, a 2D modeling approach can be used. On the other hand, in panelized building configurations, where the interactions between in- and out-of-plane wall panels are the main load-resisting mechanism, a 3D modeling approach should be used.

The foundation of the building is included in the model if the building-foundation interaction is expected to significantly influence the building's response. Similarly, depending on the natural hazard being considered (e.g., earthquakes), the foundation-soil interaction may significantly influence the building's response and, therefore, should be included in the computational model. The boundary conditions are specified as realistically as possible for all the elements of the building, including the foundation and soil, if considered.

6.3.2 Process 1A: Structural Assessment to Natural Hazard Loads

Similar to the computational building models, adequate characterization of the natural hazard load is essential to predict accurate building performance and damage.

Natural hazard loads are usually applied suddenly over a short period of time (e.g., windstorm, earthquake, tsunami, etc.), which make them dynamic (i.e., time-dependent) in nature. Nonlinear time-history analysis is the most realistic approach to modeling natural hazard loads because it accurately imposes time-dependent load behaviors such as rate-dependent effects and path-dependent cyclic loads on the computational building models [8]. Nonlinear time-history analysis, however, is a computationally demanding procedure that can take significant time to complete depending on the natural hazard, computational building model, and computational resources (e.g., 2 days to perform a complete seismic time-history analysis of a 7-story 3D building model on an average office computer). Nonlinear static analysis – where the load application time is not considered – offers a much simpler alternative to nonlinear time-history analysis. Although structural responses will not be as accurate, this procedure can be used when there are limited computational resources and sufficient literature evidence that demonstrate its applicability and its limitations to nonlinear time-history analyses.

To characterize the full response of the building configurations from their initial-elastic to the near-collapse-nonlinear stages, each computational model is subjected to a series of natural hazard loads starting at reasonably low values (e.g., 0.5 m tsunami inundation depth, 0.05g earthquake peak ground acceleration, etc.) and increasing in magnitude at reasonable steps until the building collapses.

6.3.3 Process 1B: Natural Hazard-Based Life Cycle Assessment (LCA)

The LCA analysis is used to evaluate the environmental impacts of each building configuration over its lifespan. The calculated structural resilience of the building has a direct impact on the LCA analysis, as shown in Figure 6-2. If no natural hazard occurs, the building operates normally until the end of its lifespan, when it is demolished, and its materials are sent to recycling. If a natural hazard occurs, the building's structural resilience determines the endured damage level (which may include building collapse), and the appropriate post-disaster retrofit measures are performed.

The LCA analysis is based on the ISO 14040 [6] and ISO 14044 [7] guidelines and constitutes a cradle-to-grave analysis subdividing the environmental impacts into five distinct LCA phases: material manufacturing, building construction, retrofit, demolition, and material recycling, as shown in Figure 6-2. The use phase of the LCA analysis can be omitted if there is sufficient literature evidence that demonstrates similar environmental impacts in this phase for the different building configurations considered. In addition, the impacts of this phase are usually not significant when the damage and retrofit impacts are assessed in separate phases [9], as is the case in this study.

The material manufacturing and construction phases group the main operations required to erect the building, including the shipping of the essential materials. These phases are also considered when the building collapses due to the natural hazard loads to account for its reconstruction. The retrofit phase groups the post-disaster operations required to restore any non-collapsible damage. The demolition phase groups the operations performed to demolish or disassemble the building at the end of its lifespan. This phase (or a variation of it) is also considered when the building collapses to account for post-disaster operations performed on collapsed structures such as the demolition of any remaining sections, gathering of debris, site cleaning, etc. Recycling is considered when the building is demolished at the end of its lifespan and when the building collapses. In the second case, a reduced recycling ratio is considered to reflect material losses (e.g., damage beyond repair, material carried away by the waves/wind, etc.) that might occur due to the collapse of the building.

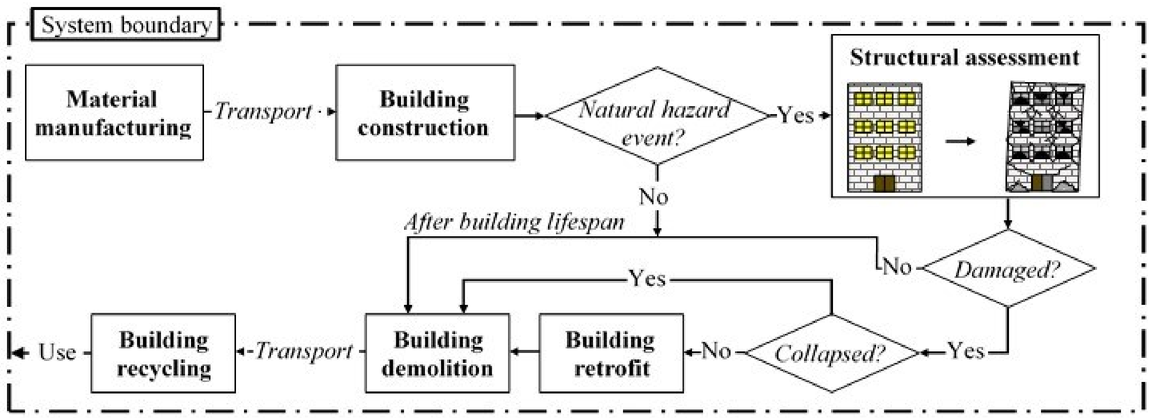

Figure 6-2: System boundary and LCA phases considered.

The functional unit of an LCA is essential for the effective comparison of the environmental impacts of the building configurations and is defined based on key properties that are common for the different building configurations considered (e.g., total floor area, number of stories, performance criteria used during design, etc.). Six impact categories are considered, following the recommendations in FEMA P-58 [9], for the environmental assessment of buildings subjected to natural hazard loads: global warming potential (GWP) including and excluding CO_2 sequestration by wood products, acidification (AC) potential, eutrophication (ET) potential, ozone depletion in the air (ODA), and smog air (SA) potential.

6.3.4 Process 2A: Performance Limit States Determination

A crucial step in the performance-based engineering (PBE) methodology is the determination of the different performance limit states that define thresholds for the expected damage levels of the building configurations. This set of performance limit states should be established for the building configurations considered to enable the assessment and comparison of their structural resilience. This study employs a set of four performance limit states commonly used to characterize building's performances and recommended in modern performance-based guidelines [4,10]: operational (OP), immediate occupancy (IO), life safety (LS), and collapse prevention (CP). As shown in Figure 6-3, the OP indicates the state at which the structure has suffered no damage and requires no evacuation during the natural hazard; the IO indicates the state at which the structure retains its pre-natural hazard strength and stiffness, and can be re-occupied immediately; the LS indicates the state at which the structure has some damaged components but is safe against the onset of a partial or total collapse; and the CP indicates the state at which the structure has suffered major damage, without complete collapse, and requires a complete demolition [10].

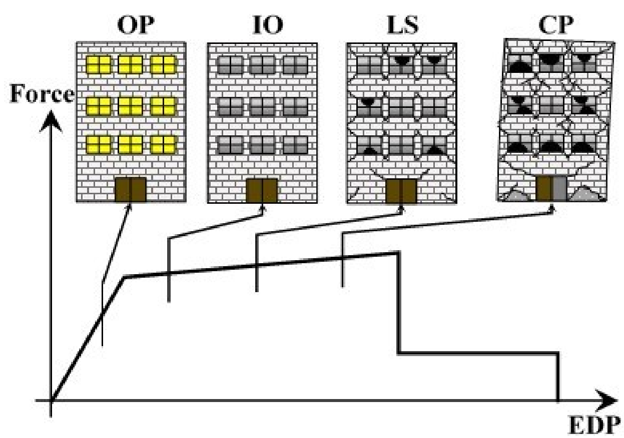

Figure 6-3: Performance limit states based on structural load-deflection response.

These performance limit states are defined based on the structural response parameters such as interstory drift ratios, deformations, or individual element rotations, called engineering demand parameters (EDP). To define the EDPs that correspond to each performance limit state, the computational model of each building is subjected to fictional loads that aim to primarily engage their main load-resisting mechanism for the natural hazard considered. These loads are applied in a displacement-controlled mode in order to capture the post-peak responses of each building configuration. If the main load-resisting mechanism of the building configuration investigated involves complex structural interactions that are not easily representable by displacement-type fictitious loads, the results calculated in Process 1A can be used to define the performance limit states (an example is discussed in the case study section of this study).

6.3.5 Process 2B: Performance Normalization Factor

One of the fundamental aspects of comparative LCA is that the two alternatives compared should be equivalent. Building codes provide the minimum requirements for the design different building configurations. Consequently, different building configurations designed to resist the same natural hazard load as per the applicable codes can actually respond significantly different if the buildings were physically tested or numerically analyzed using nonlinear computational models. Because the computational demand and time required to perform nonlinear numerical analyses are significantly high, it would not be feasible to attempt to match the performance of the different building configurations by iteratively adjusting their computational building models and re-analyzing them. To overcome this limitation, a factor called the Performance Normalization Factor (PNF) is developed to allow the direct quantitative comparison of the performance limit states of each building configuration, as shown in Figure 6-4. To calculate the PNF, one of the investigated building configurations is treated as the reference building (e.g., building 2 in Figure 6-4). For all other building configurations considered (only two are considered in Figure 6-4, but more could be added), Equation 1 is used to calculate the PNF for each performance limit state, which accounts for the calculated force and EDP differences between the considered building configurations and the reference building.

$$PNF_i = \sqrt{\left(\frac{edp_{bj_i}}{edp_{bref_i}}\right)^2 + \left(\frac{F_{bj_i}}{F_{bref_i}}\right)^2} \tag{1}$$

where PNFi is the performance normalization factor for performance limit state i, b_j is building j, b_{ref} is the reference building, and the F_{bji} is the force for building j. Figure 6-4 shows the visual representation of the PNF where i equals CP, j equals building 1, and ref equals building 2.

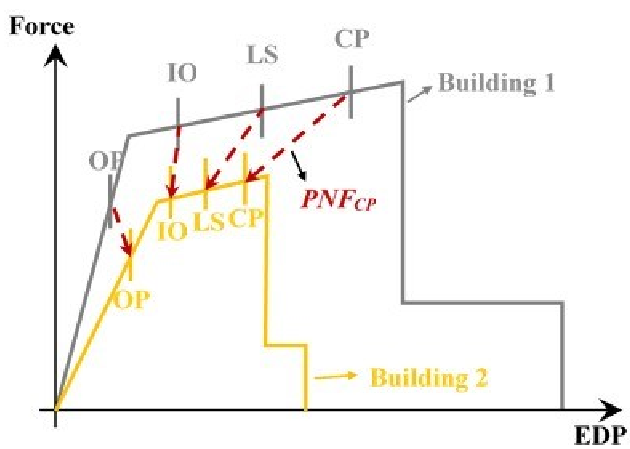

Figure 6-4: Performance comparison and normalization factors.

6.3.6 Goal: Structural Resilience-Based Environmental Assessment

To perform the structural resilience-based environmental assessment of the different building configurations, the environmental impacts of the non-reference buildings are divided by their calculated PNFs for each performance limit state. This ensures that their environmental impacts are normalized to the same structural performance of the reference building (e.g., building 2 in Figure 6-4), which allows for the normalized quantitative comparison of the environmental impacts versus the structural resilience of the different building configurations considered.

6.4 Case Study: Cross Laminated Timber and Reinforced Concrete

For demonstration purposes, the proposed framework is employed to investigate and compare the structural resilience-based environmental impacts of a building made of cross laminated timber (CLT) and traditional reinforced concrete (RC) materials in a tsunami-prone region. While this case study focuses on the structural resilience to tsunami loads, which is a relatively unexplored research area compared to seismic or windstorm loads, the framework could also be applied to other natural hazard loads.

CLT is a relatively new material that has been increasingly investigated as a possible alternative to traditional building materials, especially for mid-rise buildings (i.e., between four and eleven stories). It is prefabricated engineered wood panels made of orthogonally bonded layers of solid-sawn lumber that are laminated by gluing longitudinal and transverse layers. CLT panels are used as load-bearing walls, floors, and roofs that are connected using metal connectors (e.g., angle brackets and hold-downs) and steel fasteners (e.g., nails, screws, or bolts). CLT has environmental advantages compared to steel, masonry, and concrete with respect to embodied CO_2, ozone depletion, and global warming potential [11–14]. In addition, CLT panels act as a carbon sink and require less energy to produce than concrete and steel. Regarding its structural resilience to natural hazard loads, CLT has been primarily investigated under seismic load conditions – where it has exhibited a good performance [15–24] – whereas, more recently, studies are investigating its response to tsunami load conditions (e.g., [25,26]).

6.4.1 The Buildings

The seven-story CLT building has been constructed as part of a study to evaluate the earthquake performance of multi-story CLT buildings [27] whereas the RC building has been designed for this study. The CLT building was designed following Eurocode 8 [28] guidelines to resist the peak ground accelerations of the Kobe JMA earthquake, one of the most devastating earthquakes of the past decades. To create an equivalent design for the CLT building, the RC building followed the same design guidelines and load intensities. The structures are considered to be located in Blaine, Washington (i.e., a highly seismic tsunami-prone region) to allow the use of the new tsunami chapter of ASCE 7 [29] to perform the tsunami analysis, which is based on mapped inundation depths of the United States.

6.4.1.1 CLT building

The CLT building is shown in Figure 6-5. Spruce CLT panels are used for the walls, floors, and roof slabs. Due to different structural needs, several CLT wall thicknesses are used on different stories. Self-drilling screws are used to connect floor slabs to CLT walls and adjacent wall/slab panels. In addition, angle brackets and hold-downs are used to connect the wall panels to the slabs and the foundation (see Figure 6-5a for the distribution of the connections on the first floor of the building). More details on the CLT building can be found at [27].

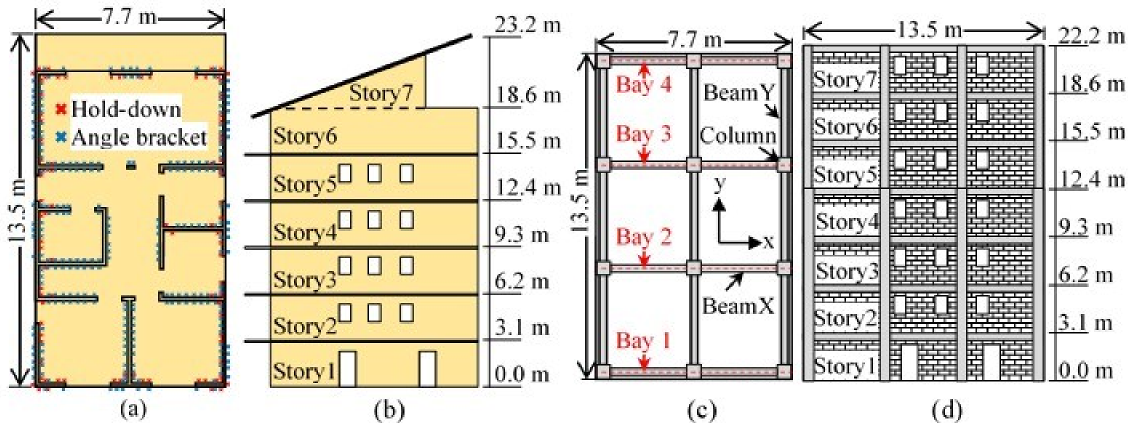

Figure 6-5: Plan and elevation views of the seven-story (a)-(b) CLT [27] and (c)-(d) RC buildings.

6.4.1.2 RC building

The RC moment frame building is shown in Figure 6-5 and the design characteristics of the beams and columns for each story of the building are shown in Table 6.1. Masonry infill walls are used to provide enclosure to the outer shell of the building while the interior walls are made of non-structural elements such as drywall or light steel framing.

Table 6.1: Design details of the RC building.

Story	**Column**			**Beams**			
					Long. Reinf.		**Transv. Reinf.**
	Dimens. (m x m)	**Long. Reinf**	**Transv. Reinf.**	**Dimens. (m x m)**	**BeamX**	**BeamY**	
1	0.6 x 0.6	12-#11	3-#4@125 mm	0.4 x 0.3	6-#10	6-#11	2-#4@220 mm
2	0.6 x 0.6	8-#10	2-#4@125 mm	0.4 x 0.3	6-#10	6-#11	2-#4@220 mm
3	0.6 x 0.6	8-#10	2-#4@125 mm	0.4 x 0.3	6-#10	6-#11	2-#4@220 mm
4	0.6 x 0.6	8-#10	2-#4@125 mm	0.4 x 0.3	6-#10	6-#11	2-#4@220 mm
5	0.5 x 0.5	8-#10	2-#4@180 mm	0.4 x 0.3	4-#10	4-#11	2-#4@300 mm
6	0.5 x 0.5	8-#10	2-#4@180 mm	0.4 x 0.3	4-#10	4-#11	2-#4@300 mm
7	0.5 x 0.5	8-#10	2-#4@180 mm	0.4 x 0.3	4-#10	4-#11	2-#4@300 mm

6.4.2 Start: Computational Models of the Building Configurations

6.4.2.1 CLT building

The CLT building computational model is created using the computer program Abaqus/Standard [30]. The details of the model described in this section have been experimentally validated in [25,26]. The CLT panels are modeled using 4-node, 6-degree-of-freedom shell elements as shown in Figure 6-6a. A composite layup approach is used with the shell elements to account for the orthogonal material directions of each layer of the panels, as shown in Figure 6-6b. The wood constitutive response is characterized as orthotropic elastic with brittle failure for both tension and compression, as shown in Figure 6-6c.

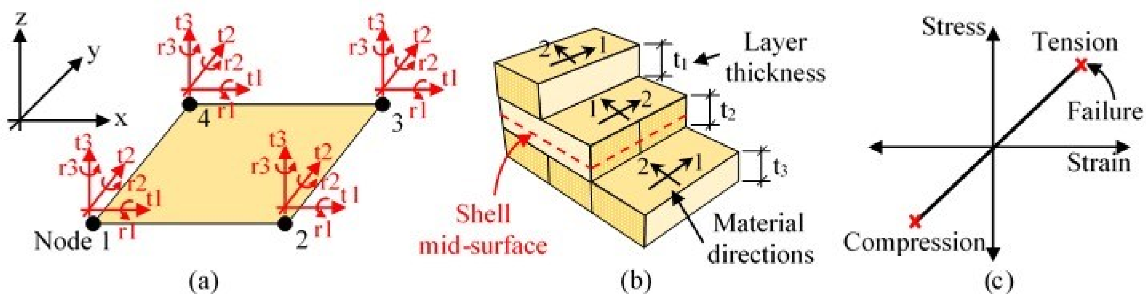

Figure 6-6: (a) Shell element, its (b) composite layup, and (c) wood constitutive response.

The panel connections are modeled using 2-node, 3-degree-of-freedom connector elements (i.e., springs), as shown in Figure 6-7a. The connector element responses are modeled using three uncoupled constitutive models (i.e., one for each degree-of-freedom) to simulate the axial, in-plane, and out-of-plane responses of the panel connections, as shown in Figure 6-7b to Figure 6-7d. The axial and in-plane responses of panel connections are well known in the literature; in this study, these behaviors are modeled as per the results of [31,32]. An accurate simulation of the out-of-plane responses of panel connections is critical for simulations of CLT buildings due to their panelized tsunami load-resisting mechanism discussed in Section 2.1. However, the out-of-plane response of panel connections has received little attention in the literature and studies have only recently started to characterize their response in two distinct out-of-plane directions, termed the out-of-plane interior (OPI) and exterior (OPE) responses [25], as shown in Figure 6-7d. In this study, the behavior of the connector elements in the out-of-plane direction is modeled as per the results of [25,26].

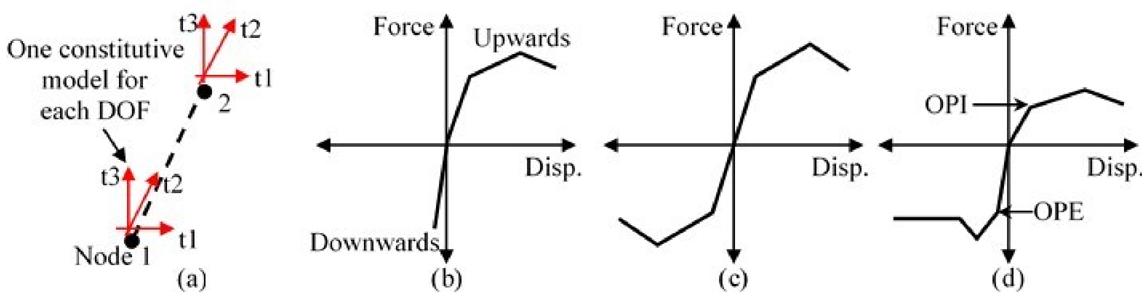

Figure 6-7: (a) Connector element, (b) axial, (c) in-plane, and (d) out-of-plane responses.

In addition to the connections on each floor, a surface-to-surface discretization method is used to define the mechanical contact interaction between the wall and slab panels or steel foundation. The behavior of each contacted interface is characterized in both the normal and tangential directions. The normal direction is dictated by a hard contact algorithm while the tangential behavior is dictated by a friction contact algorithm with a friction coefficient of 0.15. The door and window openings on the afflicted side are removed from the model, as shown in Figure 6-8a, to allow the tsunami to fully engage the building. The boundary conditions are modeled with a fixed rigid plane that represents the building foundation.

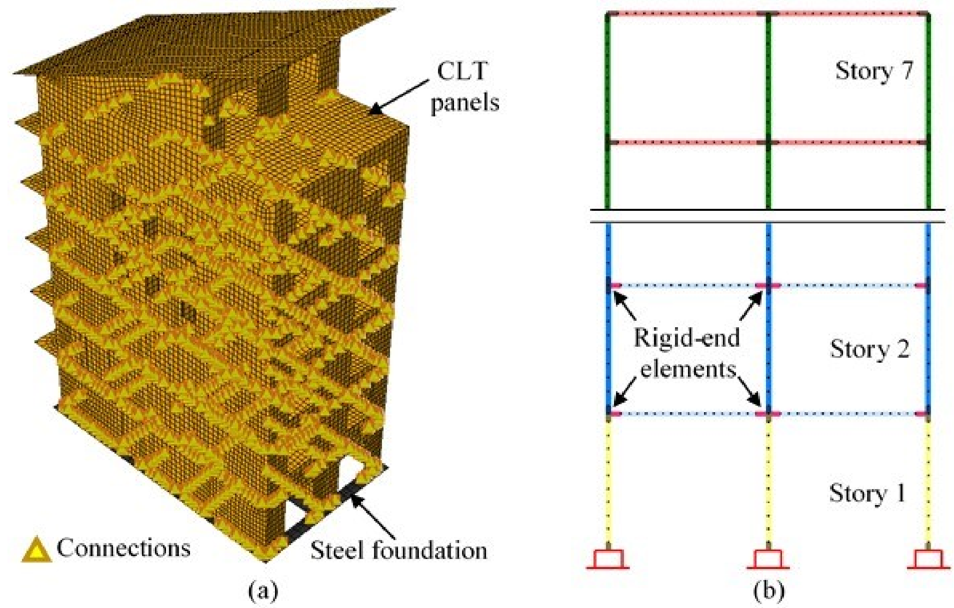

Figure 6-8: Created seven-story (a) CLT and (b) RC buildings computational models.

6.4.2.2 RC building

The RC building considered in this study is a regular structure, which allows for a 2D modeling approach with the frame element developed by Guner and Vecchio [33,34]. This element is based on the Modified Compression Field [35] and the Disturbed Stress Field [36] theories, which captures the coupled flexure, axial, and shear interaction effects. A smeared, rotating crack approach based on a total load, secant stiffness formulation is employed, and the triaxial concrete core confinement is inherently accounted for using in- and out-of-plane reinforcement ratios. In addition, the element incorporates several second-order material behaviors specifically developed for RC structures. The model is created using the computer program VecTor5 [37]. The details of the model described in this section have been extensively experimentally validated (e.g., [34,38,39]).

The concrete uniaxial stress-strain response is modeled using the Popovics and Modified Park-Kent models [40] for the pre- and post-peak responses, respectively, as shown in Figure 6-9a. The reinforcing steel stress-strain response is modeled as a tri-linear response in tension comprised of a linear-elastic, a yield plateau, and a nonlinear strain-hardening response until rupture; a buckling response in compression is also considered using the model of Akkaya et al. [41], as shown in Figure 6-9b. The longitudinal reinforcing steel of each member is discretely modeled while the shear reinforcing is smeared into the element.

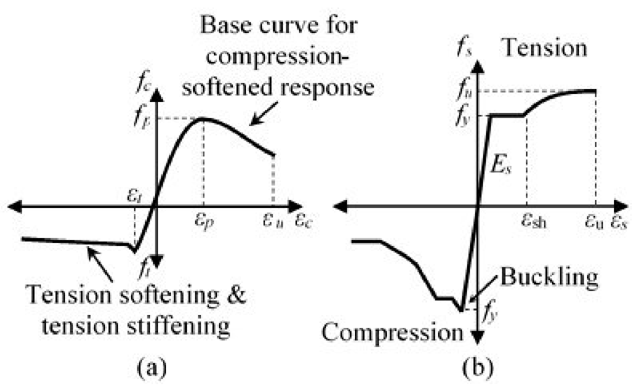

Figure 6-9: (a) Concrete and (b) reinforcing steel stress-strain response.

Because the RC building is designed following modern design guidelines that aim at preventing beam-column joint failures, rigid-end offsets are used to model the beam-column and the column-foundation joints of the building. The boundary conditions are defined by fixed supports at the bottom of each column. The created computational model of the seven-story RC building is shown in Figure 6-8b.

6.4.3 Process 1A: Structural Assessment to Tsunami Loads

Characterization of the tsunami load is performed using a triangular static-equivalent lateral hydrodynamic force, which is the approach proposed in current design guidelines [29] that has been shown to provide good predictions of structural responses when compared to a wide range of dynamic time-history analyses [42]. The force per building's unit width is calculated based on the tsunami flow regime (i.e., subcritical or choked). At the building location, the inundation depth and flow velocity are calculated to be 2.4 m and 4.5 m/s, respectively, using the energy grade line analysis method of ASCE 7 [29], which results in a Froude number of 0.93. As indicated in [42], the critical Froude number for a building located on a sparse environment is 0.68; consequently, the tsunami flow considered in this study is in the choked regime, and the force per unit structural width is calculated using Equation 2 [43].

$$\frac{F}{b} = \lambda \rho g^{1/3} u^{4/3}\, h^{4/3}, \quad if\ F_r \geq F_{r,c} \tag{2}$$

where F is the tsunami force, b is the width of the building, ρ is the density of the fluid, u is the flow velocity, h is the inundation depth, g is the acceleration of gravity, F_r is the Froude number ($u/\sqrt{gh}$), and λ is the leading coefficient [43].

In the CLT computational building model, the tsunami force is applied as a triangular pressure distribution from the bottom of the building to the inundation depth considered, as shown in Figure 6-10. For the RC computational building model, a tributary distance is used to convert the water pressure into an equivalent triangular force. The tributary distance is considered before and after the masonry infill walls collapse due to the tsunami. Before the infill walls collapse, they are assumed to effectively transfer the loads to the adjacent moment frames and the tributary distance is taken as the distance between the moment frames of the building. After the infill walls collapse, they are assumed to be carried away by the wave, making the load affect only the moment frame itself. In this case, a reduced tributary distance equals to the width of the RC columns is considered. The maximum out-of-plane load that the infill walls can resist is calculated using [44].

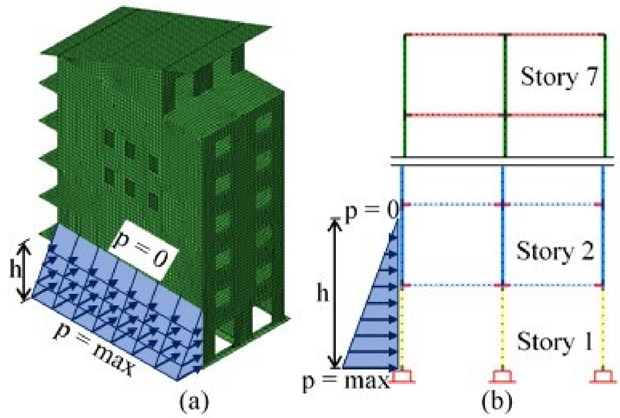

Figure 6-10: Tsunami load application approach on (a) CLT and (b) RC models.

The wave is considered to afflict the longest side of each building configuration, as shown in Figure 6-10, as this side provides the largest area for the development of the tsunami pressure. The two building configurations are subjected to a series of tsunami inundation depths starting at 0.5 m and increasing by 0.5 m until their collapse. The flow velocity at each inundation depth is calculated assuming a constant Froude number, which is considered a realistic assumption as shown in typical tsunami onshore flow time-histories [42].

6.4.4 Process 1B: Natural Hazard-Based Life Cycle Assessment Analysis

Key common properties of the two building configurations are used to define the functional unit as a 13.5 m x 7.7 m seven-story building designed according to Eurocode 8 [28] to resist the peak ground accelerations of the Kobe JMA earthquake. The life cycle inventory (LCI) data are site-specific, based on recent technologies and normal production conditions. The life cycle impact assessment is calculated based on the LCI inputs using

TRACI 2.1 [45] characterization factors and the LCA software GaBi [46]. The use phase is not included in the framework as previous studies have demonstrated similar environmental impacts for CLT and RC buildings (e.g., [47]). A summary of the main assumptions made to compile the LCI inputs and quantify the outputs of each LCA phase is discussed next.

6.4.4.1 Material manufacturing and construction phases

For the CLT building, the panels are produced and shipped from a manufacturing plant 777 km away from the construction site whereas the metal connectors are produced by a steel plant and shipped from a hardware store located 34 km away from the building site. The construction of the CLT building is mainly comprised of two procedures: lifting of the panels to their location and fastening of each member connection. The lifting is performed by a diesel-powered telescopic boom truck crane with a 300 hp engine power that is considered to work at a power rate of 65%, which is intended to accommodate periods during the construction in which the truck is not operating at full power. The fastening of the connections is performed with 600 W power drills that are commonly used in wood construction projects. For the RC building, the concrete, reinforcing steel, and bricks are produced and shipped from existing manufacturing plants located 24 km, 214 km, and 34 km, respectively, from the building site. The construction of the RC building is mainly comprised of concrete pumping since the reinforcing steel is manually placed. The pumping is performed by a 200 hp diesel-powered truck-mounted concrete pump capable of pumping 100 m3 of concrete per hour.

6.4.4.2 Retrofit phase

For the CLT building, two main retrofit actions are considered: replacement of failed CLT panel connections and replacement of CLT panels that experience stress levels above 80% of their strength. For the RC building, the retrofitting of the beam and column elements are based on the calculated crack damage and concrete and reinforcing stresses. For crack widths below 0.3 mm, cosmetic crack sealing procedures are performed, whereas crack widths above 0.3 mm are retrofitted via filling with epoxy mortar to ensure concrete integrity and prevent reinforcing steel corrosion. For concrete stresses above 80% of its compressive strength or for reinforcing stresses above the yield stress, concrete jacketing on the damaged member is performed. The environmental impacts associated with the jacketing procedure are calculated following [48].

6.4.4.3 Demolition phase

For the CLT building, the demolition is comprised of the disassembly of the CLT panels using the telescopic boom truck crane and power drill discussed in the construction phase (see Section 3.4.1). Consequently, except for the impacts related to the manufacturing and shipping of the materials, the demolition environmental impacts are the same as the construction impacts. For the RC building, the demolition is performed using a demolition truck with a 360 hp engine operating at a power rate of 65%, which considers periods of the demolition in which the truck is not operating at full power.

6.4.4.4 Recycling phase

For the CLT building in the first case (see description of the two recycling cases in Section 2.3), 100% of the CLT panels are recycled. In the second case, only 60% of the CLT panels are recycled whereas the remaining 40% are sent to a landfill facility.

Recycling of the CLT panels is performed by shipment of the panels back to the manufacturing plant to be used as recycled CLT panel products. For the RC building in the first case, the concrete waste is sent to recycling. In the second case, only 60% of the RC waste is sent to recycling while the remaining 40% is sent to a landfill. In the recycling plant, 60% of the concrete waste is recycled and the remaining 40% is disposed of in a landfill, as per [48]. The RC recycling plant is located 149 km from the building location and the landfill is located 32 km from the recycling plant.

6.4.5 Processes 2A & 2B: Performance Limit States Determination and Performance Normalization Factors

The first story interstory drift (ISD) ratio is selected as the EDP to define the performance limit states of the two building configurations. ISD is the most common EDP for the performance-based engineering analysis of buildings and has been extensively used to investigate the performance under earthquake loads. Since tsunamis impose lateral loads analogous to seismic loads, several studies have used the ISD as EDPs for tsunami performance assessment (e.g., [42,49]).

Two approaches are used to determine the performance limit states for the CLT and RC buildings due to the fundamental differences in their main tsunami load-resisting mechanisms (discussed in Section 2.1). For the RC building, displacement is increasingly applied at the first story level of the building. This approach is used because it represents the main tsunami load-resisting mechanism RC building, which is the moment frame lateral resistance. For the CLT building, since its main tsunami load-resisting mechanism involves significant interaction between the in- and out-of-plane panels, a fictitious displacement-type load cannot be easily derived. Thus, the calculated response to the highest imposed tsunami inundation depth is used. The two buildings responses are shown in Figure 6-11.

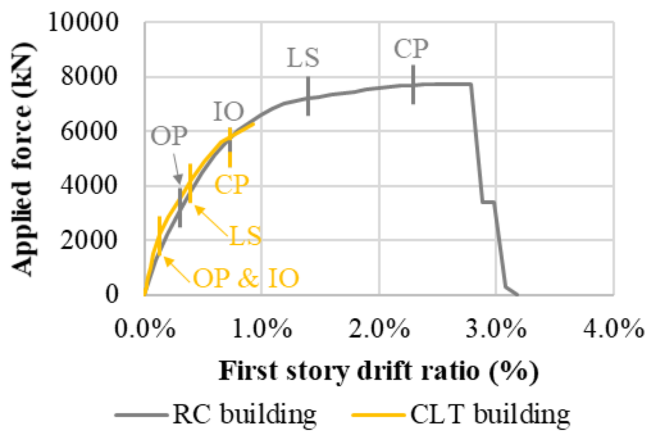

Figure 6-11: CLT and RC building response to determining performance limit states.

For the RC building, the ISD ratios corresponding to each performance limit state are defined following the recommendations of ASCE 41 [10] which is the drift at which: the first cracking occurred for the OP limit state, minor cracking and limited yielding occurred at a few locations for the IO limit state; extensive damage to beams, shear cracking in ductile columns, and joint cracks occurred for the LS limit state, and extensive cracking in ductile elements and severe damage in columns for the CP limit state. For the CLT building, the ISD ratios are defined as the drift at which: the first connection failed for the OP and IO limit states, all of the connections of a single wall panel failed for the LS limit state, and as 75% of the collapse drift for the CP limit state. Based on the defined ISD and the corresponding force levels for each performance limit state, Equation 1 is used to calculate the Performance Normalization Factors (PNF) for the RC building while the CLT building is treated as the reference building. The ISD and PNF results are summarized in Table 6.2.

Table 6.2: Performance limit states for the CLT and RC buildings.

Performance Limit	Force (kN) CLT Building	Force (kN) RC Building	ISD CLT Building	ISD RC Building	Performance Normalization Factors (PNF)
Operational (OP)	2198	3024	0.13%	0.30%	2.7
Immediate Occupancy (IO)	2198	5599	0.13%	0.70%	6.0
Life Safety (LS)	4229	7184	0.40%	1.40%	3.9
Collapse Prevention (CP)	5583	7688	0.66%	2.30%	3.7

6.5 Results and Discussions

6.5.1 Structural Assessment

No significant damage was calculated for the CLT building under inundation depths below 3.0 m (i.e., approximately the height of the first story). As inundation depths increased, an increasing number of CLT panel connections on the first story of the side afflicted by the tsunami load failed. With a reduced number of panel connections (after failures), increased loads were re-distributed which caused overloads that spread to the adjacent connections until the inundation reached 6.0 m, which was the maximum resisted inundation depth of the CLT building (i.e., approximately the height of the second story). For larger inundation depths investigated (i.e., 6.5 m), all of the first story panel connections on the loaded building side failed, which significantly increased the stresses on the CLT wall panels, causing the failure of the long span walls, as shown in Figure 6-12a. The stresses on the short span walls were not enough to cause their failure due to the restraint provided by the in-plane walls, which reduced the span of the walls and, consequently, the tsunami-applied bending moments. Despite the survival of the shorter walls, it was assumed that the failure of the long span walls would cause tsunami loads to afflict and fail the interior walls since their lengths are similar to the exterior walls. Since

CLT wall panels comprise the main structural system of the building, this inundation depth was considered to initiate the building collapse.

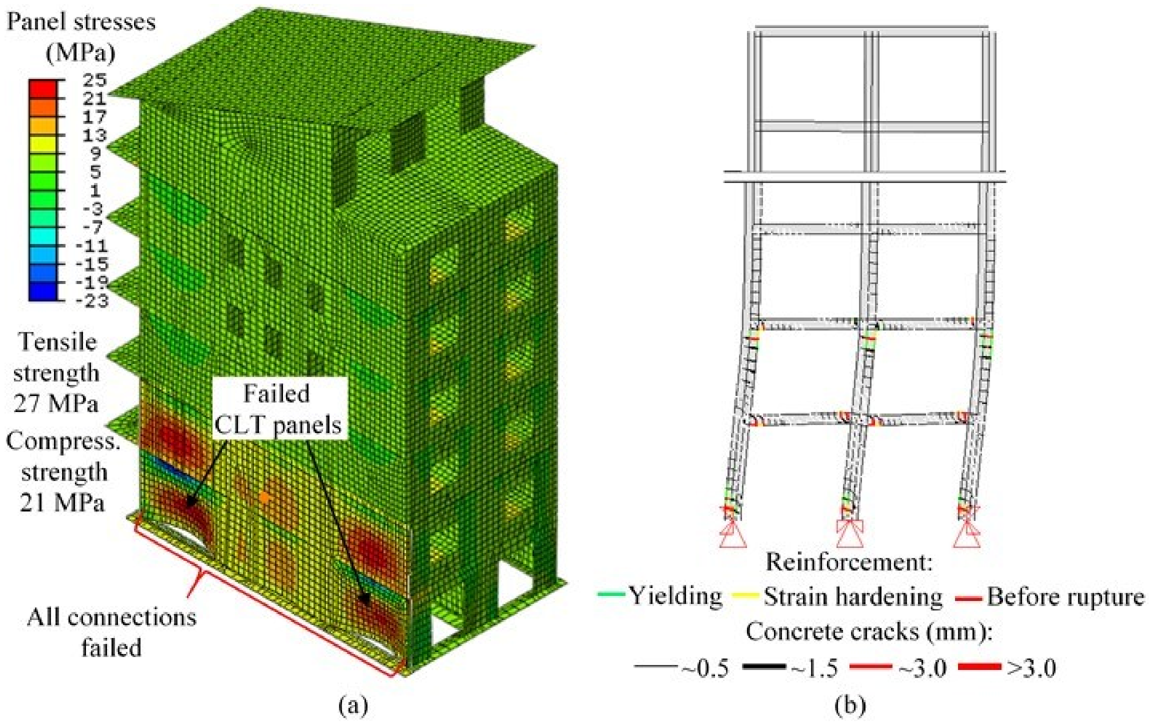

Figure 6-12: (a) CLT and (b) RC building response at the highest resisted tsunami inundation depth.

For the RC building, no significant damage was calculated until the tsunami inundation depth reached 2.0 m, where minor cracks occurred at the bottom of the first story columns. As inundation depths increased, the cracks widened and propagated along the beams and columns of the first stories. At an inundation depth of 5.0 m, the first reinforcing steel yielding occurred at the base of the first story columns. At the maximum resisted tsunami inundation depth (i.e., 8.0 m), extensive cracking was calculated in the first three stories of the building and several reinforcing steels experienced post-yield stress levels, with many approaching the rupture stress, as shown in Figure 6-12b. For larger inundation depths investigated (i.e., 8.5 m), the building collapsed due to reinforcing steel rupture and extensive damage to the first story beams and columns.

Figure 6-13 compares the ISD versus inundation depths response of the two building configurations. Similar ISDs were calculated until an inundation depth of 5.6 m. At higher inundation depths, the RC building's ISD increased significantly due to the softer response caused by the damaged beams and columns. The maximum resisted inundation depth of the RC building was 1.3 times higher than that of the CLT building. In addition to resisting a lower tsunami inundation depth, the performance of the CLT building was considerably lower than that of the RC building. Figure 6-13 shows that, for a tsunami inundation depth of 5.8 m, for example, the CLT building experienced post-LS responses while the RC building was at the IO performance limit state. In addition to structural resilience, ductility (i.e., the ability to undergo significant deformation before failure) can be an indicator of the energy absorbed by the building. At their maximum resisted inundation depths, the first-story drift of the RC building was approximately 4.8 times higher than that of the CLT building, as shown in Figure 6-13, which shows that the ductility of the CLT building at failure was 79% lower than that of the RC building.

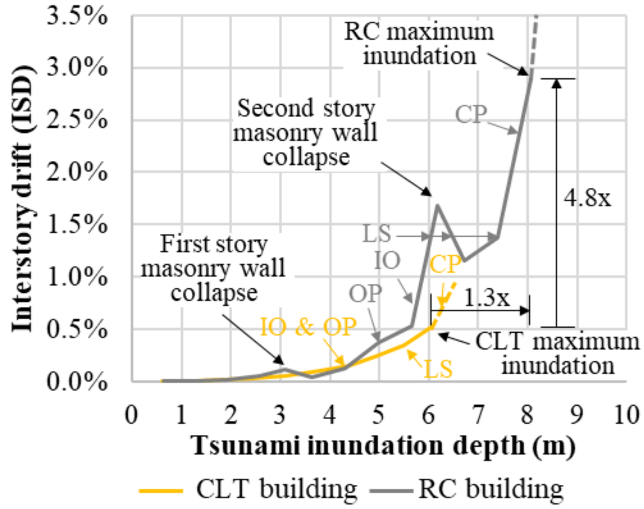

Figure 6-13: First story drift versus inundation depth response.

6.5.2 Life Cycle Environmental Assessment

6.5.2.1 Reference impacts

Reference environmental impacts (i.e., where no tsunami damage occurs) were calculated and are shown in Figure 6-14. For each category, the 100% impact is attributed to the building configuration with the highest environmental impact for that category. The reference impacts of each building configuration indicate that the total environmental impacts of the CLT building were, as an average of all investigated impact categories, 39% lower than those of the RC building. This result validates the calculated life cycle data as it agrees with the findings of the previous studies (e.g., [50–52]).

The large amounts of energy required to produce RC are clear in Figure 6-14, where the material manufacturing was the most environmentally degrading phase of the RC building accounting for, on average, 81% of the total impacts. For some of the impact categories, this phase alone resulted in higher environmental impacts than the total impacts of the CLT building. For the CLT building, the total environmental impacts had a better distribution throughout the different LCA phases. The construction phase was responsible for the highest environmental impact contribution, accounting for, on average, 36% of the total impacts. Different from the other impact categories, the ODA and SA impacts of the CLT building were significantly higher and comparable to those of the RC building. This result occurred due to the large shipping distance (i.e., 777 km) from the CLT manufacturing plant to the building site. This is one of the existing limitations of constructing with CLT materials as only a few manufacturers are currently available in North America (i.e., about 10) compared to much more prevalent concrete plants. The detrimental environmental effects of large CLT travel distances have also been confirmed by previous literature studies (e.g., [53]). This study has a "favorable" scenario in terms of CLT travel because most of the plants in North America are on the west coast. Consequently, projects in different areas would likely require longer travel distances.

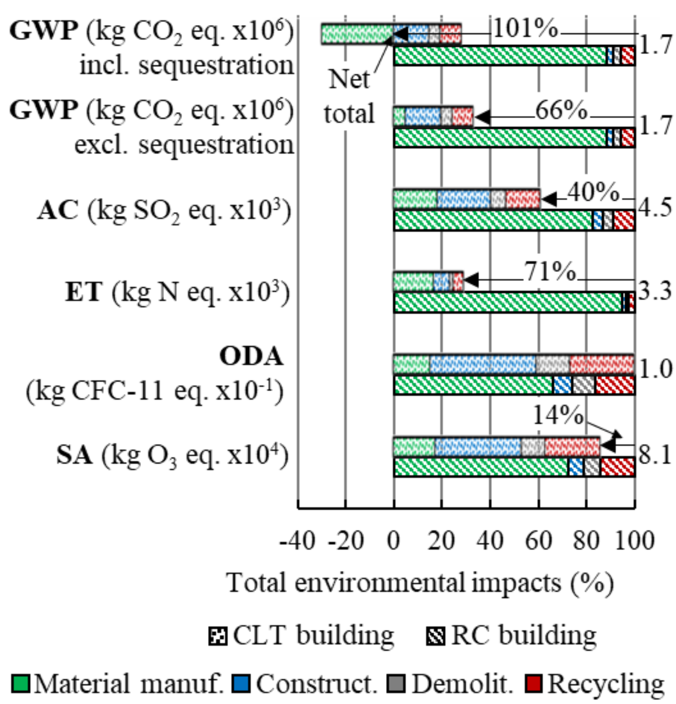

Figure 6-14: Life cycle assessment results for CLT and RC buildings.

6.5.2.2 Tsunami-induced environmental impacts

The results shown in Figure 6-15 indicate the non-normalized environmental impacts of the CLT and RC buildings for each tsunami inundation depth investigated. The impacts at the inundation depth of zero meter are equivalent to the reference impacts shown in Figure 6-14. The increase in total environmental impacts caused by the retrofit actions on the CLT building was insignificant when compared to its reference impacts (see the damage and undamaged results in Figure 6-15) and only significant for the RC building after the point where RC jacketing was required. After this inundation depth, a noticeable increase in the environmental impacts of the RC building (i.e., ~9%) in all impact categories was observed, as indicated in Figure 6-15a.

As shown in Figure 6-15, the most significant environmental impact increase for the two building configurations occurred when the buildings collapsed due to the tsunami. The collapse of the CLT and RC buildings increased their total environmental impacts by, on average, 30% and 82%, respectively. The building's collapse caused a larger increase in the environmental impacts of the RC building due to the significant environmental impacts of its material manufacturing phase, as discussed in Section 4.2.1 and shown in Figure 6-14.

For most of the impact categories analyzed, the difference in the impacts of the two building configurations was sufficiently large that not even the collapse of the CLT building (i.e., at 6.5 m) resulted in higher impacts than the reference impacts of the RC building, as shown in Figure 6-15a to Figure 6-15d. The ODA and SA were the only categories in which this result was not applicable. For these categories, at inundation depths between the collapse of the CLT and RC buildings (i.e., between 6.5 m and 8.5 m), the

CLT building resulted in higher environmental impacts than the RC building, as shown in Figure 6-15e and Figure 6-15f.

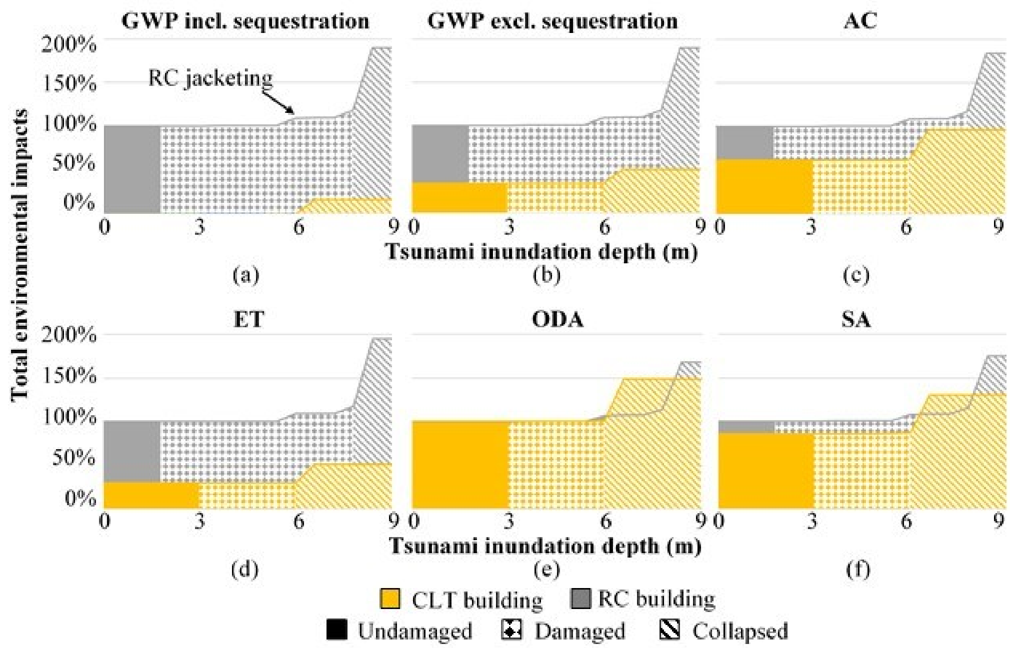

Figure 6-15: Life cycle assessment for the CLT and RC buildings under different tsunami inundation depths.

6.5.3 Goal: Structural Resilience-Based Environmental Assessment

In this section, the calculated Performance Normalization Factors (PNF) are used to normalize the uncoupled structural and environmental results – discussed in Section 4.1 and Section 4.2 – and enable a normalized quantitative comparison of the environmental impacts versus the structural resilience of the CLT and RC buildings. The environmental impacts of the RC building are normalized to the CLT building using the PNFs calculated in Section 3.5. The normalized environmental impacts for each performance limit state are shown in Figure 6-16.

The results of the GWP (excluding sequestration) and the ET categories show that for the first performance limit state considered (i.e., OP), the CLT building had lower normalized environmental impacts. This result occurred because, at the first performance limit state, the structural performance of the two building configurations were similar, as discussed in Section 4.1 and shown in Figure 6-13. In this case, the structural performance does not play a major role in the assessment while the sustainability governs the determination of the favorable building configuration. For subsequent performance limit states, the normalized environmental impacts of the CLT building were either similar or higher than the RC building due to their significantly different structural performance.

The results for the AC, ODA, and SA impact categories show that the RC building had lower normalized environmental impacts for all performance limit states investigated. This result occurred because these impact categories were the ones with minimal difference in environmental impacts between the CLT and RC buildings, as shown in Figure 6-15. When the significantly different structural performances of the two building configurations were normalized, the RC building became a more favorable alternative.

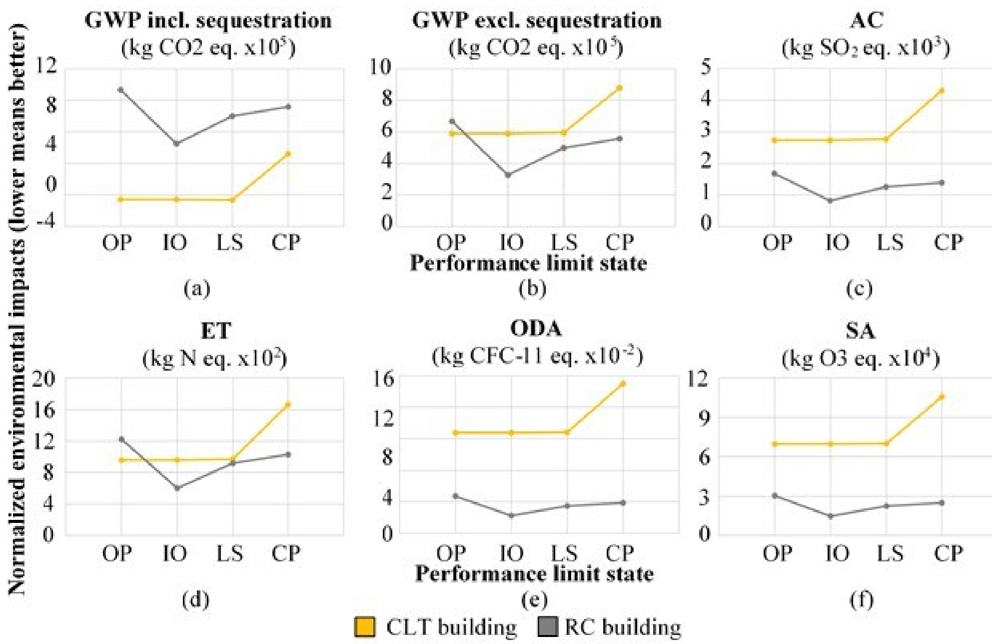

Figure 6-16: Environmental impact to inundation depth ratio for the CLT and RC buildings.

In the GWP (including sequestration) category, the CLT building had lower normalized environmental impacts for all performance limit states considered. This result is directly related to the majority of the CLT structural system being comprised of CLT panels, which have the ability to act as a carbon sink provided that it comes from sustainably managed forests. This ability allows the CLT building to significantly diminish its carbon footprint, especially in comparison to traditional material alternatives such as reinforced concrete.

6.6 Study Limitations and Future Research

The objective of this study is to take the first step in creating a multidisciplinary framework that combines PBE with LCA to quantify and compare the structural resilience-based environmental impacts of different building configurations. There are many more aspects that need to be investigated in future studies to derive more comprehensive conclusions. These aspects may include stochastic and probabilistic methods to produce statistical outcomes while accounting for the probability of different natural hazard recurrence intervals on random building configurations, locations, and natural hazard load conditions. The consideration of such aspects would also improve the generalization of the results, which, for the case study performed in this study, is restricted to the considered buildings, their configuration, design conditions, and locations investigated.

The structural part of the framework can also be expanded to multi-hazard analysis approaches. For instance, the earthquake resilience and pre-tsunami earthquake damage of each building configuration considered will likely have an impact on their structural performance during the tsunami. The same might occur for fire resilience after an earthquake, wind resilience after a flood, and other combinations of natural hazards. In addition, dynamic response history analysis, rather than static equivalent ones, should be employed for building configurations with plan and elevation irregularities, or where the contributions of higher mode effects are expected to be significant as in the case of taller buildings.

The environmental part of the framework should be expanded to include life cycle aspects other than environmental impacts. Examples of such aspects are the costs involved in each LCA phase considered; the required time for the construction, demolition, and retrofit actions, which can produce economic and societal impacts due to the downtime of the damaged structure; and the energy usage, which, depending on the energy matrix of the considered locations, may significantly alter its environmental impacts.

6.7 Summary and Conclusions

In this study, a multidisciplinary framework that combines performance-based engineering with life cycle assessment was created to quantify and compare the structural resilience-based environmental impacts of different building configurations. To demonstrate its application, the framework was used to investigate and compare a seven-story building made from cross laminated timber (CLT) and reinforced concrete (RC) materials located in a tsunami-prone region. The following conclusions are drawn from this study:

- The proposed framework is based on the accurate computational characterization of the building configurations to predict their performance and damage to natural hazard loads. The performed case study demonstrated that the computational modeling could effectively quantify the performance and damage of the two investigated building configurations to tsunami loads.
- The proposed framework includes a structural assessment to natural hazard loads that allow for the use of both dynamic and static-equivalent load procedures in incremental steps to characterize the full response of the building configurations from their initial-elastic to the near-collapse-nonlinear stages.
- The proposed framework includes a natural hazard-based life cycle assessment that can be effectively used to obtain the environmental impacts of building configurations based on their structural resilience to natural hazard loads.
- The Performance Normalization Factor (PNF) permits a direct numerical quantitative comparison of the performance limit states of each building configuration. The PNF can be effectively used to normalize the environmental

impacts of one of the investigated building configurations to the same structural performance as the other. The normalized environmental impacts have been shown by the performed case study analysis to allow for the normalized comparison of the environmental impacts versus the structural resilience of the different building configurations considered.

- The application of the proposed framework for the case study investigated indicates that the structural resilience to natural hazard loads can offset the benefits of environmental impacts. The magnitude of the offset depends on the combination of the building configurations, performance limit states, and environmental impact categories are considered.
- For the case study investigated, the RC building is shown to have better structural resilience to tsunami loads while the CLT building have lower environmental impacts. The use of the calculated PNFs to perform the normalized structural resilience-based environmental assessment indicates that, when the difference in structural resilience between the two building configurations is considered, the RC building presents lower normalized environmental impacts than the CLT building for the majority of environmental impact categories and performance limit states investigated.

6.8 Acknowledgments

The authors would like to thank Dr. Defne Apul for the advice and resources used to perform the life cycle impact assessment in this study.

Chapter 7

Conference Paper I - Modelling Beam-Column Joints for Progressive Collapse Analysis [6]

7.1 Abstract

When a reinforced concrete frame is subjected to progressive collapse due to the loss of a structural column, the surrounding elements typically experience a significant overload that may lead to their collapse. The rotational capacity of beams and, consequently, the beam-column connections is a critical factor determining the structural resiliency. Numerical models developed to assess the structural response under a progressive collapse situation must incorporate the beam-column joint response. In this study, a review of the beam-column joint modelling approaches, constitutive models, and the ease of their numerical implementation are presented. Some of these models are utilized to simulate the response of a previously-tested reinforced concrete frame. The calculated structural response parameters are compared to the experimental results, and the accuracy of each constitutive model is discussed.

---

[6] Reprinted from the proceedings of the 2017 IABSE Symposium in Vancouver, Rafael A. Salgado & Serhan Guner, Modelling Beam-Column Joints for Progressive Collapse Analysis, 592-599, © 2017, with permission from International Association for Bridge and Structural Engineering (IABSE). For the published version, please refer to https://www.researchgate.net/publication/320044012_Modelling_Beam-Column_Joints_for_Progressive_Collapse_Analysis.

7.2 Introduction

Progressive, or disproportionate, collapse refers to a localized structural collapse that forces the adjoining members to fail, initiating a domino effect. Localized fire, natural disasters, vehicle impacts, terrorist attacks, and many other events may trigger the progressive collapse of a structure.

To mitigate the impacts of a progressive collapse, alternative load paths must be present in a structure. In a common progressive collapse scenario where a structural column is lost, three critical load resisting mechanisms form: 1) the compressive arch action (CAA), which is the additional flexural resistance due to the axial restraint of the surrounding structure; 2) the plastic hinge action (PH), where large structural displacements occur on the beams due to the plastic hinge formation; and 3) the catenary action (CA), where tensile resistance develops due to the extreme deflections of the beams (see Figure 7-1).

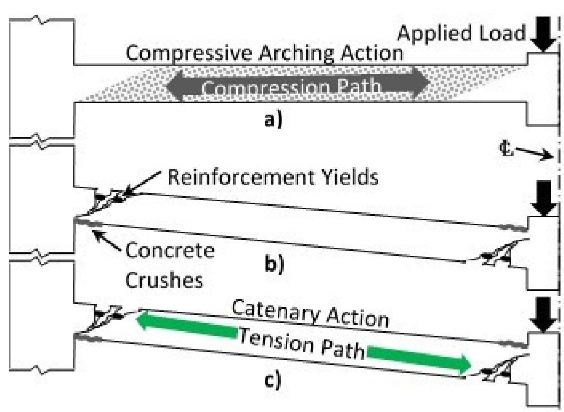

Figure 7-1: Resisting mechanisms: a) arching action, b) plastic hinge, and c) catenary action.

Due to the concentrated deformations of the concrete beams at the beam-column connections, previous studies indicated the rotational capacity of the beams to control the development of catenary actions [1]. Additionally, beam-column joints are critical for resisting and distributing loads [2], as well as determining the rotational capacity of the beams.

In this study, existing state-of-the-art numerical beam-column joint modelling techniques and constitutive behaviors from the literature are assessed using a previously-tested planar reinforced concrete frame subjected to progressive collapse analysis by the removal of a ground-level structural column. The accuracy and easy-of-use of the joint models are evaluated by comparing the calculated response parameters with the experimental results.

7.3 Modelling of Joints

Two main factors affect the beam-column joint behavior: panel shear and bond-slip actions. The application of extreme loading on members adjacent to a beam-column joint results in substantial shear deformation in the joint panel zone. In addition, the common practice of terminating the longitudinal reinforcing rebar inside the joint diminishes the flexural resistance of the beams. Consequently, the joint damage mechanism due to high shear and bond stresses reduce the strength and stiffness of the frame.

Amongst various beam-column joints modelling techniques, three methods have been widely used: rigid-joint, rotational-hinge, and component models.

In rigid-joint models, joint damage is neglected by modelling a perfectly-rigid connection between the beam and the column elements, where moments are fully transferred from one element to the other (see Figure 7-2a). The rigid element region encompasses the physical joint core and, due to its stiffer response, the joint damage becomes concentrated at the interface with the beam, or column. Rigid-joints yield reasonably accurate results when beam-column joint damage is not a dominant structural behavior. When this is not the case (e.g., a progressive collapse loading), such models fail to account for the actual joint panel deformations, which results in a unconservative (i.e., unsafe) strength and deformation calculation.

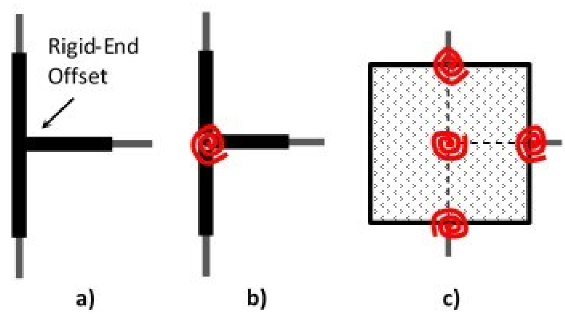

Figure 7-2: Beam-column joint modelling methods.

In the rotational-hinge joint models, a single rotational-spring that accounts solely for the shear panel stress-strain deformation is incorporated at the center of the beam-column connection, which is modelled with rigid-end offsets (see Figure 7-2b). The rigid links are used to neglect the damage in the elements at the joint panel, while joint deformations are simulated by the moment-rotation constitutive behavior of the center spring. This model was widely used in the literature (e.g. [3,4]) and, despite its simplified methodology, provided reasonably accurate results. This model should not be used, however, when the bond-slip action is a critical behavior.

Component models incorporate a more realistic constitutive model, where joint panel shear-deformation and bond-slip are explicitly modelled. The shear deformation is usually incorporated either by springs or continuous panel elements, whereas the bond-slip relationships of adjacent elements are accounted using 1-D springs (see Figure 7-2c). Many component models have been proposed in the literature (e.g. [5-7]); however, these models require many constitutive models for each considered behavior (i.e. spring), which in most cases are not readily available or difficult to obtain, thus hindering their effective and practical applications.

In this study, the rotational-hinge joint model is incorporated in the numerical analyses due to its relative simplicity, reasonable accuracy, and given that the bond-slip effects are not a critical mechanism for the frame structure examined. For comparison and quantification of the effects of beam-column joint modelling, a rigid-joint model is also examined.

7.3.1 Shear Panel Constitutive Model

The available models in the literature typically use calibrated joint-panel shear stress-strain response derived from experimental testing of a set of specimens with certain geometry and reinforcement configuration. When analyzing an existing or planned structure using these models, the calculation accuracy will be significantly affected by similarities between the structure being modelled and the experimental dataset used in the model calibration. Consequently, the existing joint models should be used with caution.

The backbone of the joint panel shear stress-strain response is generally controlled by four damage states: concrete cracking, yielding of stirrups, shear strength, and residual joint shear capacity, as shown in Figure 7-3.

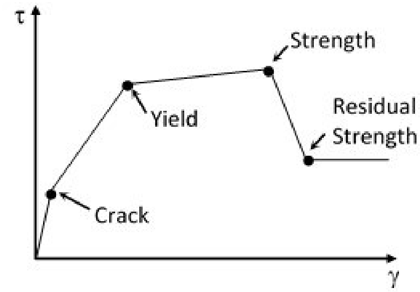

Figure 7-3: Joint shear panel damage states.

In this study, five constitutive models from the literature were considered: Teraoka and Fujii [8], Theiss [9], Anderson et al. [10], Birely et al. [11], and Kim and LaFave [12].

The Teraoka and Fujii [8] constitutive model defines each damage state with a fixed strain pattern obtained from an experimental database though curve fitting. The relationships were derived based solely on concrete properties and joint type (i.e., exterior or interior joint, and transverse beams or not). Consequently, four joint backbone points can be quickly defined using this model. However, this simplicity may result in deteriorated reliability and accuracy.

Theiss [9] proposed a constitutive model that employs fixed strain values and percentages of the maximum shear stress for the joint backbone response. The Theiss [9] model uses the Modified Compression Field Theory (MCFT) [13] to determine the nominal shear capacity of the joint. The MCFT, however, employs an iterative, 17-step, calculation procedure to estimate the shear stress capacity, which hinders the practical application of this model.

The Anderson et al. [10] model calculates the stress and strain backbone points using fixed stiffness values for each segment that are based on the joint maximum shear stress. It was calibrated for internal beam-column joint assemblies with insufficient amounts of transverse reinforcement, which might result in a reduced accuracy for adequately-designed joints.

The Birely et al. [11] model defines the joint-shear backbone with only two points: flexural yield of the adjacent beam, and the maximum shear capacity, with a brittle failure once the capacity is reached. This model is placed at the beam-joint interface, not at the center of the beam-column connection. The model limits the beam moment capacity as per the joint response. The bilinear constitutive behavior makes the implementation relatively simple. However, this model was developed solely for interior joints, and uses fixed maximum strain and stiffness values.

The Kim and LaFave [12] defines the crack, yield, and residual strength damage states as proportional to the maximum shear and strain values. Its main advantage is its "unified" constitutive model that does not employ fixed values of stress or strains. It incorporates the effects of the compressive strength of the concrete, in-plane and out-of-plane geometry, joint eccentricity, beam reinforcement, and joint transverse reinforcement for a comprehensive maximum shear and strain calculation.

7.3.1.1 Cyclic hinge response

When subjected to cyclic loading conditions, beam-column joints typically experience a highly-pinched hysteresis response. Even though this study performs only nonlinear static analyses, the beam-column joint still experiences unloading due to the compression-tension alternation between the CAA and CA mechanisms. Consequently, it is important to consider the hysteretic response of the joint for progressive collapse analyses. Figure 7-4 shows the joint cyclic behavior proposed by Lowes et al. [14].

Similar to the backbone response of the joint, the majority of existing studies derive the cyclic pinching parameters based on an experimental curve fitting approach; very few studies propose generally applicable pinching. This study incorporates the hysteretic parameters obtained by Jeon et al. [4], due to its comprehensible set of 124 beam-column joint specimens analyzed.

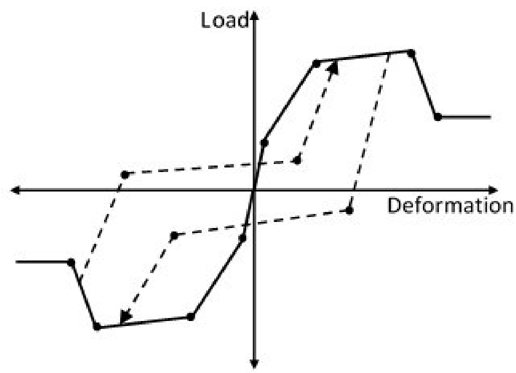

Figure 7-4: Beam-column joint hysteretic behavior (adopted from Lowes et al. [14]).

7.4 Experimental Verification

Amongst the experimental studies available in the literature for the progressive collapse conditions, the work of Lew et al. [1] was selected for this numerical study due to its planar configuration and elements designed per modern building codes. The planar configuration of the frame permits a simpler and computationally efficient numerical modelling. In addition, the proper design of frame elements allows for the exclusion of structural behaviors such as bond-slip and column shear failure, thereby isolating the behaviors of beams and beam-column joints studied herein.

The frame is part of a 10-story structure with the design carried out by a consulting engineering firm as per the requirements of ACI 318-02 [15] for the seismic design category C. The frame is comprised of a symmetric beam and column assembly, with the middle column representing a column loss scenario. Each external column was embedded into spread footings, which was clamped down to the strong floor. The top of the column was restrained by a two-roller fixture and the load was applied in the form of a displacement on the middle column (see Figure 7-5).

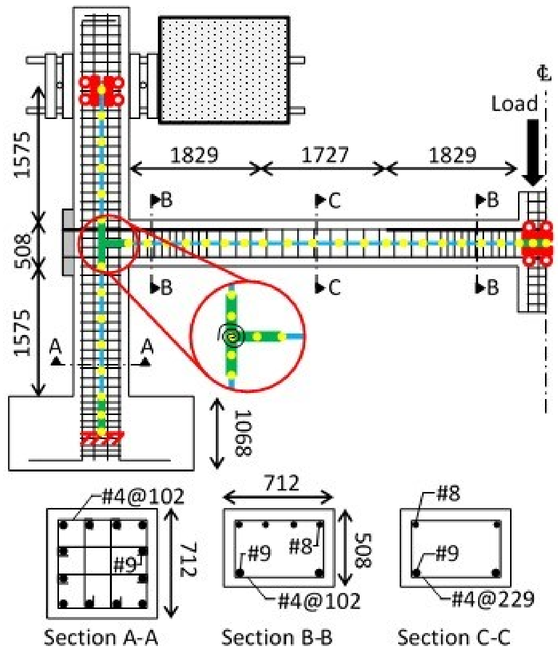

Figure 7-5: Lew et al. [1] frame's specimen and numerical model.

The beam's reinforcing steel was anchored by an external plate attached to the exterior of the beam-column joint face, as shown in Figure 7-5, to represent the continuity of the longitudinal bars. The average compressive strength of the concrete was 32 MPa, and the average reinforcing steel properties were as listed in Table 7.1.

Table 7.1: Average reinforcing properties.

Bar Size	Yield Stress [MPa]	Ultimate Stress [MPa]	Hardening Strain [me]	Rupture Strain [me]
#4	524	710	9	140
#8	476	648	8	210
#9-B	462	641	7	180
#9-C	483	690	7	170

The reported failure mode was the rupture of the longitudinal bottom reinforcement of the beam at the beam-middle column interface. In Figure 7-6, the cracking pattern at the failure load is shown. Although the beam-column joint was not the main failure mechanism, Figure 7-6 shows extensive shear cracking at the joint, which indicates a high joint stress demand.

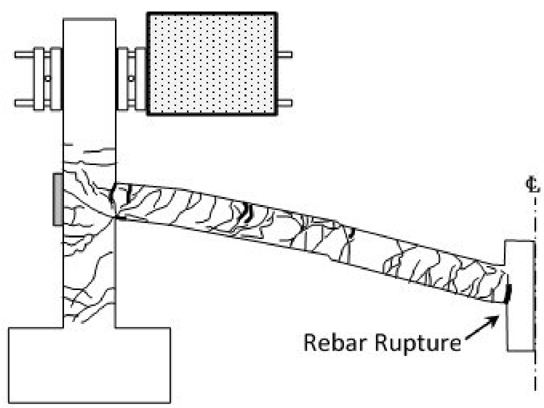

Figure 7-6: Cracking pattern at failure condition (adopted from Lew et al. [1]).

7.5 Numerical Model

The numerical model was developed using the OpenSees [16] software with displacement-based frame elements idealized at the centerline of the structural components (see Figure 7-5). One half of the structure was modelled due to symmetry. The height of the column spans from the mid-height of the concrete foundation to the mid-height of the two-roller fixture as shown in Figure 7-5.

Semi rigid-end offsets were incorporated at the beam-column joints and the column footing, where the area of longitudinal reinforcement was doubled and the transverse reinforcement space reduced in half. These semi rigid-end elements cover the beam-column intersection and half the column's foundation height. As mentioned for rigid joints, these elements act to shift the damage concentration from the joint panel to the beam or column interfaces. The semi-rigid modelling approach permits more flexibility at the joint panel zones as compared to the rigid-end offsets. At the axis of symmetry, semi rigid-ends were also included to account for the increased stiffness of the intersection.

A two-dimensional fiber based cross-section with concrete and longitudinal steel fibers were incorporated in each frame element, following the design shown in Figure 7-5. Confinement of each element concrete core was calculated using the Mander [17] model.

The column foundation was idealized as a rigid support. The two-roller horizontal fixture allows the column to displace vertically; consequently, it was modelled with a rigid vertical roller. Finally, at the beam-middle column intersection at the plane of symmetry, a rigid horizontal roller was defined (see Figure 7-5).

Load was statically applied in the form of vertical displacements on the three nodes that comprise the beam-middle column connection. A 1-mm displacement increment was imposed downwards on each of these nodes over the middle column joint up to the structural failure, characterized as the structural collapse or non-convergence of the load stage results.

The analysis was repeated using different constitutive models incorporated in the rotational-hinge beam-column joint model studied.

7.5.1 Beam-Column Joint

OpenSees [16] provides a number of beam-column joint elements in its online user's manual. However, these elements are component model elements, for which the analyst needs to specify all constitutive model parameters for each behavior considered (e.g., shear panel stress-strain and bond-slip responses). The reference manual, however, does not offer guidance on how to obtain or calculate such constitutive models, leaving it to the discretion of the analyst. This limits the software usage to analysts who have expert knowledge on the beam-column joint models (e.g., researchers), which hinders the practical use of OpenSees [16] by the engineering community and practicing engineers.

In this study, the previously-discussed damage state parameters were calculated and incorporated into the joint element using a zeroLength rotational-hinge. The pinching4 uniaxial material model that employs the hysteretic material behavior of the joint (shown in Figure 7-4), developed by Lowes et al. [14], was incorporated in the hinge. The shear stress-strain backbone response calculated at each joint model was converted to a moment-rotation response using the equations derived by Celik and Ellingwood [3]. Figure 7-7 shows the calculated backbone moment-rotation responses for each model.

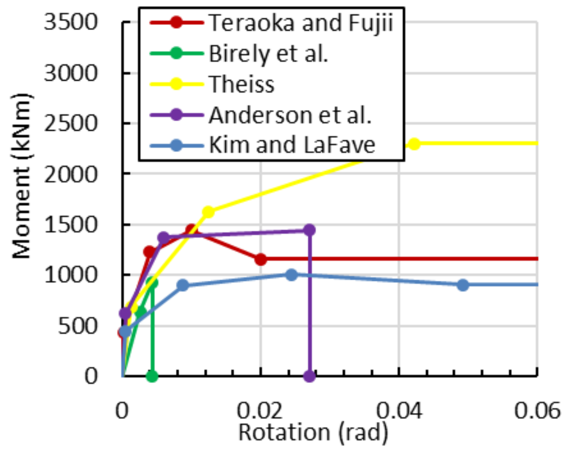

Figure 7-7: Calculated moment-rotation joint response.

As shown in Figure 7-7, the Kim and LaFave [12] and the Theiss [9] models calculated the lowest and highest moment-rotation capacity, respectively, for the frame analyzed in this study. Anderson et al. [10] and Teraoka and Fujii [8] models calculated a similar joint response up to the joint moment capacity, with different post-peak behaviors. Birely et al. [11] calculated the lowest moment capacity. However, this model's moment capacity refers to the beam moment capacity and not the joint moment capacity, since it is incorporated as a spring in the beam-joint interface, and not at the joint center like the other models. In this study, the joint was properly designed and was not expected to reach its shear strength capacity before the flexural capacity of the beam was reached. Thus, only the initial damage states of the moment-rotation curves should govern the joint response.

7.6 Results and Discussion

The total load-displacement response of the middle column is shown in Figure 7-8 for three of the joint models examined. These three models represent the effects of the five joint models analyzed in this study. The response obtained from the Theiss [9] and the

Anderson et al. [10] models were virtually the same as the Teraoka and Fujii [8] model, with a response deviation of less than 3%.

The Kim and LaFave [12] and the rigid joint model calculated the softest and stiffest numerical responses, respectively, whereas the Birely et al. [11] model calculated a response essentially identical to the rigid joint model (see Figures 7-8 and 7-9). The Teraoka and Fujii [8] model calculated a response in between the Birely et al [11] and the Kim and LaFave [12] models.

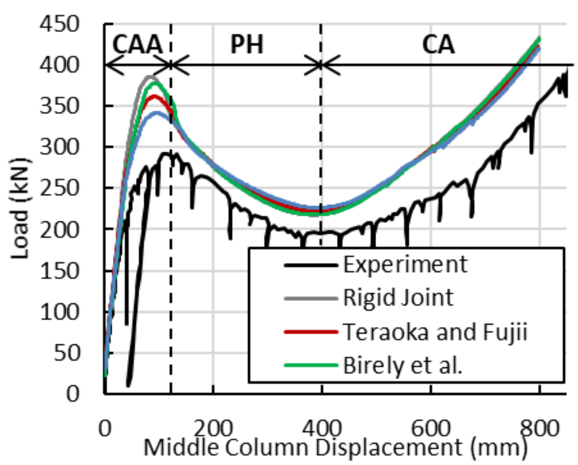

Figure 7-8: Numerical models' load-displacement response.

The numerical models captured the three load resisting mechanisms (see Figure 7-1) with varying degrees of success. The first region of the curve, (i.e., the compressive arch action region) goes up to the beam flexural capacity, where a peak form in the load-displacement response. In the plastic hinge region, the capacity of the beam, and the frame, starts to degrade due to the concrete crushing and steel yielding. The catenary action region progresses based on the additional strength provided by the development of tension forces in the beam-column assembly (see Figure 7-8).

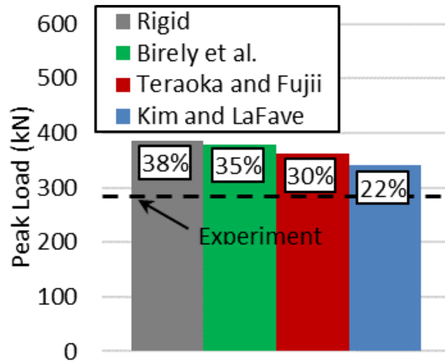

Figure 7-9: Peak compressive arch response and percent deviation to experimental result.

All models calculated the rupture of the bottom beam reinforcement at the middle column interface at approximately the same middle column displacement, which indicates that the strains at the beam-column interface reached the ultimate value for the reinforcement regardless of the joint model analyzed. In Figure 7-8, the response is shown up to a displacement close to where the models failed. Experimental response is terminated at this point due to the extreme damage state that the structure sustained; the experimental response continues up to 536 kN at a displacement of 1076 mm.

As seen in Figures 7-8 and 7-9, the difference in each calculated response is not significant. The Kim and LaFave [12] model provided a better correlation to the experimental response, still with an overestimation of more than 20%. The “unified” stress-strain formulations utilized in this model was the most comprehensive of all models considered and are thought to be responsible for the “closer-to-experimental” calculated structural response.

All joint models considered in this study exhibited negligible discrepancies in the calculated responses at the PH and CAA regions. This indicates that the beam-column joint does not play a critical role after the force peak strength at the CA region (see Figure 7-8).

This might be due to the large rotation of the beam once the plastic hinge started to form at the PH and the CAA regions.

The lack of a visual post-processor interface in OpenSees [16] makes it practically impossible to determine the cracking and damage conditions of the frame. The failure mode can only be estimated manually based on stress-strain response plots of each material, where it can be checked if the ultimate strength has been reached.

7.7 Conclusions

This study presented the numerical simulation results for a planar reinforced concrete frame subjected to a progressive collapse scenario by the removal of a column. The findings of this study support the following conclusions:

- Beam-column joint response is of critical importance in the compressive arch region of the structural response under progressive collapse conditions. In this study, the incorporation of beam-column joint models resulted in a decrease in the peak strength in this region by up to 16% as compared to not modelling the joint damage through the use of a rigid-joint model.
- All models that considered the joint response calculated similar structural responses regardless of the beam-column joint model utilized, with a maximum strength difference of 13% between the models.
- The beam-column joint models did not have a significant impact on the plastic hinge and catenary action regions. A possible reason for this is that the structural response is mainly dominated by the large plastic-hinge deflections of the beams in these regions.

- Most of the beam-column joint constitutive models available in the literature are highly dependent on the experimental dataset used for their calibration. This requires an expert knowledge from the engineer as to which model is more appropriate for the structure being analyzed, and hinders their practical application in industry.
- OpenSees presents a number of beam-column joint elements for numerical analysis. However, very limited user documentation is available as to what constitutive model is recommended to use, where to find them, and how to calculate the input parameters. This results in significant challenges for the correct use of these models. In addition, the lack of a visual post-processor interface makes it practically impossible to assess the structural deflections, crack patterns, damage states, and failure modes.
- The results of this study indicate that even properly designed joints have a significant effect on the structural performance under progressive collapse conditions. It is expected that poorly-designed joints will exhibit a much severe performance loss.

Chapter 8

Conclusions

The high-fidelity numerical models created have demonstrated to satisfactorily capture the structural performance of the considered structure alternatives including: satisfactorily capturing crucial response and important second-order material behaviors such as reinforcement strains, crack widths, energy dissipation, ductility, load-deflection responses, and failure modes of reinforced concrete (RC) structures; and allowing the characterization of the response under out-of-plane-dominant natural hazard loads of cross laminated timber (CLT) buildings, which enabled, for the first time, the assessment of the structural performance of CLT buildings to tsunami loads.

The cradle-to-grave life cycle environmental assessment models created effectively accounted for the effects of natural hazard induced impacts such as the levels of damage and required retrofit actions, the damage-induced demolition, the recycling of the generated construction and demolition waste, and the post-event reconstruction of the structures.

The multidisciplinary framework created to combine performance-based engineering with life cycle environmental assessment provides a powerful means for making science-based decisions when considering newer and seemingly more sustainable building structure alternatives while accounting for their natural hazard resilience level.

References

Chapter 1

[1] Eileen McSaveney, Historic earthquakes - The 2011 Christchurch earthquake, Te Ara - the Encyclopedia of New Zealand. *Online*, 2017. Retrieved from: http://www.TeAra.govt.nz/en/historic-earthquakes/page-13

[2] Federal Emergency Management Agency (FEMA), Seismic Performance Assessment of Buildings. Volume 1 - Methodology, FEMA P-58-1 Publication. (2012) 278.

Chapter 2

[1] Chen XM, Duan J, Qi H, Li YG. Controls on Material and Mesh for Structural Nonlinear Time-History Analysis. Applied Mechanics and Materials 2014; 580: 1564-1569.

[2] Möller O, Foschi RO, Quiroz LM, Rubinstein M. Structural optimization for performance-based design in earthquake engineering: Applications of neural networks. Structural Safety 2009; 31:490-99.

[3] Spacone E, Camata G, Faggella M. Nonlinear models and nonlinear procedures for seismic analysis of reinforced concrete frame structures. Computational Structural

Dynamics and Earthquake Engineering 2008: Structures and Infrastructures Book Series, 2, 323.

[4] Kalkan E, Kunnath SK. Assessment of current nonlinear static procedures for seismic evaluation of buildings. Engineering Structures 2007;29:305-16.

[5] Ghaffarzadeh H, Talebian N, Kohandel R. Seismic demand evaluation of medium ductility RC moment frames using nonlinear procedures. Earthquake Engineering and Engineering Vibration 2013;12:399-409.

[6] Domingues Costa JL, Bento R, Levtchitch V, Nielsen MP. Rigid-plastic seismic design of reinforced concrete structures. Earthquake Engineering & Structural Dynamics 2007;36:55-76.

[7] Goel SC, Liao WC, Reza Bayat M, Chao SH. Performance-based plastic design (PBPD) method for earthquake-resistant structures: an overview. The structural design of tall and special buildings 2010;19: 115-37.

[8] Liao WC, Goel SC. Performance-Based Seismic Design of RC SMF Using Target Drift and Yield Mechanism as Performance Criteria. Advances in Structural Engineering 2014;17:529-42.

[9] Amouzegar H, Riahi HT. Seismic assessment of concrete frames by endurance time method. Proceedings of the Institution of Civil Engineers-Structures and Buildings 2015;168:578-92.

[10] Celik OC, Ellingwood BR. Seismic risk assessment of gravity load designed reinforced concrete frames subjected to Mid-America ground motions. Journal of structural engineering 2009;135:414-24.

[11] Elwood KJ, Moehle JP. Dynamic collapse analysis for a reinforced concrete frame sustaining shear and axial failures. Earthquake Engineering & Structural Dynamics 2008;37:991-1012.

[12] Huang X, Kwon OS. Numerical models of RC elements and their impacts on seismic performance assessment. Earthquake Engineering & Structural Dynamics 2015;44:283-98.

[13] Zareian F, Krawinkler H. Simplified performance-based earthquake engineering. 2006. Doctoral dissertation, Stanford University.

[14] Federal Emergency Management Agency (FEMA). Seismic Performance Assessment of Buildings. Volume 1 - Methodology. FEMA P-58-1 Publication 2012:278.

[15] American Society of Civil Engineers (ASCE). Minimum design loads and associated criteria for buildings and other structures. ASCE 7 Publication 2017:889.

[16] Federal Emergency Management Agency (FEMA). NEHRP Recommended Seismic Provisions for New Buildings and Other Structures. Volume 1 - Part 1 Provisions, Part 2 Commentary. FEMA Report No. P-1050-1 2015:555.

[17] PEER. (2017). PEER Ground Motion Database [online]. Available from http://ngawest2.berkeley.edu/ [accessed 16 November 2016].

[18] Ghannoum WM, Moehle JP. Shake-table tests of a concrete frame sustaining column axial failures. ACI Structural Journal 2012;109:393-402.

[19] Guner, S., & Vecchio, F. J. Pushover analysis of shear-critical frames: formulation. ACI Structural Journal 2010;107:63-71.

[20] Vecchio FJ, Collins MP. The modified compression-field theory for reinforced concrete elements subjected to shear. ACI Journal 1986;83:219-231.

[21] Wong PS, Vecchio FJ, Trommels H. Vector2 & Formworks User's Manual. 2nd ed. 2013. http://www.vectoranalysisgroup.com/user_manuals/manual1.pdf.

[22] Guner S, Vecchio F. User's manual of VecTor5. 2008. Available from http://www.utoledo.edu/engineering/faculty/serhan-guner/Publications.html

[23] Guner S. VecTor5 [software]. 2017. Available from http://www.utoledo.edu/engineering/faculty/serhan-guner/Software.html

[24] Sadeghian V. Formworks-Plus: Improved Pre-Processor for Vector Analysis Software. 2012. Masters Thesis, Department of Civil Engineering, University of Toronto, Canada, p. 147.

[25] Blosser K, Guner S, Vecchio FJ. User's Manual of FormWorks Plus for VecTor5. 2016. Available from http://www.utoledo.edu/engineering/faculty/serhan-guner/Publications.html.

[26] Chak IN. Janus: A Post-Processor for VecTor Analysis Software. 2013. Masters Thesis, Department of Civil Engineering, University of Toronto, Canada, p. 193.

[27] Loya AS, Lourenço DDS, Guner S, Vecchio FJ. User's Manual of Janus for VecTor5. 2017. Available from http://www.utoledo.edu/engineering/faculty/serhan-guner/Publications.html.

[28] Vecchio FJ. Towards cyclic load modeling of reinforced concrete. ACI Structural Journal 1999;96:193-202.

[29] Seckin M. Hysteretic Behaviour of Cast-in-Place Exterior Beam-Column-Slab Subassemblies. 1981. Doctoral Dissertation, Department of Civil Engineering, University of Toronto, Toronto, Ontario, Canada, p. 266.

[30] LeBorgne MR, Ghannoum WM. Analytical element for simulating lateral-strength degradation in reinforced concrete columns and other frame members. Journal of Structural Engineering 2013;140:04014038.

[31] Mazzoni S, McKenna F, Scott MH, Fenves GL. OpenSees command language manual. Pacific Earthquake Engineering Research (PEER) Center 2006.

[32] American Society of Civil Engineers (ASCE). Seismic Evaluation and Retrofit of Existing Buildings. ASCE 41 Publication 2017:576. https://doi.org/10.1061/9780784414859.

[33] Filippou F. Concrete02 Material -- Linear Tension Softening. OpenSeesWiki 2010. Available from http://opensees.berkeley.edu/wiki/index.php/Concrete02_Material_--_Linear_Tension_Softening.

[34] Mander JB, Priestley MJ, Park R. Theoretical stress-strain model for confined concrete. Journal of structural engineering 1988;114:1804-26.

[35] CSI. Analysis reference manual for SAP2000, ETABS, and SAFE. Computers and Structures, Inc., 2015, California, USA.

[36] American Concrete Institute (ACI). Building code requirements for structural concrete (ACI 318-14) and commentary. American Concrete Institute 2014.

[37] Guner S, Vecchio FJ. Simplified method for nonlinear dynamic analysis of shear-critical frames. ACI Structural Journal-American Concrete Institute 2012;109:727-37.

[38] FEMA. Pre-standard and Commentary for the Seismic Rehabilitation of Buildings. FEMA-356 Publication 2000.

[39] Erberik MA. Fragility-based assessment of typical mid-rise and low-rise RC buildings in Turkey. Engineering Structures 2008;30:1360-74.

Chapter 3

[1] American Concrete Institute (ACI). Guide for the Design and Construction of Structural Concrete Reinforced with FRP Bars. ACI 440.1R-15 Publication. 2015: 88.

[2] Canadian Standards Association / National Standard of Canada (CAN/CSA). Canadian Highway Bridge Design Code. CAN/CSA S6-14 Publication 2014:894.

[3] American Concrete Institute (ACI). Building Code Requirements for Structural Concrete and Commentary. ACI 318-19 Publication 2019:624.

[4] Canadian Standards Association (CSA). Design of Concrete Structures. CSA A23.3-14 Publication 2014:290.

[5] Guner S, Vecchio FJ. Pushover Analysis of Shear-Critical Frames: Formulation. ACI Structural Journal 2010;107:63-71. http://www.utoledo.edu/engineering/faculty/serhan-guner/docs/JP1-Guner and Vecchio.pdf.

[6] Guner S, Vecchio FJ. Pushover Analysis of Shear-Critical Frames: Verification and Application. ACI Structural Journal 2010;107:72-81. http://www.utoledo.edu/engineering/faculty/serhan-guner/docs/JP2_Guner_Vecchio_2010b.pdf.

[7] Wong PS, Vecchio FJ, Trommels H. Vector2 & Formworks User's Manual. 2nd ed. 2013. http://www.vectoranalysisgroup.com/user_manuals/manual1.pdf.

[8] Vecchio FJ. Disturbed Stress Field Model for Reinforced Concrete: Formulation. Journal of Structural Engineering 2000;September:1070-7. http://www.vectoranalysisgroup.com/journal_publications/jp34.pdf.

[9] Vecchio FJ, Collins MP. The Modified Compression-Field Theory for Reinforced Concrete Elements Subjected to Shear. ACI Journal 1986;83:219-31. http://www.vectoranalysisgroup.com/journal_publications/jp2.pdf.

[10] American Association of State Highway and Transportation Officials (AASHTO). AASHTO LRFD Bridge Design Specifications. 2017:566.

[11] Hognestad E. A Study of Combined Bending and Axial Load in Reinforced Concrete Members Bulletin Series No. 399 1951: 128, https://www.ideals.illinois.edu/handle/2142/4360%0Ahttp://hdl.handle.net/2142/4360.

[12] Coulomb CA. Essai Sur Une Application des Regles de Maximis et Minimis a Quelques Problemes de Statique Relatifs a l'Architecture (Essay on Maximums and Minimums of Rules to Some Static Problems Relating to Architecture). Memoires De La Mathematique Et De Physique 1973;7:343–87.

[13] Bunni NG, Scott B, Park R, Priestley M. Stress-Strain Behavior of Concrete Confined by Overlapping Hoops at Low and High Strain Rates. ACI Journal 1982;79:496-8 pp.

[14] Vecchio FJ. Analysis of Shear-Critical Reinforced Concrete Beams. ACI Structural Journal 2000;97:102-10.

[15] Vecchio FJ. Finite Element Modeling of Concrete Expansion and Confinement. Journal of Structural Engineering 1992:118:2390-406.

[16] Bentz EC. Explaining the Riddle of Tension Stiffening Models for Shear Panel Experiments. Journal of Structural Engineering 2005;131:1422-5. http://ascelibrary.org/doi/10.1061/%28ASCE%290733-9445%282005%29131%3A9%281422%29.

[17] Walraven JC, Reinhardt HW. Theory and Experiments on the Mechanical Behaviour of Cracks in Plain and Reinforced Concrete Subjected to Shear Loading. Heron 1981;26:227-252. https://repository.tudelft.nl/islandora/object/uuid:3d68bd1a-465d-4590-b33c-7ede99bbc251/datastream/OBJ/download.

[18] Seckin M. Hysteretic Behavior of Cast-In-Place Exterior Beam-Column-Slab Assemblies. Doctoral Dissertation, University of Toronto, Toronto, Canada, 1982.

[19] Kupfer H, Hilsdorf H, Behavior of Concrete Under Biaxial Stresses. ACI Journal 1969;66:656-66. http://www.academia.edu/download/33736623/kupfer.pdf.

[20] Richart F, Brandtzaeg A, Brown RL. A Study of the Failure of Concrete under Combined Compressive Stresses. University of Illinois Bulletin 1928;26:104. http://www.academia.edu/download/33736623/kupfer.pdf.

[21] He XG, Kwan AKH. Modeling Dowel Action of Reinforcement Bars for Finite Element Analysis of Concrete Structures. Computers and Structures 2001;79:595-604.

[22] Dhakal RP, Maekawa K. Modeling for Postyield Buckling of Reinforcement. Journal of Structural Engineering 2002;128:1139-47. http://ascelibrary.org/doi/10.1061/%28ASCE%290733-9445%282002%29128%3A9%281139%29.

[23] Dhakal RP, Maekawa K. Reinforcement Stability and Fracture of Cover Concrete in Reinforced Concrete Members. Journal of Structural Engineering 2002; 128:1253-62.

[24] Grelle SV, Sneed LH. Review of Anchorage Systems for Externally Bonded FRP Laminates. International Journal of Concrete Structures and Materials 2013;7:17-33.

[25] Sato Y, Vecchio FJ. Tension Stiffening and Crack Formation in Reinforced Concrete Members with Fiber-Reinforced Polymer Sheets. Journal of Structural Engineering 2003;129:717-24.

[26] Wong RS, Vecchio FJ. Towards Modeling of Reinforced Concrete Members with Externally Bonded Fiber-Reinforced Polymer Composites. ACI Structural Journal 2003;100:47-55. http://www.vectoranalysisgroup.com/journal_publications/jp45.pdf.

[27] Ceroni F, Pecce M, Matthys S, Taerwe L. Debonding Strength and Anchorage Devices for Reinforced Concrete Elements Strengthened with FRP Sheets.

Composites Part B: Engineering 2008;39:429-41. doi:10.1016/j.compositesb.2007.05.002

[28] Cervenka V. Global Safety Format for Nonlinear Calculation of Reinforced Concrete. Beton- und Stahlbetonbau 2008;103:37-42. http://doi.wiley.com/10.1002/best.200810117.

[29] Sangiorno F. Safety Format for Non-linear Analysis of RC Structures Subjected to Multiple Failure Modes. 2015. Doctoral Dissertation, KTH Royal Institute of Technology, Stockholm, Sweden. p. 45.

[30] European Committee for Standardization (CEN). Eurocode 2 - Design of Concrete Structures - Concrete Bridges - Design and Detailing Rules. EN 1992-2:2005 Publication 2005:95.

[31] Khalifa A, Nanni A. Rehabilitation of Rectangular Supported RC Beams with Deficiencies Using CFRP Composites. Construction and Building Materials 2002;16:135-46.

[32] Al-Tamimi AK, Hawileh R, Abdalla J, Rasheed HA. Effects of Ratio of CFRP Plate Length to Shear Span and End Anchorage on Flexural Behavior of SCC RC Beams. Journal of Composites for Construction 2011;15:908-19.

Chapter 4

[1] United States Geological Survey (USGS). Why Are We Having so Many Earthquakes? Web Page 2016. https://www.usgs.gov/faqs/why-are-we-having-so-many-earthquakes-has-naturally-occurring-earthquake-activity-been.

[2] Toscano P. The Most Costly Earthquakes of All Time. Web Page 2011. https://www.cnbc.com/2011/03/15/The-Most-Costly-Earthquakes-of-All-Time.html.

[3] Popovski M, Gavric I. Performance of a 2-Story CLT House Subjected to Lateral Loads. Journal of Structural Engineering 2016;142:E4015006. https://doi.org/10.1061/(ASCE)ST.1943-541X.0001315.

[4] Izzi M, Casagrande D, Bezzi S, Pasca D, Follesa M, Tomasi R. Seismic behaviour of Cross-Laminated Timber structures: A state-of-the-art review. Engineering Structures 2018;170:42–52. https://doi.org/10.1016/j.engstruct.2018.05.060.

[5] van de Lindt JW, Furley J, Amini MO, Pei S, Tamagnone G, Barbosa AR, et al. Experimental seismic behavior of a two-story CLT platform building. Engineering Structures 2019;183:408–22. https://doi.org/10.1016/j.engstruct.2018.12.079.

[6] Ceccotti A, Sandhaas C, Okabe M, Yasumura M, Minowa C, Kawai N. SOFIE project - 3D shaking table test on a seven-storey full-scale cross-laminated timber building. Earthquake Engineering & Structural Dynamics 2013;42:2003–21. https://doi.org/10.1002/eqe.2309.

[7] Pei S, Popovski M, Van De Lindt JW. Seismic Design of a Multi-Story Cross Laminated Timber Building Based on Component Level Testing. World Conference on Timber Engineering (WCTE) 2012, Auckland, New Zealand: 2012, p. 244–52.

[8] Popovski M, Schneider J, Schweinsteiger M. Lateral Load Resistance of Cross-Laminated Wood Panels. World Conference on Timber Engineering (WCTE) 2010, Trento, Italy: 2010, p. 10.

[9] Reynolds T, Foster R, Bregulla J, Chang W-S, Harris R, Ramage M. Lateral-Load Resistance of Cross-Laminated Timber Shear Walls. Journal of Structural Engineering 2017;143:06017006. https://doi.org/10.1061/(ASCE)ST.1943-541X.0001912.

[10] Pei S, van de Lindt JW, Popovski M, Berman JW, Dolan JD, Ricles J, et al. Cross-Laminated Timber for Seismic Regions: Progress and Challenges for Research and Implementation. Journal of Structural Engineering 2016;142:E2514001. https://doi.org/10.1061/(ASCE)ST.1943-541X.0001192.

[11] Follesa M, Christovasilis IP, Vassallo D, Fragiacomo M, Ceccotti A. Seismic Design of Multi-Storey Cross Laminated Timber Buildings According to Eurocode 8. Ingegneria Sismica International Journal of Earthquake Engineering 2013;30:27–53.

[12] Hashemi A, Valadbeigi A, Masoudnia R, P.Quenneville. Seismic Resistant Cross Laminated Timber Structures Using an Innovative Resilient Friction Damping System. Proceedings of the 2016 New Zealand Society of Earthquake Engingeering Conference (NZSEE), Christchurch, New Zealand: 2016, p. 8.

[13] Joyce T, Ballerini M, Smith I. Mechanical behaviour of in-plane shear connections between CLT wall panels. Proceedings of the CIB Working Commission W18–Timber Structures. 44th meeting, Alghero, Italy: 2011, p. 3.

[14] Izzi M, Polastri A, Fragiacomo M. Investigating the Hysteretic Behavior of Cross-Laminated Timber Wall Systems due to Connections. Journal of Structural Engineering 2018;144:04018035. https://doi.org/10.1061/(ASCE)ST.1943-541X.0002022.

[15] Service NW. Pacific Tsunami Warning Center - Frequent Asked Questions. Web Page 2019. https://ptwc.weather.gov/ptwc/faq.php.

[16] Mimura N, Yasuhara K, Kawagoe S, Yokoki H, Kazama S. Damage from the Great East Japan Earthquake and Tsunami - A quick report. Mitigation and Adaptation Strategies for Global Change 2011;16:803–18. https://doi.org/10.1007/s11027-011-9297-7.

[17] Kajitani Y, Chang SE, Tatano H. Economic Impacts of the 2011 Tohoku-Oki Earthquake and Tsunami. Earthquake Spectra 2013;29:S457–78. https://doi.org/10.1193/1.4000108.

[18] Goda K, Petrone C, De Risi R, Rossetto T. Stochastic coupled simulation of strong motion and tsunami for the 2011 Tohoku, Japan earthquake. Stochastic Environmental Research and Risk Assessment 2017;31:2337–55. https://doi.org/10.1007/s00477-016-1352-1.

[19] American Society of Civil Engineers (ASCE). Minimum design loads and associated criteria for buildings and other structures. ASCE 7 Publication 2017:889.

[20] Federal Emergency Management Agency (FEMA). Guidelines for Design of Structures for Vertical Evacuation from Tsunamis. Second Edition. FEMA P-646 Publication 2012:202. https://doi.org/10.1061/40978(313)7.

[21] Yeh H, Barbosa AR, Ko H, Cawley J. Tsunami Loadings on Structures. Coastal Engineering 2014:1–13. https://doi.org/http://dx.doi.org/10.9753/icce.v34.currents.4.

[22] Poulin M, Viau C, Lacroix DN, Doudak G. Experimental and Analytical Investigation of Cross-Laminated Timber Panels Subjected to Out-of-Plane Blast

Loads. Journal of Structural Engineering 2018;144:04017197. https://doi.org/10.1061/(ASCE)ST.1943-541X.0001915.

[23] Mahdavifar V, Barbosa AR, Sinha A. Nonlinear Layered Modelling Approach for Cross Laminated Timber Panels Subjected to Out-Of-Plane Loading. 41st IAHS World Congress, Algarve, Portugal: 2016, p. 9.

[24] Fragiacomo M, Menis A, Clemente I, Bochicchio G, Ceccotti A. Fire Resistance of Cross-Laminated Timber Panels Loaded Out of Plane. Journal of Structural Engineering 2013;139:04013018. https://doi.org/10.1061/(ASCE)ST.1943-541X.0000787.

[25] Chen Y, Lam F. Bending Performance of Box-Based Cross-Laminated Timber Systems. Journal of Structural Engineering 2013;139:1–12. https://doi.org/10.1061/(ASCE)ST.1943-541X.0000786.

[26] Hristovski V, Dujic B, Stojmanovska M, Mircevska V. Full-Scale Shaking-Table Tests of XLam Panel Systems and Numerical Verification: Specimen 1. Journal of Structural Engineering 2013;139:2010–8. https://doi.org/10.1061/(ASCE)ST.1943-541X.0000754.

[27] Fragiacomo M, Dujic B, Sustersic I. Elastic and Ductile Design of Multi-Storey Crosslam Massive Wooden Buildings Under Seismic Actions. Engineering Structures 2011;33:3043–53. https://doi.org/10.1016/j.engstruct.2011.05.020.

[28] Izzi M, Flatscher G, Fragiacomo M, Schickhofer G. Experimental Investigations and Design Provisions of Steel-to-Timber Joints with Annular-Ringed Shank Nails for Cross-Laminated Timber Structures. Construction and Building Materials 2016;122:446–57. https://doi.org/10.1016/j.conbuildmat.2016.06.072.

[29] Rinaldin G, Amadio C, Fragiacomo M. A component approach for the hysteretic behaviour of connections in cross-laminated wooden structures. Earthquake Engineering & Structural Dynamics 2013;42:2023–42. https://doi.org/10.1002/eqe.2310.

[30] Ceccotti A, Sandhaas C, Yasamura M. Seismic Behaviour of Cross-Laminated Timber Buildings. Proceedings of the International Convention of Society of Wood Science and Technology and United Nations Economic Commission for Europe – Timber Committee, Geneva, Switzerland: 2010, p. 14.

[31] Gavric I, Fragiacomo M, Popovski M, Ceccotti A. Behaviour of Cross-Laminated Timber Panels under Cyclic Loads. In: Aicher S, Reinhardt H, Garrecht H, editors. Materials and Joints in Timber Structures, Dordrecht: RILEM Bookseries, vol 9. Springer; 2014, p. 689–702. https://doi.org/10.1007/978-94-007-7811-5_62.

[32] Huber JAJ, Ekevad M, Girhammar UA, Berg S. Finite element analysis of alternative load paths in a platform-framed CLT building. Proceedings of the Institution of Civil Engineers - Structures and Buildings 2020;173:379–90. https://doi.org/10.1680/jstbu.19.00136.

[33] Bedon C, Rinaldin G, Fragiacomo M, Noé S. q-factor estimation for 3D log-house timber buildings via Finite Element analyses. Soil Dynamics and Earthquake Engineering 2019;116:215–29. https://doi.org/10.1016/j.soildyn.2018.09.040.

[34] Rinaldin G, Fragiacomo M. Non-Linear Simulation of Shaking-Table Tests on 3- and 7-Storey X-Lam Timber Buildings. Engineering Structures 2016;113:133–48. https://doi.org/10.1016/j.engstruct.2016.01.055.

[35] Li M, Lam F. Lateral Behaviour of Cross Laminated Timber Shear Walls under Reversed Cyclic Loads. Proceedings of the Tenth Pacific Conference on Earthquake Engineering, 2015, p. 1–8.

[36] Pozza L, Saetta A, Savoia M, Talledo D. Angle Bracket Connections for CLT Structures: Experimental Characterization and Numerical Modelling. Construction and Building Materials 2018;191:95–113. https://doi.org/10.1016/j.conbuildmat.2018.09.112.

[37] Pozza L, Saetta A, Savoia M, Talledo D. Coupled Axial-Shear Numerical Model for CLT Connections. Construction and Building Materials 2017;150:568–82. https://doi.org/10.1016/j.conbuildmat.2017.05.141.

[38] Schneider J, Karacabeyli E, Popovski M, Stiemer SF, Tesfamariam S. Damage Assessment of Connections Used in Cross-Laminated Timber Subject to Cyclic Loads. Journal of Performance of Constructed Facilities 2014;28:371–6. https://doi.org/10.1061/(ASCE)CF.1943-5509.0000528.

[39] Mahdavifar V, Sinha A, Barbosa AR, Muszynski L, Gupta R. Lateral and Withdrawal Capacity of Fasteners on Hybrid Cross-Laminated Timber Panels. Journal of Materials in Civil Engineering 2018;30:04018226. https://doi.org/10.1061/(ASCE)MT.1943-5533.0002432.

[40] Danielsson H, Jelec M, Serrano E. Strength and Stiffness of Cross Laminated Timber at In-Plane Beam Loading. Lund, Sweden: 2017.

[41] Gavric I, Fragiacomo M, Ceccotti A. Cyclic behaviour of typical metal connectors for cross-laminated (CLT) structures. Materials and Structures 2015;48:1841–57. https://doi.org/10.1617/s11527-014-0278-7.

[42] Mahdavifar V, Barbosa AR, Sinha A, Muszynski L, Gupta R, Pryor SE. Hysteretic Response of Metal Connections on Hybrid Cross-Laminated Timber Panels. Journal of Structural Engineering 2019;145:04018237. https://doi.org/10.1061/(ASCE)ST.1943-541X.0002222.

[43] Weinfurt KP. Multivariate Analysis of Variance. Reading and Understanding Multivariate Statistics, American Psychological Association; 1995, p. 245–276.

[44] Simulia Corp. ABAQUS User's Manual, 2019 Edition. Providence, RI: Dassault Systèmes; 2019.

[45] Izzi M, Polastri A, Fragiacomo M. Modelling the Mechanical Behaviour of Typical Wall-to-Floor Connection Systems for Cross-Laminated Timber Structures. Engineering Structures 2018;162:270–82. https://doi.org/10.1016/j.engstruct.2018.02.045.

[46] Hong J, Barrett D. Three-Dimensional Finite-Element Modeling of Nailed Connections in Wood. Journal of Structural Engineering 2010;136:715–22. https://doi.org/10.1061/(ASCE)ST.1943-541X.0000160.

[47] Hassanieh A, Valipour HR, Bradford MA, Sandhaas C. Modelling of Steel-Timber Composite Connections: Validation of Finite Element Model and Parametric Study. Engineering Structures 2017;138:35–49. https://doi.org/10.1016/j.engstruct.2017.02.016.

[48] Johansen KW. Theory of Timber Connections. International Association for Bridge and Structural Engineering 1949;9:249–62. https://doi.org/10.5169/seals-9703.

[49] European Committee for Standardization (CEN). Eurocode 5: Design of timber structures: Part 1-1, General–Common rules and rules for buildings. EN 1995-1-1:2004+A1:2008 Publication 2008:121.

[50] American Wood Council (AWC). National Design Specification® for Wood Construction, 2018 Edition. NDS 2018 Publication 2017:193.

[51] Uibel T, Blaß H. Edge Joints With Dowel Type Fasteners in Cross Laminated Timber. Proceedings of the CIB-W18 Meeting 2007, Bled, Slovenia: 2007, p. 11.

[52] Brandner R, Flatscher G, Ringhofer A, Schickhofer G, Thiel A. Cross laminated timber (CLT): Overview and Development. European Journal of Wood and Wood Products 2016;74:331–51. https://doi.org/10.1007/s00107-015-0999-5.

[53] Montgomery DC. Design and Analysis of Experiments. 10th ed. Hoboken, NJ: John Wiley & Sons, Inc.; 2019.

Chapter 5

[1] Federal Emergency Management Agency (FEMA). FEMA 547: Techniques for the seismic rehabilitation of existing buildings. Washington, DC: 2006. https://doi.org/10.1061/9780784408841.

[2] Lopez RG, Pilakoutas K, Guadagnini M, Jemaa Y, Helal Y, Hajirasouliha I, et al. Seismic strengthening of deficient RC buildings using post-tensioned metal straps: An experimental investigation. Proceedings of the 15th World Conference on Earthquake Engineering (15 WCEE), 2012, p. 10.

[3] Bai J-W, Center M-AE, Hueste MB. Seismic retrofit for reinforced concrete building structures. Mid-America Earthquake Center CM-4: Structure Retrofit Strategies, College Station, TX: 2003, p. 27.

[4] Federal Emergency Management Agency (FEMA). FEMA 356: Prestandard and commentary for the seismic rehabilitation of buildings. Washington, DC: 2000.

[5] Khasreen M, Banfill PFG, Menzies G. Life-Cycle Assessment and the Environmental Impact of Buildings: A Review. Sustainability 2009;1:674–701. https://doi.org/10.3390/su1030674.

[6] Zabalza Bribián I, Valero Capilla A, Aranda Usón A. Life cycle assessment of building materials: Comparative analysis of energy and environmental impacts and evaluation of the eco-efficiency improvement potential. Building and Environment 2011;46:1133–40. https://doi.org/10.1016/j.buildenv.2010.12.002.

[7] Menna C, Asprone D, Jalayer F, Prota A, Manfredi G. Assessment of ecological sustainability of a building subjected to potential seismic events during its lifetime. The International Journal of Life Cycle Assessment 2013;18:504–15. https://doi.org/10.1007/s11367-012-0477-9.

[8] Peyroteo A, Silva M, Jalali S. Life cycle assessment of steel and reinforced concrete structures: A new analysis tool. Portugal SB07. Sustainable Construction, Materials and Practices, 2007, p. 397–402.

[9] Zhang X, Su X, Huang Z. Comparison of LCA on steel- and concrete-construction office buildings: A case study. Sixth International Conference on Indoor Air Quality, Ventilation and Energy Conservation in Buildings: Sustainable Built Environment, 2006, p. 9. https://doi.org/10.1.1.496.3903.

[10] Jönsson Å, Björklund T, Tillman AM. LCA of concrete and steel building frames. International Journal of Life Cycle Assessment 1998;3:216–24. https://doi.org/10.1007/BF02977572.

[11] Lemay L. Life cycle assessment of concrete buildings. National Ready Mixed Concrete Association (NRMCA) 2011:1–12.

[12] Peñaloza D, Norén J, Eriksson P. Life cycle assessment of different building systems: The wälludden case study. Borås, Sweden: 2013.

[13] Robertson AB, Lam FCF, Cole RJ. A Comparative Cradle-to-Gate Life Cycle Assessment of Mid-Rise Office Building Construction Alternatives: Laminated Timber or Reinforced Concrete. Buildings 2012;2:245–70. https://doi.org/10.3390/buildings2030245.

[14] Peng W, Sui Pheng L. Managing the embodied carbon of precast concrete columns. Journal of Materials in Civil Engineering 2011;23:1192–9. https://doi.org/10.1061/(ASCE)MT.1943-5533.0000287.

[15] Saiz S, Kennedy C, Bass B, Pressnail K. Comparative life cycle assessment of standard and green roofs. Environmental Science & Technology 2006;40:4312–6. https://doi.org/10.1021/es0517522.

[16] Castleton HF, Stovin V, Beck SBM, Davison JB. Green roofs: Building energy savings and the potential for retrofit. Energy and Buildings 2010;42:1582–91. https://doi.org/10.1016/j.enbuild.2010.05.004.

[17] Stephan A, Crawford RH, de Myttenaere K. A comprehensive assessment of the life cycle energy demand of passive houses. Applied Energy 2013;112:23–34. https://doi.org/10.1016/j.apenergy.2013.05.076.

[18] Dong B, Kennedy C, Pressnail K. Comparing life cycle implications of building retrofit and replacement options. Canadian Journal of Civil Engineering 2005;32:1051–63. https://doi.org/10.1139/l05-061.

[19] Chiu C, Noguchi T, Kanematsu M. Effects of maintenance strategies on the life-cycle performance and cost of a deteriorating RC building with high-seismic hazard. Journal of Advanced Concrete Technology 2010;8:157–70.

[20] Padgett JE, Dennemann K, Ghosh J. Risk-based seismic Life-Cycle Cost – Benefit (LCC-B) analysis for bridge retrofit assessment. Structural Safety 2010;32:165–73. https://doi.org/10.1016/j.strusafe.2009.10.003.

[21] Taflanidis AA, Beck JL. Life-cycle cost optimal design of passive dissipative devices. Structural Safety 2009;31:508–22. https://doi.org/10.1016/j.strusafe.2009.06.010.

[22] Gidaris I, Taflanidis AA. Performance assessment and optimization of fluid viscous dampers through life-cycle cost criteria and comparison to alternative design approaches. Bulletin of Earthquake Engineering 2015;13:1003–28. https://doi.org/10.1007/s10518-014-9646-5.

[23] Dattilo CA, Negro P, Landolfo R. An Integrated Approach for Sustainability (IAS): Life Cycle Assessment (LCA) as a supporting tool for Life Cycle Costing (LCC) and social issues. International Conference on Sustainable Building and Affordable To All, Vilamoura, Algarve, Portugal, 2010, p. 721–8.

[24] Zerbin M, Aprile A. Sustainable retrofit design of RC frames evaluated for different seismic demand. Earthquake and Structures 2015;9:1337–53. https://doi.org/10.12989/eas.2015.9.6.1337.

[25] Vitiello U, Asprone D, Di Ludovico M, Prota A. Life-cycle cost optimization of the seismic retrofit of existing RC structures. Bulletin of Earthquake Engineering 2017;15:2245–71. https://doi.org/10.1007/s10518-016-0046-x.

[26] Sibanda KL, Kaewunruen S. Life cycle assessment of retrofit strategies applied to concrete infrastructure at railway stations exposed to future extreme events. In: Ivankovi A, Mari M, Strauss A, Kišiek T, editors. International Conference on Sustainable Materials, Systems and Structures (SMSS 2019): Challenges in Design and Management of Structures, Vol 4, Rovinj, Croatia: RILEM Publications S.A.R.L.; 2019, p. 168–75.

[27] Napolano L, Menna C, Asprone D, Prota A, Manfredi G. LCA-based study on structural retrofit options for masonry buildings. International Journal of Life Cycle Assessment 2015;20:23–35. https://doi.org/10.1007/s11367-014-0807-1.

[28] Vitiello U, Salzano A, Asprone D, Di Ludovico M, Prota A. Life-cycle assessment of seismic retrofit strategies applied to existing building structures. Sustainability 2016;8:1275. https://doi.org/10.3390/su8121275.

[29] US-EPA. Construction and demolition debris generation in the united states, 2014. Washington, DC: 2014.

[30] Osmani M. Construction waste. In: Letcher T, Vallero D, editors. Waste - A Handbook for Management. 2nd ed., Academic Press; 2011, p. 207–18. https://doi.org/10.1016/B978-0-12-381475-3.10015-4.

[31] Thompson J, Watson R. Time is running out: The U.S. Landfill capacity crisis. Solid Waste Environmental Excellence Protocol (SWEEP) 2018.

https://nrra.net/sweep/time-is-running-out-the-u-s-landfill-capacity-crisis/ (accessed October 4, 2019).

[32] Shoraka MB, Elwood KJ, Yang TY, Liel AB. Collapse assessment of non-ductile, retrofitted and ductile reinforced concrete frames. ACI Special Publication 2014;297:1–20.

[33] International Standards Organization (ISO). Environmental management - Life cycle assessment - Principles and framework. ISO 14040 Publication 2006:27.

[34] International Standards Organization (ISO). Environmental management - Life cycle assessment - Requirements and guidelines. ISO 14044 Publication 2006:8.

[35] Dyngeland T. Retrofitting of bridges and building structures – A literature survey. European Laboratory for Structural Assessment, JRC-ISIS 1998;I.98.33:19.

[36] Griffith MC, Pinto A. Seismic retrofit of reinforced concrete buildings: A review and case study. 12th World Conference on Earthquake Engineering, Auckland, New Zealand, 2000, p. 1–8.

[37] Júlio ES, Branco F, Silva VD. Structural rehabilitation of columns with reinforced concrete jacketing. Progress in Structural Engineering and Materials 2003;5:29–37. https://doi.org/10.1002/pse.140.

[38] McCormick TP. Shear walls. Seismic Retrofit Training For Building Contractors & Inspectors, Timothy P. McCormick; 2005, p. 17–29.

[39] Kaplan H, Salih Y. Seismic strengthening of reinforced concrete buildings. Earthquake-Resistant Structures: Design, Assessment and Rehabilitation, InTech; 2011, p. 407–28.

[40] American Society of Civil Engineers (ASCE). Seismic evaluation and retrofit of existing buildings (ASCE 41-13). Reston, VA: 2014. https://doi.org/10.1061/9780784412855.

[41] Kaplan H, Yilmaz S, Cetinkaya N, Atimtay E. Seismic strengthening of RC structures with exterior shear walls. Sadhana 2011;36:17–34. https://doi.org/10.1007/s12046-011-0002-z.

[42] Kam WY, Pampanin S, Elwood K. Seismic performance of reinforced concrete buildings in the 22 February Christchurch (Lyttelton) earthquake. Bulletin of the New Zealand Society for Earthquake Engineering 2011;44:239–78.

[43] Bradley DS, Brooke NJ, Stuart TJ, Davidson BJ. Development of a beam-column joint model for use in the CTV Building earthquake response analysis. 2016 New Zealand Society for Earthquake Engineering (NZSEE) Annual Technical Conference, Christchurch, New Zealand: 2016, p. 12.

[44] thinkstep. GaBi ts 2017.

[45] Bare J. TRACI 2.0: the tool for the reduction and assessment of chemical and other environmental impacts 2.0. Clean Technologies and Environmental Policy 2011;13:687–96. https://doi.org/10.1007/s10098-010-0338-9.

[46] Ding T, Xiao J, Tam VWY. A closed-loop life cycle assessment of recycled aggregate concrete utilization in China. Waste Management 2016;56:367–75. https://doi.org/10.1016/j.wasman.2016.05.031.

[47] Rosado LP, Vitale P, Penteado CSG, Arena U. Life cycle assessment of natural and mixed recycled aggregate production in Brazil. Journal of Cleaner Production 2017;151:634–42. https://doi.org/10.1016/j.jclepro.2017.03.068.

[48] Korre A, Durucan S. Life cycle assessment of aggregates, EVA025–final report: Aggregates industry life cycle assessment model: Modelling tools and case studies. Banbury: 2009.

[49] Marinković S, Radonjanin V, Malešev M, Ignjatović I. Comparative environmental assessment of natural and recycled aggregate concrete. Waste Management 2010;30:2255–64. https://doi.org/10.1016/j.wasman.2010.04.012.

[50] Blengini GA. Life cycle of buildings, demolition and recycling potential: A case study in Turin, Italy. Building and Environment 2009;44:319–30. https://doi.org/10.1016/j.buildenv.2008.03.007.

Chapter 6

[1] Khasreen M, Banfill PFG, Menzies G. Life-Cycle Assessment and the Environmental Impact of Buildings: A Review. Sustainability 2009;1:674–701. https://doi.org/10.3390/su1030674.

[2] Zabalza Bribián I, Valero Capilla A, Aranda Usón A. Life cycle assessment of building materials: Comparative analysis of energy and environmental impacts and evaluation of the eco-efficiency improvement potential. Building and Environment 2011;46:1133–40. https://doi.org/10.1016/j.buildenv.2010.12.002.

[3] Menna C, Asprone D, Jalayer F, Prota A, Manfredi G. Assessment of ecological sustainability of a building subjected to potential seismic events during its lifetime. The International Journal of Life Cycle Assessment 2013;18:504–15. https://doi.org/10.1007/s11367-012-0477-9.

[4] Federal Emergency Management Agency (FEMA). Seismic Performance Assessment of Buildings. Volume 1 - Methodology. FEMA P-58-1 Publication 2012:278.

[5] Federal Emergency Management Agency (FEMA). NEHRP Commentary on the Guidelines for the Seismic Rehabilitation of Buildings. FEMA 274 Publication 1997:488.

[6] International Standards Organization (ISO). Environmental management - Life cycle assessment - Principles and framework. ISO 14040 Publication 2006:27.

[7] International Standards Organization (ISO). Environmental management - Life cycle assessment - Requirements and guidelines. ISO 14044 Publication 2006:8.

[8] Applied Technology Council. Guidelines for nonlinear structural analysis and design of buildings. Part I - general. NIST GCR 17-917-46v1 Publication 2017:137. https://doi.org/10.6028/NIST.GCR.17-917-46v1.

[9] Federal Emergency Management Agency (FEMA). Seismic Performance Assessment of Buildings. Volume 4 - Methodology for Assessing Environmental Impacts. FEMA P-58-4 Publication 2018:122.

[10] American Society of Civil Engineers (ASCE). Seismic Evaluation and Retrofit of Existing Buildings. ASCE 41 Publication 2017:576. https://doi.org/10.1061/9780784414859.

[11] John S, Nebel B, Perez N, Buchanan A. Environmental Impacts of Multi-Storey Buildings Using Different Construction Materials. Christchurch, New Zealand: 2009.

[12] Chen YJ. Comparison of Environmental Performance of a Five-Storey Building Built with Cross-Laminated Timber and Concrete. University of British Columbia, 2012.

[13] Robertson AB, Lam FCF, Cole RJ. A Comparative Cradle-to-Gate Life Cycle Assessment of Mid-Rise Office Building Construction Alternatives: Laminated Timber or Reinforced Concrete. Buildings 2012;2:245–70. https://doi.org/10.3390/buildings2030245.

[14] Durlinger B, Crossin E, Wong J. Life cycle assessment of a cross laminated timber building. vol. 61. Melbourne, Australia: Forest and Wood Products; 2013.

[15] Popovski M, Gavric I. Performance of a 2-Story CLT House Subjected to Lateral Loads. Journal of Structural Engineering 2016;142:E4015006. https://doi.org/10.1061/(ASCE)ST.1943-541X.0001315.

[16] Izzi M, Casagrande D, Bezzi S, Pasca D, Follesa M, Tomasi R. Seismic behaviour of Cross-Laminated Timber structures: A state-of-the-art review. Engineering Structures 2018;170:42–52. https://doi.org/10.1016/j.engstruct.2018.05.060.

[17] Pei S, Popovski M, Van De Lindt JW. Seismic Design of a Multi-Story Cross Laminated Timber Building Based on Component Level Testing. World Conference on Timber Engineering (WCTE) 2012, Auckland, New Zealand: 2012, p. 244–52.

[18] Popovski M, Schneider J, Schweinsteiger M. Lateral Load Resistance of Cross-Laminated Wood Panels. World Conference on Timber Engineering (WCTE) 2010, Trento, Italy: 2010, p. 10.

[19] Reynolds T, Foster R, Bregulla J, Chang W-S, Harris R, Ramage M. Lateral-Load Resistance of Cross-Laminated Timber Shear Walls. Journal of Structural Engineering 2017;143:06017006. https://doi.org/10.1061/(ASCE)ST.1943-541X.0001912.

[20] Pei S, van de Lindt JW, Popovski M, Berman JW, Dolan JD, Ricles J, Sause R, Blomgren H, Rammer DR. Cross-Laminated Timber for Seismic Regions: Progress and Challenges for Research and Implementation. Journal of Structural Engineering 2016;142:E2514001. https://doi.org/10.1061/(ASCE)ST.1943-541X.0001192.

[21] Follesa M, Christovasilis IP, Vassallo D, Fragiacomo M, Ceccotti A. Seismic Design of Multi-Storey Cross Laminated Timber Buildings According to Eurocode 8. Ingegneria Sismica International Journal of Earthquake Engineering 2013;30:27–53.

[22] Hashemi A, Valadbeigi A, Masoudnia R, Quenneville P. Seismic Resistant Cross Laminated Timber Structures Using an Innovative Resilient Friction Damping System. Proceedings of the 2016 New Zealand Society of Earthquake Engingeering Conference (NZSEE), Christchurch, New Zealand: 2016, p. 8.

[23] Joyce T, Ballerini M, Smith I. Mechanical behaviour of in-plane shear connections between CLT wall panels. Proceedings of the CIB Working Commission W18–Timber Structures. 44th meeting, Alghero, Italy: 2011, p. 3.

[24] Izzi M, Polastri A, Fragiacomo M. Investigating the Hysteretic Behavior of Cross-Laminated Timber Wall Systems due to Connections. Journal of Structural

Engineering 2018;144:04018035. https://doi.org/10.1061/(ASCE)ST.1943-541X.0002022.

[25] Salgado RA, Guner S. Characterization of the Out-of-Plane Behavior of CLT Panel Connections for Tsunami Load Resilience. Submitted for Publication 2020.

[26] Salgado RA, Guner S. Out-of-Plane Constitutive Model to Capture the Tsunami-Load Response of Cross Laminated Timber Buildings. 17th World Conference on Earthquake Engineering, 17WCEE, 2020, p. 12.

[27] Ceccotti A, Sandhaas C, Okabe M, Yasumura M, Minowa C, Kawai N. SOFIE project - 3D shaking table test on a seven-storey full-scale cross-laminated timber building. Earthquake Engineering & Structural Dynamics 2013;42:2003–21. https://doi.org/10.1002/eqe.2309.

[28] European Committee for Standardization (CEN). Eurocode 8: Design of structures for earthquake resistance - Part 1: General rules, seismic actions and rules for buildings. EN 1998-1:2004 Publication 2004:229.

[29] American Society of Civil Engineers (ASCE). Minimum design loads and associated criteria for buildings and other structures. ASCE 7 Publication 2017:889.

[30] Simulia Corp. ABAQUS User’s Manual, 2019 Edition. Providence, RI: Dassault Systèmes; 2019.

[31] Rinaldin G, Amadio C, Fragiacomo M. A component approach for the hysteretic behaviour of connections in cross-laminated wooden structures. Earthquake Engineering & Structural Dynamics 2013;42:2023–42. https://doi.org/10.1002/eqe.2310.

[32] Gavric I, Fragiacomo M, Ceccotti A. Cyclic behaviour of typical metal connectors for cross-laminated (CLT) structures. Materials and Structures 2015;48:1841–57. https://doi.org/10.1617/s11527-014-0278-7.

[33] Guner S, Vecchio FJ. Pushover Analysis of Shear-Critical Frames : Formulation. ACI Structural Journal 2010;107:63–71.

[34] Guner S, Vecchio FJ. Pushover Analysis of Shear-Critical Frames: Verification and Application. ACI Structural Journal 2010;107:72–81.

[35] Vecchio FJ, Collins MP. The Modified Compression-Field Theory for Reinforced Concrete Elements Subjected to Shear. ACI Journal 1986;83:219–31.

[36] Vecchio FJ. Disturbed Stress Field Model for Reinforced Concrete: Formulation. Journal of Structural Engineering 2000;September:1070–7.

[37] Guner S, Vecchio F. User's manual of VecTor5. 2008.

[38] Salgado RA, Guner S. A comparative study on nonlinear models for performance-based earthquake engineering. Engineering Structures 2018;172:382–91. https://doi.org/10.1016/j.engstruct.2018.06.034.

[39] Guner S, Vecchio FJ. Analysis of Shear-Critical Reinforced Concrete Plane Frame Elements under Cyclic Loading. Journal of Structural Engineering 2011;137:834–43. https://doi.org/10.1061/(ASCE)ST.1943-541X.0000346.

[40] Wong PS, Vecchio FJ, Trommels H. Vector2 & Formworks User's Manual. 2nd ed. 2013. http://www.vectoranalysisgroup.com/user_manuals/manual1.pdf.

[41] Akkaya Y, Guner S, Vecchio FJ. Constitutive Model for Inelastic Buckling Behavior of Reinforcing Bars. ACI Structural Journal 2019;116:195–204. https://doi.org/10.14359/51711143.

[42] Petrone C, Rossetto T, Goda K. Fragility assessment of a RC structure under tsunami actions via nonlinear static and dynamic analyses. Engineering Structures 2017;136:36–53. https://doi.org/10.1016/j.engstruct.2017.01.013.

[43] Qi ZX, Eames I, Johnson ER. Force acting on a square cylinder fixed in a free-surface channel flow. Journal of Fluid Mechanics 2014;756:716–27. https://doi.org/10.1017/jfm.2014.455.

[44] National Concrete Masonry Association. Design of Concrete Masonry Infill 2019. https://ncma.org/resource/design-of-concrete-masonry-infill/ (accessed July 5, 2020).

[45] Bare J. TRACI 2.0: the tool for the reduction and assessment of chemical and other environmental impacts 2.0. Clean Technologies and Environmental Policy 2011;13:687–96. https://doi.org/10.1007/s10098-010-0338-9.

[46] thinkstep, GaBi ts, (2017). http://www.gabi-software.com/america/index/.

[47] Guo H, Liu Y, Meng Y, Huang H, Sun C, Shao Y. A Comparison of the Energy Saving and Carbon Reduction Performance between Reinforced Concrete and Cross-Laminated Timber Structures in Residential Buildings in the Severe Cold Region of China. Sustainability 2017;9:1426. https://doi.org/10.3390/su9081426.

[48] Salgado RA, Apul D, Guner S. Life cycle assessment of seismic retrofit alternatives for reinforced concrete frame buildings. Journal of Building Engineering 2020;28:101064. https://doi.org/10.1016/j.jobe.2019.101064.

[49] Attary N, van de Lindt JW, Unnikrishnan VU, Barbosa AR, Cox DT. Methodology for Development of Physics-Based Tsunami Fragilities. Journal of Structural

Engineering 2016;143:12. https://doi.org/10.1061/(ASCE)ST.1943-541X.0001715.

[50] Darby HJ, Elmualim A, Kelly F. A case study to investigate the life cycle carbon emissions and carbon storage capacity of a cross laminated timber, multi-storey residential building. Proceedings of the World Sustainable Building Conference, Singapore: 2013, p. 1–8.

[51] Hafner A, Schäfer S. Comparative LCA study of different timber and mineral buildings and calculation method for substitution factors on building level. Journal of Cleaner Production 2017;167:630–42. https://doi.org/10.1016/j.jclepro.2017.08.203.

[52] Skullestad JL, Bohne RA, Lohne J. High-Rise Timber Buildings as a Climate Change Mitigation Measure – A Comparative LCA of Structural System Alternatives. Energy Procedia 2016;96:112–23. https://doi.org/10.1016/j.egypro.2016.09.112.

[53] Chen C, Pierobon F, Ganguly I. Life Cycle Assessment (LCA) of Cross-Laminated Timber (CLT) Produced in Western Washington: The Role of Logistics and Wood Species Mix. Sustainability 2019;11:1278. https://doi.org/10.3390/su11051278.

Chapter 7

[1] Lew HS, Bao Y, Pujol S, Sozen MA. Experimental study of reinforced concrete assemblies under column removal scenario. ACI Structural Journal. 2014 Jul 1;111(4):881.

[2] Yap SL, Li B. Experimental investigation of reinforced concrete exterior beam-column subassemblages for progressive collapse. ACI Structural Journal. 2011 Sep 1;108(5):542.

[3] Celik OC, Ellingwood BR. Modeling beam-column joints in fragility assessment of gravity load designed reinforced concrete frames. Journal of Earthquake Engineering. 2008 Mar 14;12(3):357-81.

[4] Jeon JS, Lowes LN, DesRoches R. Numerical Models for Beam-Column Joints in Reinforced Concrete Building Frames. Special Publication. 2014 Mar 6;297:1-26.

[5] Mitra N, Lowes LN. Evaluation, calibration, and verification of a reinforced concrete beam–column joint model. Journal of Structural Engineering. 2007 Jan;133(1):105-20.

[6] Altoontash A. Simulation and damage models for performance assessment of reinforced concrete beam-column joints (Doctoral dissertation, Stanford University).

[7] Shin M, LaFave JM. Modeling of cyclic joint shear deformation contributions in RC beam-column connections to overall frame behavior. Structural Engineering and Mechanics. 2004 Nov 1;18(5):645-70.

[8] Teraoka M, Fujii S. Seismic damage and performance evaluation of R/C beam-column joints. In The Second US-Japan Workshop on Performance-Based Engineering for Reinforced Concrete Buliding Structures 2000 (pp. 379-390).

[9] Theiss AG. Modeling the Earthquake Response of Older Reinforced Concrete Beam-Column Building Joints (Doctoral dissertation, University of Washington).

[10] Anderson M, Lehman D, Stanton J. A cyclic shear stress–strain model for joints without transverse reinforcement. Engineering Structures. 2008 Apr 30;30(4):941-54.

[11] Birely AC, Lowes LN, Lehman DE. A model for the practical nonlinear analysis of reinforced-concrete frames including joint flexibility. Engineering Structures. 2012 Jan 31;34:455-65.

[12] Kim J, LaFave JM. Joint Shear Behavior Prediction in RC Beam-Column Connections Subjected to Seismic Lateral Loading.

[13] Vecchio FJ, Collins MP. The modified compression-field theory for reinforced concrete elements subjected to shear. ACI J.. 1986 Mar 1;83(2):219-31.

[14] Lowes LN, Altoontash A, Mitra N. Closure to "Modeling Reinforced-Concrete Beam-Column Joints Subjected to Cyclic Loading" by Laura N. Lowes and Arash Altoontash. Journal of Structural Engineering. 2005 Jun;131(6):993-4.

[15] ACI A. 318-02 Building Code Requirements for Structural Concrete. American Concrete Institute, Farmington Hills, USA. 2002.

[16] McKenna F, Fenves GL, Scott MH. Open system for earthquake engineering simulation. University of California, Berkeley, CA. 2000.

[17] Mander JB, Priestley MJ, Park R. Theoretical stress-strain model for confined concrete. Journal of structural engineering. 1988 Aug;114(8):1804-26.